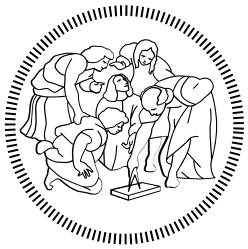

POLITECNICO
MILANO 1863

SCHOOL OF INDUSTRIAL AND
INFORMATION ENGINEERING

Multi-colour power splitters based on femtosecond-laser-written directional couplers

Master of Science Degree in
Engineering Physics - Ingegneria Fisica

Author: **Matteo Balen**

Student ID: 970729
Advisor: Prof. Roberto Osellame
Co-advisors: Dr. Francesca Bragheri
Academic Year: 2021-2022

Abstract

In recent years the field of optical microscopy has been characterised by an increasing interest in the realization of Microscopes on Chip (MOCs), compact integrated systems encompassing optical and fluidic components for the automation of the imaging process. MOCs have the goal of revolutionizing access to powerful microscopy techniques, thanks to their reduced costs, simplicity of use and measurement automation. Among the many fabrication techniques utilized for the realization of integrated optic devices, femtosecond laser micromachining (FLM) is the one exploited in the present work. The goal of this work is the realization of an FLM-written integrated circuit working as a multi-wavelength power splitter to be utilized in a MOC. In fact, in biological sample imaging, the ability to discern multiple structures in the specimen is of paramount importance. In dealing with fluorescence microscopy, the evaluation of distinct fluorescent markers is therefore imperative. The need for multiple illumination wavelengths thus stems from the excitation of distinct fluorophores, with specific absorption lines. It is demonstrated that the required power-splitting device can be realized by exploiting directional couplers and that it is possible to achieve multi-wavelength operation by tuning their parameters. Two methods are reported which allow manufacturing power splitters operating at selected wavelengths and over an extended bandwidth. Furthermore, the experimental validation of these methods is described. The present work constitutes important evidence towards the realization of MOCs with ever-increasing quality, not dissimilar to the one attainable with bulk optics solutions.

Keywords: FLM, MOC, SIM, Integrated Optics, Directional Couplers

Abstract in lingua italiana

Negli ultimi anni il campo della microscopia ottica ha mostrato un crescente interesse nello sviluppo di microscopi su chip (MOCs), ossia compatti sistemi integrati costituiti da componenti ottiche e fluidiche adatte all'automazione del processo di imaging. I MOC hanno lo scopo di rivoluzionare l'accesso a potenti tecniche di microscopia grazie ai loro costi ridotti, la semplicità di utilizzo e l'automazione della misura. Fra le molte tecniche di fabbricazione utilizzate per la realizzazione di dispositivi di ottica integrata, la microfabbricazione con laser a femtosecondi (FLM) è quella sfruttata in questo lavoro. L'obiettivo di questo progetto di tesi consiste nella realizzazione di un circuito di ottica integrata operante a multiple lunghezze d'onda, sviluppato tramite FLM, che operi come distributore di potenza da utilizzare in un MOC. Infatti, nell'imaging di campioni biologici, l'abilità di distinguere le diverse strutture presenti in un campione è di primaria importanza. Lavorando con microscopia a fluorescenza la capacità di valutare diversi marcatori fluorescenti è perciò imprescindibile. Il requisito di illuminazione a diverse lunghezze d'onda nasce dunque dalla necessità di eccitare specifici fluorofori. In questo lavoro è stata dimostrata la realizzazione di dispositivi per la distribuzione di potenza sfruttando accoppiatori direzionali e la possibilità di operazione a diverse lunghezze d'onda. Sono riportati due metodi per la fabbricazione di distributori di potenza operanti a singole lunghezze d'onda e in una banda estesa. Inoltre, è presentata la validazione sperimentale dei metodi descritti. Questo lavoro costituisce una importante evidenza della possibilità di realizzare MOC di alta qualità e non dissimile da quella ottenibile con sistemi in ottica da banco.

Parole chiave: FLM, MOC, SIM, Ottica integrata, Accoppiatori direzionali

Contents

Introduction

In the recent years, a rapid expansion in the interest in the field of optical microscopy for compact integrated systems called Microscopes On Chip (MOC) occurred. These devices aim at enabling the use of advanced microscopy techniques, integrated into a portable, low-cost and easy-to-use system tailored for many applications, ranging from point-of-care diagnostics to material sciences and biology. In fact, integrating all the components required to perform a given type of analysis in a single device, largely simplifies its usage as compared to bulk optics instrumentation, since there is no need for day-by-day alignment. Furthermore, the usage of samples and other substances is vastly reduced thanks to the small form factor of these devices. Finally, the combination of these aspects allows for a cost reduction of the imaging platform.

Depending on the material utilized, different lithographic techniques can be exploited to realize integrated optical circuits. A particularly interesting technique utilized to manufacture MOCs is Femtosecond Laser Micromachining (FLM). FLM is a versatile fabrication technique that enables the fabrication of optical and fluidic components of almost arbitrarily complex three-dimensional structures. Thanks to its versatility FLM allows the realization, on the same chip, of integrated optical components for the delivery of light — such as optical waveguides and lenses — and microfluidic channels for transporting and manipulating samples. One of the great advantages of this fabrication method is that thanks to the simultaneous fabrication of the necessary structures, fluidic and optical components alike are perfectly aligned, granting the best possible performance. Furthermore, the alignment of the components is robust, and unchanging, greatly simplifying the procedure required to perform complex imaging measurements.

A promising microscopy technique well suited for its integration on a MOC is light-sheet fluorescence microscopy (LSFM). It consists of illuminating the sample with a thin light-sheet — typically obtained with cylindrical lenses — and collecting the fluorescent signal from an entire slice of the sample at a time, thus allowing for the 3D reconstruction of the specimen. The short acquisition time and the low photo-toxicity of this technique are two advantages that make LSFM adapt to the imaging of live biological samples at high throughput. One drawback of the technique is the lateral resolution, which is limited by

diffraction and doesn't allow imaging of subcellular structures. To improve the resolution LSFM can be combined with structured illumination microscopy (SIM), which exploits a patterned illumination to obtain super-resolved imaging of a sample. Typically, the structured illumination is obtained by the interference of multiple light beams which can be easily integrated with the LSFM illumination geometry.

This thesis work is a part of a project aimed at the realization of light-sheet structured illumination microscope integrated on a glass chip. The device studied in the course of the project features a three-way illumination with light-sheets obtained with embedded cylindrical lenses. Such light-sheets, perfectly aligned with a microfluidic channel in which the specimens are flown, create an interference pattern that is employed for SIM and attain super-resolved imaging. To obtain the desired illumination pattern it is necessary to split the power of the input laser beam across the three light-sheets. Therefore a custom integrated optical circuit is realized with FLM to deliver light on the cylindrical lenses. The goal of this thesis work is the study and implementation of optical elements that are insensitive to the illumination wavelength. In fact, when dealing with fluorescence microscopy, the possibility to illuminate the sample at multiple wavelengths is of paramount importance. Exciting different fluorophores contained in the specimen allows the identification of multiple structures and thus enriching the information content obtained.

The first chapter of this work presents the theory regarding the most important integrated optical components, which constitute the main topic of this theses project. The second chapter deals instead with the fundamental principles of the fabrication technique utilized, that is FLM. Furthermore, an overview is given of the most important parameters that play a role in the irradiation of a sample and the different type of permanent modifications that can be obtained in the substrates. The third chapter concludes the theoretical discussions, presenting structured illumination microscopy, the microscopy technique that is at the centre of the project this thesis takes part in. Chapter 4 explains the methods and techniques that have been utilized in this work for the realization of the integrated circuits under study and their validation. The fifth chapter presents the results of the preliminary studies regarding the fabrication of low-loss waveguides and the characterization of the directional couplers. Finally, chapter 6 reports the work carried out for the design and the fabrication of multi-colour couplers.

1 | Integrated Optics

The term "integrated optics" refers to the concept emerged in the late 1960s of the realization of miniaturized optical integrated circuits (OICs), also known as photonic integrated circuits (PICs), to substitute conventional electrical integrated circuits to perform optical signal processing. Integrated optics entails the realization of optical circuits that perform processing operations such as power splitting, multiplexing and demultiplexing of distinct wavelength carriers, signal filtering and light modulation without the need for bulk optics or electronics and optical-electrical-optical (O-E-O) conversion. Some of the advantages of such devices are low-loss transmission, large bandwidth, circuits of small size and light weight among many other. [1] The main component of integrated optical devices are optical waveguides, which not only allow to deliver light to the various elements constituting the optical circuit, but also are the fundamental structure that enables their implementation. Some of most important optical components utilized in integrate optics, of which will be given an overview in this chapter, are: couplers, Mach-Zehnder interferometers and phase shifters.

1.1. Theory of optical waveguides

The optical waveguide is the fundamental element that interconnects the various devices of an optical integrated circuit. The simplest form of optical waveguide is the planar dielectric waveguide, also referred to as slab waveguide, that is a structure composed of three layers of material with refractive indices n_1, n_2 and n_3 stacked onto each other in one direction (x) and infinite in the other two (y and z, where the z axis is assumed to be the propagation direction), as represented on the left in figure 1.1. Clearly, this structure cannot be a practical waveguide but it helps to lay the foundations for the study of waveguides due to its relative simplicity. [1, 2]

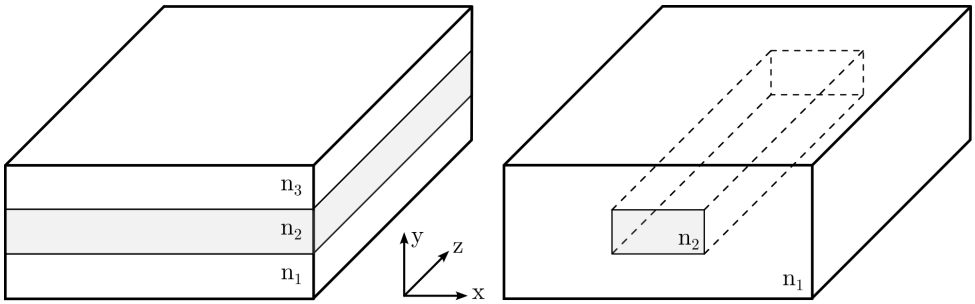

Figure 1.1: Representation of a planar waveguide (left) and a channel waveguide (right).

To describe how light propagates through a guiding structure we resort to Maxwell's equations:

$$\vec{\nabla} \times \vec{E}(\vec{r},t) = -\frac{\partial \vec{B}(\vec{r},t)}{\partial t} \qquad \vec{\nabla} \cdot \vec{D}(\vec{r},t) = \rho$$

$$\vec{\nabla} \cdot \vec{B}(\vec{r},t) = 0 \qquad \vec{\nabla} \times \vec{H}(\vec{r},t) = \vec{J} + \frac{\partial \vec{D}(\vec{r},t)}{\partial t}$$

With the constitutive equations, valid in linear isotropic and non magnetic media:

$$\vec{D}(\vec{r},t) = \epsilon_0 \epsilon_r(\vec{r}) \vec{E}(\vec{r},t) \qquad \vec{B}(\vec{r},t) = \mu_0 \mu_r(\vec{r}) \vec{H}(\vec{r},t) \simeq \mu_0 \vec{H}(\vec{r},t)$$

In the case of a medium free of charges $\rho = 0$ and without free currents $\vec{J} = 0$, under the weakly guiding approximation[1] $\epsilon_r(\vec{r}) = \epsilon_r$, Maxwell's equations can be combined and one can identify Maxwell's wave equation:

$$\nabla^2 \vec{E}(\vec{r},t) = \frac{n(\vec{r})^2}{c^2} \frac{\partial^2 \vec{E}(\vec{r},t)}{\partial t^2} \tag{1.1}$$

In fact, optical waves travel inside a waveguide in distinct and discrete optical modes,which describe a spatial distribution of optical energy that remains constant in time. An optical mode is an electromagnetic field that is a solution of equation (1.1).

Considering the case of monochromatic plane waves the solutions have the form:

$$\vec{E}(\vec{r},t) = \vec{E}(x,y) e^{i\omega t - i\beta z} \tag{1.2}$$

being β the propagation constant. Now substituting the ansatz of solution (1.2) in the

[1] Always valid in the case of small relative difference in the refractive indices of core and claddings.

wave equation (1.1) one obtains the following equation:

$$\frac{\partial^2 \vec{E}(x,y)}{\partial x^2} + \frac{\partial^2 \vec{E}(x,y)}{\partial y^2} + \left[k^2 n^2(\vec{r}) - \beta^2\right] \vec{E}(x,y) = 0 \tag{1.3}$$

where $k \triangleq \omega/c$. The solutions of such equation in the different media composing the guiding structure can either be sinusoidal functions, thus describing the propagation of the optical field, or exponentially decaying functions, depending on the sign of the quantity $k^2 n^2(\vec{r}) - \beta^2$. In fact, considering the case of the planar waveguide, when the value of $\beta < k n_i \quad \forall\ i = 1,2,3$ the solution of equation (1.3) only yields propagative solutions, meaning that the structure is not confining the light. Conversely if $n_2 > n_{1,2}$ and $k n_{1,3} < \beta < k n_2$ solutions in which the optical field is confined in the region 2 can be identified, these are guided modes. Example of such modes are represented in figure 1.2.

Formally solving equation (1.1) imposing the appropriate boundary conditions of continuity of the electric field at the interface between the different media, yields a constraint on the value of β. In fact, while for propagative modes β can take on any value, for guided modes β can take on a set of discrete values. To each β corresponds a different guided mode with a different distribution of energy in space and a different propagation constant. The set of possible values for β is discrete but infinite yet not all the modes can be supported by the guiding structure. For a given guiding structure can be written a cut-off condition which correlates the refractive index contrast of the structure with the geometrical dimensions of the structure and the wavelength of the light. Such cut-off condition describes how many modes can be supported by a given structure at a given wavelength. Typically, the smaller the ratio between the wavelength and the dimension of the core of the waveguide or the bigger the index contrast, the more modes are supported by the guiding structure.

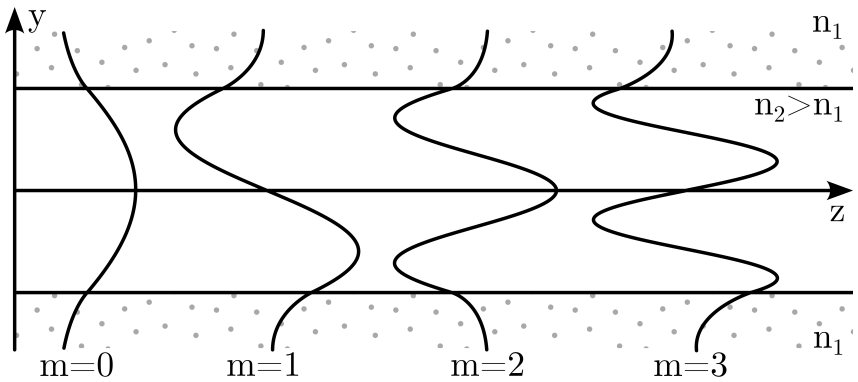

Figure 1.2: Representation of the first four modes of a planar waveguide. Each graph represents the distribution of the electric field inside the waveguide.

An important fact that is worth highlighting is that the guided modes are orthogonal with each other thus no power can be exchanged from one to the other. Shining light in a waveguide will give power to all the supported modes, depending on the overlap between them and the input light, which will travel along the waveguide without interaction.

As already anticipated the planar waveguide does not constitute a guiding structure which can actually be applied in real integrated optical circuits. The channel waveguide — represented on the right in figure 1.1 — instead consists of a guiding structure characterised by a region of refractive index n_1 surrounded by a confining medium of lesser index n_2, capable of confining light in two dimensions and allow its propagation in the third. The modes guided by this structure can be identified with the same procedure mentioned previously solving Maxwell's wave equation[2] and imposing the correct boundary conditions. This is the most fundamental structure utilized in integrated optical circuits.

Concluding this section on optical waveguides it is worth presenting the on of the most common implementation of this kind of technology, that is optical fibers. In its simplest form an optical fiber consists of two concentric cylinders, the core and the surrounding cladding, respectively of refractive indexes n_1 and $n_2 < n_1$ Two different types of optical fibers exist depending on how the transition of the refractive index occurs, in a *step-index fiber* the refractive index changes abruptly at the core-cladding interface and remains constant otherwise, in a *graded-index fiber* instead, the refractive index varies gradually inside the core. Notwithstanding this difference, the phenomena that is responsible for the guiding of light, in both types of fibers, is total internal reflection. Considerable insight in the guiding properties of optical fibers can be gained by using a ray picture based on geometrical optics.[3] [3]

As exemplified in the figure 1.3, in a step index fiber the refractive index changes abruptly at the interface of core and cladding. Given the refractive indexes of core and cladding, respectively n_1 and $n_2 < n_1$ we can define the *critical angle* φ_c such that:

$$\sin \varphi_c = n_2/n_1$$

Light rays impinging at such interface with an angle φ smaller than the critical angle φ_c experience total internal reflection and remain confined within the fiber core. On the contrary, rays impinging with an angle $\varphi < \varphi_c$ are refracted outside the core.

---

[2] Admittedly an exact solution for the wave equation for this kind of structure has not been obtained yet, but approximate solutions exist.

[3] The geometrical-optics description is valid when the core of the fiber is much larger than the wavelength of the optical carrier.

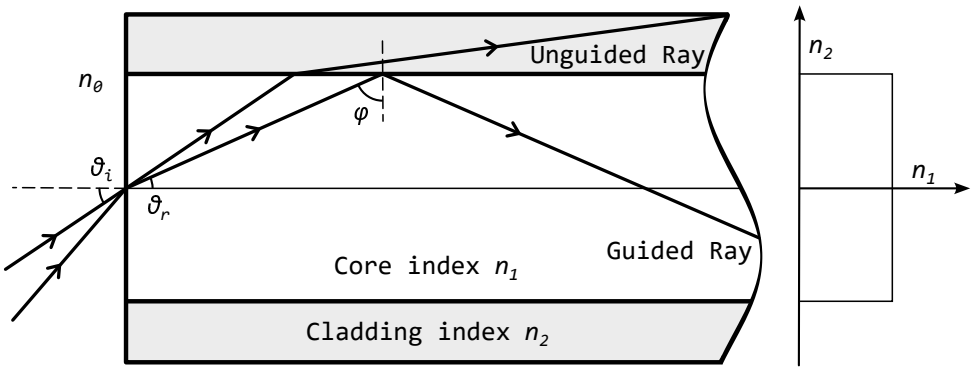

Figure 1.3: Light confinement through total internal reflection in step-index fibers. [3]

One peculiar information concerning this kind of optical waveguide is that the fundamental mode has no cutoff and is always supported by the fiber.

In a graded-index fiber the refractive index of the core is not constant and decreases from its maximum value n_1 at the core centre to its minimum value n_2 at the core-cladding interface. Figure 1.4 shows schematically paths for three different rays propagating through the fiber.

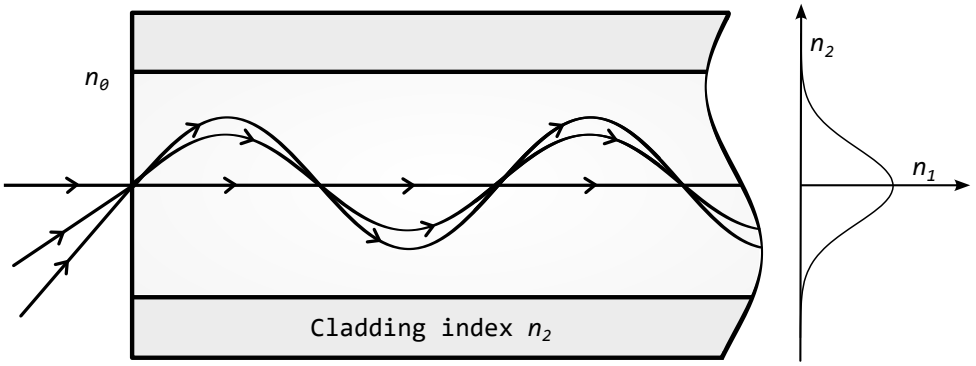

Figure 1.4: Ray trajectories in a graded-index fiber. [3]

1.2. Directional couplers

By the term Directional Coupler, we refer to a light guiding structure composed of two waveguides with two inputs and two outputs for light. In figure 1.5 it is reported the general geometry of a coupler.

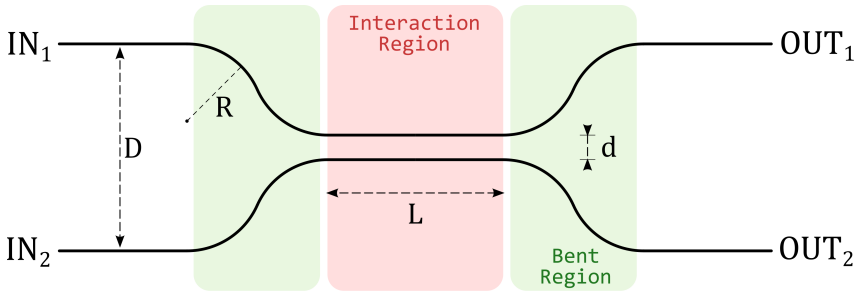

Figure 1.5: The geometry of a directional coupler. [3]

The two waveguides, initially at a distance D, are brought closer one to one another at a distance d, called *interaction distance*, for a given length L, called *interaction length*. The central region in which the waveguides are close to each other is defined *interaction region* since here the light coupled in either of the waveguides interacts and exchanges energy with the other, while maintaining phase coherence, through an evanescent coupling of their modes. In this work, we will consider that the waveguides come close together, and subsequently get further apart, following two consecutive arcs of a circle of radius R. The two sections of approach and departure of the waveguides constitute the *bent region*, which, as it will be detailed forward, partially contributes to the exchange of power between the two modes.

The underlying assumption of this geometry is that the distance d is small enough such that there is a power exchange between the waveguides while at the distance D they are far enough apart so that no coupling of the modes occurs.

1.2.1. Coupled Mode Theory

To study the behaviour of light propagating in two interacting waveguides a possible approach is to follow the laws of electromagnetism rigorously. Unfortunately, this method suffers from one main problem that is the difficulty to deal with the mathematical description of the structure of the directional coupler, being a structure that is not as simple as two nearby waveguides since it is characterized by two curved regions in which the distance of the waveguides varies along the propagation direction. [4]

The approach typically used to describe such structures is represented by the Coupled Mode Theory. In CMT the two waveguides constituting the Directional Coupler are considered as two separate structures each of them guiding a single mode indicated as ψ_j.

A general field distribution in the overall structure can be represented as a superposition of the two fundamental modes:

$$\psi = A_1(z)\psi_1(x,y)e^{-j\beta_1 z} + A_2(z)\psi_2(x,y)e^{-j\beta_2 z} \tag{1.4}$$

The two modes are not perpendicular, as they do not represent modes of the same guiding structure, therefore an exchange of power between the two is allowed because of the overlap of the exponential tails of the two modes in the region that separates the waveguides. To integrate this exchange of power the two complex coefficients A_1 and A_2 present dependence of the propagation along the direction z.

The CMT represents a good approximation of the correct results, that come from a rigorous electromagnetic description, under the assumption of weak coupling, which implies that the dielectric structure can be considered as formed by two separated and distinct waveguides.

The wave equation of the guiding structure can be, then, written as:

$$\nabla_t^2\,\psi + \frac{\partial^2\psi}{\partial z^2} + k_0^2 n^2(x,y)\psi = 0 \tag{1.5}$$

By inserting the expression of the field (1.4) in the equation (1.5) and neglecting the second order derivative in z of the coefficients A_1 and A_2, which do not vary significantly under the weak coupling condition, one obtains the following expression:

$$-2j\beta_1\dot{A}_1\psi_1 - 2j\beta_2\dot{A}_2\psi_2 e^{j\Delta\beta z} + A_1\psi_1\Delta n_1^2 k_0^2 + A_2\psi_2\Delta n_2^2 k_0^2 e^{j\Delta\beta z} = 0 \tag{1.6}$$

in which we have defined the detuning parameter $\Delta\beta = \beta_1 - \beta_2$ which is the difference in the propagation constants of the two waveguides and Δn_j such that:

$$n^2(x,y) = n_1^2(x,y) + \Delta n_1^2(x,y) = n_2^2(x,y) + \Delta n_2^2(x,y)$$

Multiplying equation (1.6) by ψ_1^* and integrating over the transverse plane we obtain:

$$\begin{aligned} &- 2j\beta_1\dot{A}_1 \iint \psi_1\psi_1^*\, dxdy - 2j\beta_2\dot{A}_2 e^{j\Delta\beta z} \iint \psi_2\psi_1^*\, dxdy + \\ &+ k_0^2 A_1 \iint \psi_1\Delta n_1^2\psi_1^*\, dxdy + k_0^2 A_2 e^{j\Delta\beta z} \iint \psi_2\Delta n_2^2\psi_1^*\, dxdy = 0. \end{aligned} \tag{1.7}$$

Now by dividing by the term

$$2\beta_1 \iint \psi_1\psi_1^*\, dxdy$$

and defining the coefficient

$$k_{il} = \frac{k_0^2}{2\beta_i} \cdot \frac{\iint \psi_l \Delta n_l^2 \psi_i^2 dxdy}{\iint \psi_i\psi_i^* dxdy} \tag{1.8}$$

we obtain the following equation:

$$-j\dot{A}_1 + k_{11}A_1 + k_{12}A_2 e^{+j\Delta\beta z} = 0 \tag{1.9}$$

where we have defined the parameter $\Delta\beta \triangleq \beta_1 - \beta_2$.

Repeating the same procedure but this time multiplying by ψ_2^*, integrating over the plane and finally dividing by

$$2\beta_2 \iint \psi_2\psi_2^*\, dxdy$$

we obtain:

$$-j\dot{A}_2 + k_{22}A_2 + k_{21}A_1 e^{-j\Delta\beta z} = 0 \tag{1.10}$$

We have thus obtained a set of two coupled equations describing the exchange of power in the two waveguides:

$$\begin{cases} \dot{A}_1 = -jk_{11}A_1 - jk_{12}A_2 e^{+j\Delta\beta z} \\ \dot{A}_2 = -jk_{22}A_2 - jk_{21}A_1 e^{-j\Delta\beta z} \end{cases} \tag{1.11}$$

Typically however the coupling coefficients k_{11} and k_{22} are negligible and the system is simplified as follows:

$$\begin{cases} \dot{A}_1 = -jk_{12}A_2 e^{+j\Delta\beta z} \\ \dot{A}_2 = -jk_{21}A_1 e^{-j\Delta\beta z} \end{cases} \tag{1.12}$$

CMT applied to directional couplers

Now we will apply the results obtained with coupled mode theory to the case of a directional coupler. This means that we will consider the two waveguides to be coupled only in the interaction region, where the distance, and the coupling coefficients are constant with z, while we will neglect for the time being the bent region. Defining the following quantities:

$$\begin{cases} R(z) \triangleq A_1(z)e^{-j\delta z} \\ S(z) \triangleq A_2(z)e^{+j\delta z} \end{cases}, \quad \delta = \frac{\Delta\beta}{2}$$

and substituting them in the system of equations (1.12) the exponential dependencies cancel out and we obtain the following system:

$$\begin{cases} \dot{R} = -j\delta R - jk_{12}S \\ \dot{S} = j\delta S - jk_{21}R \end{cases} \tag{1.13}$$

This is a linear system of coupled differential equations and, to solve it, we can differentiate again both sides of both equations with respect to the z coordinate:

$$\begin{cases} \ddot{R} = -j\delta\dot{R} - jk_{12}\dot{S} \\ \ddot{S} = j\delta\dot{S} - jk_{21}\dot{R} \end{cases} \tag{1.14}$$

Substituting (1.13) in (1.14) we obtain:

$$\begin{cases} \ddot{R} + (k_{12}k_{21} + \delta^2)\, R = 0 \\ \ddot{S} + (k_{12}k_{21} + \delta^2)\, S = 0 \end{cases}$$

The solution of the first equation of this system amounts to:

$$R(z) = C_1 \cos(\sigma z) + C_2 \sin(\sigma z)$$

Where the two constants C_1 and C_2 are determined by the initial conditions and we defined $\sigma \triangleq \sqrt{k_{12} \cdot k_{21} + \delta^2}$.

Substituting this expression in the first equation of (1.13) we get:

$$S(z) = \frac{j}{k_{12}} \left[-C_1 \sin(\sigma z) + C_2\sigma \cos(\sigma z) + j\delta C_1 \cos(\sigma z) + j\delta C_2 \sin(\sigma z)\right]$$

Assuming the initial conditions $R(0) = A_1(0)$, $S(0) = A_2(0)$ to be known we can find the

expression for the constants C_1 and C_2:

$$C_1 = R(0), \qquad C_2 = \frac{1}{\sigma}\left[-jk_{12}S(0) - j\delta R(0)\right]$$

Substituting this constants in the equations for $R(z)$ and $S(z)$ we can write an equation that links the field distribution at the input with the field at any coordinate z, in fact:

$$\begin{bmatrix} R(z) \\ S(z) \end{bmatrix} = M \cdot \begin{bmatrix} R(0) \\ S(0) \end{bmatrix}$$

where the transfer matrix is:

$$M = \begin{bmatrix} \cos(\sigma z) - j\frac{\delta}{\sigma}\sin(\sigma z) & -j\frac{k_{12}}{\sigma}\sin(\sigma z) \\ -j\frac{k_{21}}{\sigma}\sin(\sigma z) & \cos(\sigma z) + j\frac{\delta}{\sigma}\sin(\sigma z) \end{bmatrix} \tag{1.15}$$

Assuming now to have an input only in the first waveguide, and thus $R(0) = 1, S(0) = 0$, the power in the two waveguides reads:

$$\begin{cases} P_1(z) = |R(z)|^2 = 1 - \frac{k^2}{\sigma^2}\sin^2(\sigma z) \\ P_2(z) = |S(z)|^2 = \frac{k^2}{\sigma^2}\sin^2(\sigma z) \end{cases} \tag{1.16}$$

where we have considered $k_{12}, k_{21} \approx k = \sqrt{k_{12}k_{21}}$. This is the general solution for a directional coupler with two non-identical waveguides, which is technically referred to as asynchronous coupler.

Conversely in the case of identical waveguides, that is for a synchronous coupler, the previous statement is rigorously true since $k_{12} = k_{21}$ and furthermore,

$$\delta = \frac{\Delta\beta}{2} = 0, \qquad \sigma = \sqrt{k^2 + \delta^2} = k$$

thus the system (1.16) simplifies to:

$$\begin{cases} P_1(z) = |R(z)|^2 = 1 - \sin^2(kz) = \cos^2(kz) \\ P_2(z) = |S(z)|^2 = \sin^2(kz) \end{cases} \tag{1.17}$$

We have therefore found the expressions of the power coupled in either of the two waveguides as a function of z, in the case of input injected in one single waveguide.

In the case of a directional coupler characterized by a coupling length L, and defining the following quantities $P_{BAR} \triangleq P_1(L), P_{CROSS} \triangleq P_2(L)$, the output power of the device will

be described by the following:

$$\begin{cases} P_{BAR} &= 1 - \frac{k^2}{\sigma^2}\sin^2(\sigma L + \varphi_0) \\ P_{CROSS} &= \frac{k^2}{\sigma^2}\sin^2(\sigma L + \varphi_0) \end{cases} \xrightarrow{\Delta\beta=0} \begin{cases} P_{BAR} &= \cos^2(kL + \varphi_0) \\ P_{CROSS} &= \sin^2(kL + \varphi_0) \end{cases} \tag{1.18}$$

Where we added the term $\varphi_0 > 0$ which is related to the portion of power exchange that occurs in the bent region which we neglected up to this point. In fact, as the two waveguides get close to each other power transfer will occur between them resulting in an additional contribution that will shift the response of the coupler as if it was longer than L. This quantity depends on multiple factors, namely the geometry of the bent region and coupling coefficient value with its dependence with the distance. Because of these complex relationships among the different terms, we do not offer an analytical study of the parameter φ_0 but rather an empirical characterization.

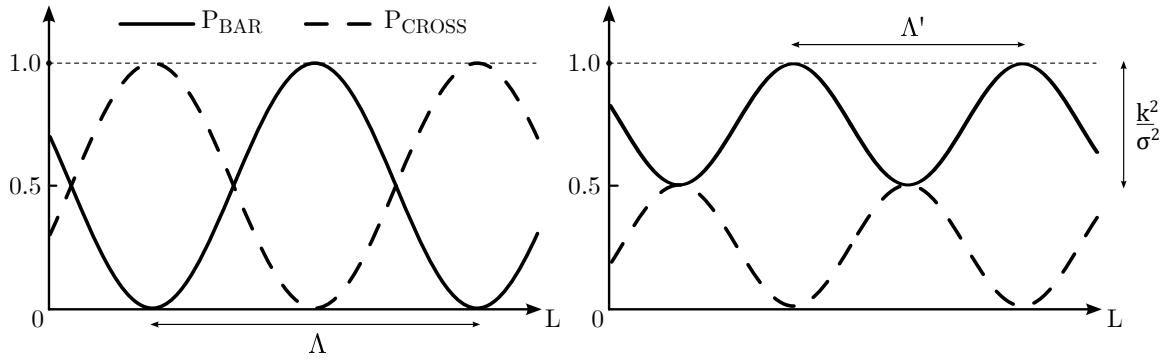

Figure 1.6: Output BAR power for a synchronous coupler (left) and an asynchronous coupler with $\Delta\beta = 2k$ (right) as a function of the coupling length L.

In figure 1.6 the output power at the BAR and CROSS ports of two directional couplers according to the equation (1.18) are represented. The graph on the left represents a synchronous coupler while the one on the right an asynchronous coupler, specifically with a value of detuning $\Delta\beta = 2k$. The most important differences between the two are highlighted in the figure:

- The period of oscillation of the power exchange in the case of an asynchronous coupler, $\Lambda' = \frac{\pi}{\sqrt{k^2+\delta^2}}$, is always shorter than the one for a synchronous coupler, $\Lambda = \frac{\pi}{k}$, and tends to zero as the detuning increases. This means that asynchronous couplers could be exploited to realize shorter devices. This fact is particularly evident in the case of a very weak coupling, in fact as $k \longrightarrow 0$ the period of the sinusoidal tends to infinity for a synchronous coupler, whilst for an asynchronous coupler the maximum length of the period is capped by the value of δ.

- The maximum exchange of power from the input waveguide to the adjacent one, $\frac{k^2}{\sigma^2}$, takes the maximum value of 1, thus total power exchange, in the case of a synchronous coupler and decreases as the detuning becomes greater. In the case represented in figure, with $\Delta\beta = 2k$, the maximum power exchange is equal to 50%. This means that by tailoring the value of the detuning one could realize an asynchronous coupler with the desired power exchange so that the working point for the desired device falls on a minima of the sinusoidal, where the slope with L is null. This is in fact, a working point much more resilient to fabrication errors.

1.2.2. Wavelength dependence

In this section it is analysed the wavelength dependence of the response of a directional coupler. The first term whose dependence on λ will be investigated is the coupling coefficient. [4] Recalling equation 1.8:

$$k_{il} = \frac{k_0^2}{2\beta_i} \cdot \frac{\iint \psi_l \Delta n_l^2 \psi_i^2 dxdy}{\iint \psi_i \psi_i^* dxdy}$$

we can observe that the first factor $\frac{k_0^2}{2\beta_i}$ has a clear dependence on the wavelength, in fact:

$$k_0 = \frac{2\pi}{\lambda}, \beta_i = \frac{2\pi}{\lambda} n_{eff}(\lambda)$$

Since the effective refractive index typically is only a weak function λ this factor will show a dependence of the type:

$$\frac{k_0^2}{2\beta_i} \propto \frac{1}{\lambda}$$

Regarding the overlap integral, as the wavelength increases the exponential tails extending in the cladding tend to expand thus increasing the overlap between the two modes. In fact, since both the exponential tails of the two modes expand, their superposition increases quadratically.

Therefore the overall dependence of the coupling coefficient is proportional to the wavelength, $k_{il} \propto \lambda$.

The second term which introduces a dependence on the wavelength is related to the detununig coefficient concerning not identical waveguides:

$$\delta = \frac{\Delta\beta}{2} = \frac{1}{2}\left[\beta_1(\lambda) - \beta_2(\lambda)\right]$$

Therefore, if the two waveguides are not identical $\delta \propto \frac{1}{\lambda}$.

Lastly, the third term which we need to consider is the initial phase φ_0 of which simple analytical expression can be provided. Nonetheless, since its value is strictly dependant on the coupling that is accumulated in the bent regions, it is reasonable to assume that it inherits from the coupling coefficient its wavelength dependence. In fact, the value of this phase is dependent on the overlap integral of the modes and the geometry of the bent region, the latter clearly is independent of the wavelength.

It is worth to point out that all the three factors are directly proportional to the effective refractive index which expression is of hard computation. In fact, from the theory of waveguides one can define the effective refractive index as $n_{eff} = \frac{\beta}{k_0}$ where β is the propagation constant of a given mode supported by the guiding structure. Unfortunately, the propagation constant of a guided mode is a complicated function of the refractive indices of core and cladding which are generally a function of the wavelength, although weakly. For these reasons is not straightforward to extract a reasonable estimation of the dependence of the effective refractive index on λ. [1]

1.3. Thermo-optic modulator

A useful device exploited in integrated optical circuits is the thermo-optic modulator. This device takes advantage of the thermo-optic effect, that is the variation of the refractive index of a material induced by a controlled temperature variation, to impose a desired optical-phase shift in a light carrier. The refractive index of a given material changes according to the following linear expression:

$$n(T) = n_0 + \alpha(T - T_0)$$

Where $\alpha = \frac{\partial n}{\partial T}$ is the thermo-optic coefficient and n_0 is the refractive index of the material at room temperature T_0. When a portion of length L of an optical waveguide is heated at a temperature T the light guided by it will accumulate an additional phase given by the following expression:

$$\Delta\varphi = \frac{2\pi}{\lambda}\Delta n_{eff}(T)L$$

This device allows to perform an active reconfiguration of the integrated optical chip as desired.

1.4. Mach-Zehnder interferometer

Mach-Zehnder interferometers are well known integrated optical devices widely used as frequency filters and optical switches. These structures are composed of three components, a first 3dB coupler — that is a directional coupler with splitting ratio equal to 50% —, a phase shifting section and lastly, another 3dB coupler.

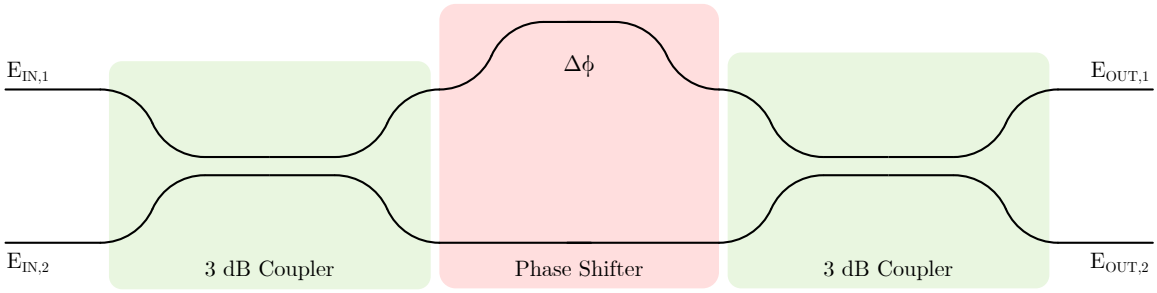

Figure 1.7: Schematic representation of a Mach-Zehnder interferometer.

Without going to much into the detail, the response of this device can be calculated by considering by considering the transfer function of the three components in succession.

The transfer matrix of both 3dB coupler is found considering equation (1.15) taking the length of the interaction region to be half the period of the sinusoidal response. Thus:

$$M_{3dB} = \frac{1}{\sqrt{2}} \begin{bmatrix} 1 & -j \\ -j & 1 \end{bmatrix}$$

The phase shifting region introduces an optical phase shift that is different for the two branches ϕ_1, ϕ_2. Its transfer matrix is simply given by:

$$M_{\Delta\phi} = \begin{bmatrix} e^{-j\phi_1} & 0 \\ 0 & e^{-j\phi_2} \end{bmatrix} = e^{-j\phi_1} \begin{bmatrix} 1 & 0 \\ 0 & e^{j\Delta\phi} \end{bmatrix}$$

Therefore the field at the output of the device is described by the following equation:

$$\begin{aligned}
\begin{bmatrix} E_{\mathrm{OUT},1} \\ E_{\mathrm{OUT},2} \end{bmatrix} &= M_{3dB} M_{\Delta\phi} M_{3dB} \begin{bmatrix} E_{IN,1} \\ E_{IN,2} \end{bmatrix} \\
&= \frac{1}{\sqrt{2}} \begin{bmatrix} 1 & -j \\ -j & 1 \end{bmatrix} e^{-j\phi_1} \begin{bmatrix} 1 & 0 \\ 0 & e^{j\Delta\phi} \end{bmatrix} \frac{1}{\sqrt{2}} \begin{bmatrix} 1 & -j \\ -j & 1 \end{bmatrix} \begin{bmatrix} E_{IN,1} \\ E_{IN,2} \end{bmatrix} \\
&= \frac{e^{-j\phi_1}}{2} \begin{bmatrix} 1 - e^{j\Delta\phi} & -j\left(1 + e^{j\Delta\phi}\right) \\ -j\left(1 + e^{j\Delta\phi}\right) & e^{j\Delta\phi} - 1 \end{bmatrix} \begin{bmatrix} E_{IN,1} \\ E_{IN,2} \end{bmatrix}
\end{aligned}$$

Assuming $E_{IN,1} = 1$ and $E_{IN,2} = 0$ the output power[4] can be computed yielding the following result:

$$\begin{cases} P_{BAR} &= \sin^2(\Delta\phi/2) \\ P_{CROSS} &= \cos^2(\Delta\phi/2) \end{cases}$$

Therefore, by controlling the phase difference between the two arms this device can be used to control the output power. In its simplest implementation the length of the two arms in the phase shifting region is different so that light propagating in them experience a longer or shorter optical path, thus accumulating a different phase. Since the optical path length is a function of the wavelength this device behaves like a filter, selecting some wavelengths at the BAR port and rejecting others in the CROSS port. Furthermore, a Mach-Zehnder can be used as an optical switch or a power modulator by actively controlling the optical path difference for example utilizing a thermo-optic modulator on one of the two arms.

1.5. Standard microfabrication techniques

A vast amount of techniques have been devised for the realization of integrated photonics circuits accurately and reliably, each method possessing particular advantages and disadvantages. The main materials utilized in the realization of photonics circuits are common glass — amorphous SiO_2 — and silicon pure or doped.

1.5.1. Glass integrated optics

Glass remains one of the most common materials for integrated optics thanks to its optical transparency at both visible and IR wavelengths as well as its low cost and strong resistance to high optical intensities. As it has been discussed in this chapter the property

[4] The output power has been expressed with the same notation utilized for directional couplers, $P_{BAR} = |E_{OUT,1}|^2$, $P_{CROSS} = |E_{OUT,2}|^2$.

of optical waveguiding relies on the difference in the index of refraction between the guiding region and the surrounding substrate, thus the various fabrication technique are employed to realize an index contrast in the material and can be distinguished based on the processes involved. One approach is *thin film deposition* which consists in depositing layers with different refractive index on top of the glass substrate. With these techniques the confinement of light is achieved in thin layers of materials deposited one after the other so to achieve the desired index contrast. A different approach consists instead in a localized modification of the material to induce changes in the refractive index. These techniques are grouped under the name of *index modification techniques* and comprehend, among others, femtosecond laser writing, which will be detailed in the following chapter and applied in this thesis work. Femtosecond laser writing, as well as UV laser writing, is based on the permanent modification of the material that ensuing from a localized injection of energy with laser intensities. A general overview of the fabrication techniques of photonics circuits on glass is schematized in figure 1.8. [5]

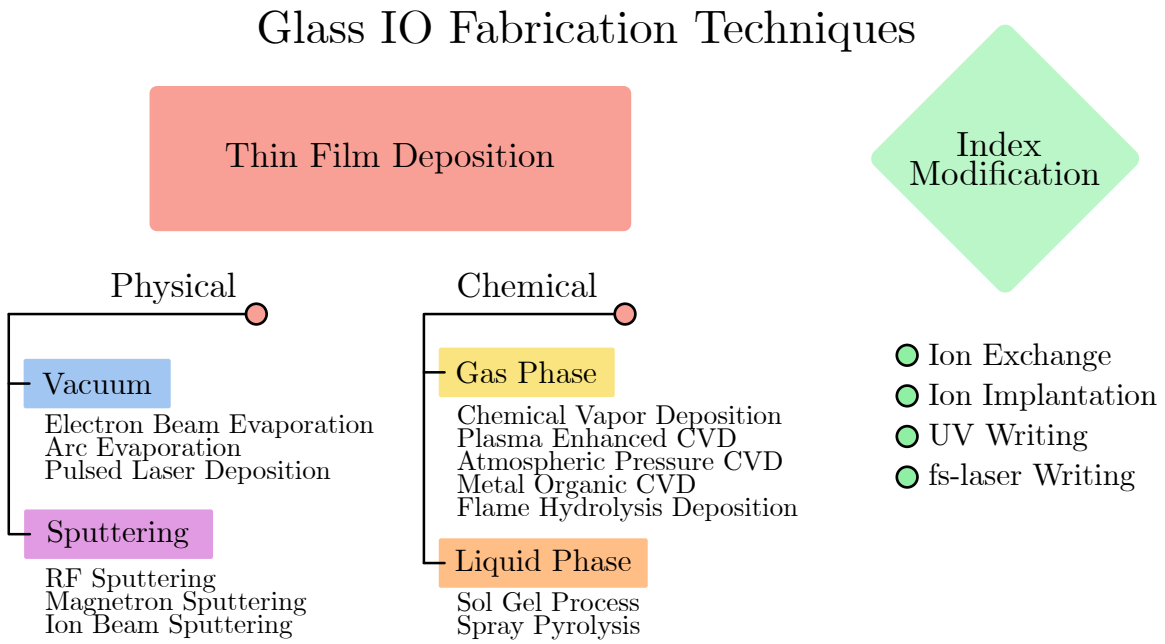

Figure 1.8: Schematic classification of glass microfabrication techniques for integrated optics (IO).

1.5.2. Silicon integrated optics

Silicon is a particularly popular material for the fabrication of integrated optical circuits as it exploits the great many and well developed techniques utilized in the manufacturing of electronic components, most of which coincidentally are listed in figure 1.8. The choice of this material presents both advantages as well as disadvantages. In fact, its integration

with electrical circuits is rather straightforward, enabling the manufacturing of compact and monolithic optoelectronic devices. Compactness is particularly driven by the strong confinement of light that can be achieved exploiting the high index contrast between silicon (n = 3.45) and SiO_2 (n = 1.45). But unfortunately, it comes with some downsides concerning its optical properties. Firstly, Si is not transparent in the visible and near infrared portion of the spectrum which limit the realm of application in which it can be exploited. Furthermore, due to the considerable index and modal mismatch between silicon waveguides and standard optical fibers, their coupling comes with high losses. Even though recent advancements have shown promising results in lowering such losses. [6]

2 | Femtosecond Laser Micromachining

The microfabrication technique known as Femtosecond Laser Micromachining (FLM) consists in focusing laser pulses of the order of hundreds of femtoseconds onto a material so to selectively determine a change in its properties. The first reported application of this technique dates back more than two decades is a study carried out by Davis et al. [7] who exploited it to fabricate optical waveguides in a fused silica substrate with the goal of realizing a three dimensional optical circuit for telecommunication purposes. After years of study, nowadays this technique has proven to be extremely powerful and versatile allowing to realize almost arbitrary three dimensional structures in a host of materials with different manufacturing techniques: FLM can be used to induce controlled modifications inside a material, most notably to induce smooth modifications of the refractive index. With this approach high quality optical circuits can be realized in various types of glass (e.g., alumino-borosilicate glass and fused silica) and other materials (such as polymers and wide range of crystalline materials e.g. Lithium niobate [8]), working in a range of different wavelengths spanning from the IR, to the visible and to the UV. By combining femtosecond laser irradiation and chemical etching a selective removal of the material can be realized granting the ability to manufacture empty channels and chambers. Common substrates employed in this kind of fabrication technique are fused silica and alumino-borosilicate glass. This technique will be detailed in the section 2.4. Finally, FLM can be utilized as an additive manufacturing technique. In fact, femtosecond laser pulses are employed to realize a variety of micro-objects, through two photon polymerization of resins. [9]

Of particular importance are the first two techniques mentioned, which, combined, allow the realization lab-on-chips (LOCs) on glass substrates, in which optics and fluidics work at unison to create devices capable of complex analyses as single cell manipulation, detection and microscopy. Such kind of devices are the focus of the thesis and will be detailed in the following.

The great advantage of this fabrication technique, as already mentioned, is the capability to realize arbitrary three dimensional structures which are attained by translating the sample with respect to the incoming laser beam, as described in section 2.2.1. Furthermore, even complex structures can be realized in a reasonably short amount of time, in a single fabrication session (unlike lithographic techniques which require multiple maskings) and with relatively small prototyping effort. In fact once the optimal parameters are identified, changing the geometry of the structure is just a matter of reprogramming the translations of the sample. The capability to fabricate multiple structures in a single session is particularly important as it allows for the perfect alignment of all the components (for example optical and fluidic) which would otherwise be hard to achieve in a multiple step process.

2.1. Physical mechanism

The physical mechanism that lies behind the technique of femtosecond laser micromachining is the modification of the transparent material. Such modification occurs as the consequence of a localized deposition of energy realised by the femtosecond laser pulses, which ionize a large density of electrons thanks to the intense electric field. This sudden deposition of energy inside the material causes a non reversible change in the material. Transparent materials are characterized by an energy gap $\mathcal{E}_G$ between valence and conduction bands that is higher than the energy $h\nu$ of a single photon in the visible and IR spectrum. This means that linear absorption events cannot determine interband transitions in these materials. In fact, electrons can be promoted to the higher band only by non linear absorption phenomena, which can occur at a significant rate only in the presence of an intense electric field. The non linear absorption phenomena, represented in figure 2.1. which concur in the process of permanent material modification are: 1) multiphoton ionization, 2) tunneling and 3) avalanche ionization.

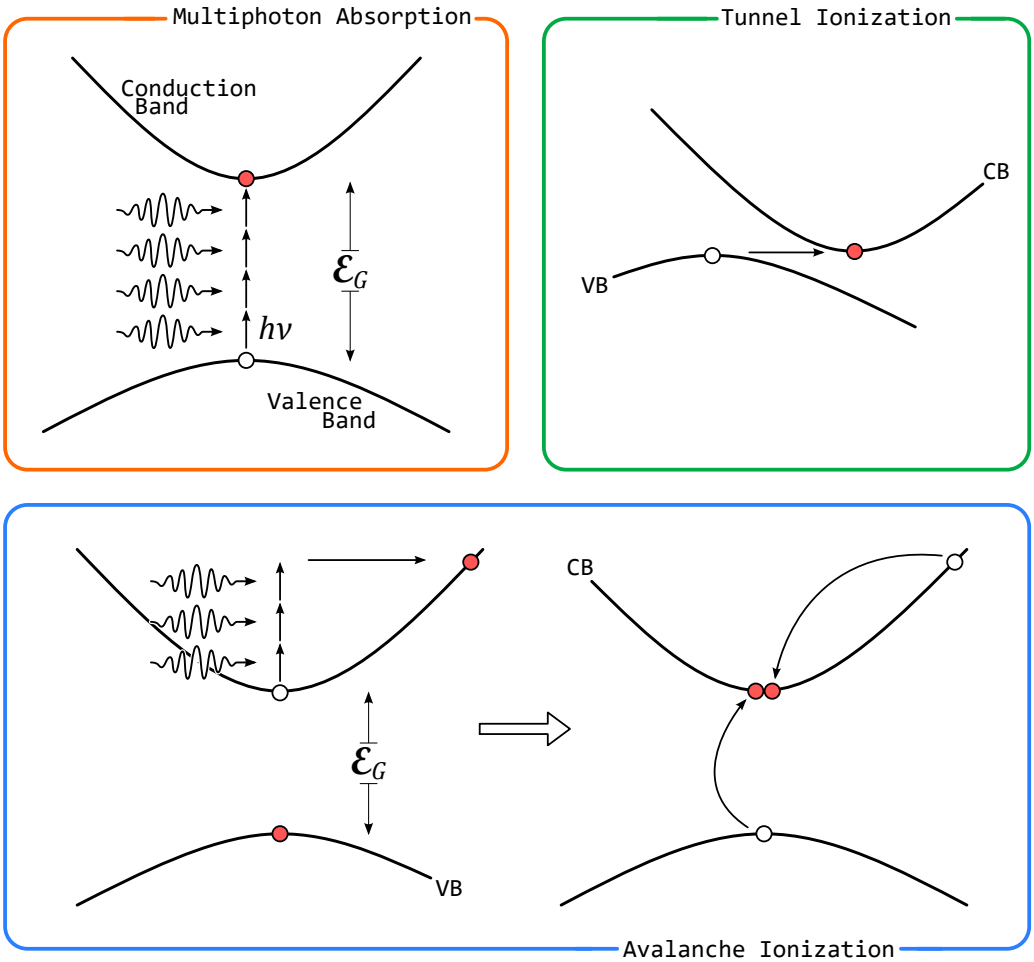

Figure 2.1: Schematic depiction of the nonlinear ionization mechanisms.

Multiphoton absorption relates to the simultaneous absorption of m photons such that $m \in \mathbb{N}$ and $mh\nu > \mathcal{E}_G$. Tunneling ionization occurs when the intensity of the externally applied electric field is so high to become comparable with Coulomb potential of the nucleus which keeps the electron bound to it. In this case the external electric field is so intense to distort and lower the potential barrier enabling the electron to tunnel from the valence to the conduction band. At high field intensities these two processes are in competition and the one which dominates can be discerned studying the so-called Keldish parameter:

$$\gamma = \frac{\omega\sqrt{2m^*\mathcal{E}_G}}{eE}$$

where m^* and e are respectively the effective mass and charge of the electron and E is intensity of the applied electric field, oscillating at frequency ω. If the parameter $\gamma >> 1.5$ multiphoton absorption dominates over the other, conversely if it is $\gamma << 1.5$ tunneling ionization gives the largest contribution. For waveguide fabrication in dielectrics the laser

properties are selected such that, in combination with the properties of the material, the result is of $\gamma \sim 1$ so that both processes of multiphoton absorption and tunnelling concur in the ionization of the material. The mechanism underlying the process of avalanche ionization is the following: let us suppose that an electron is free at the bottom of the conduction band of the material; said electron, when exposed to an intense electric field, gets accelerated and thus gains a certain amount of kinetic energy; when its energy exceeds the bandgap energy it can ionize another electron at the top of the valence band by sharing its kinetic energy with it. At the end of this process both electrons will sit near the bottom of the conduction band, where the process can readily start again. It is intuitive to understand that even a relatively small density of free electrons can grow exponentially following this process. It is worth highlighting that, for this process to occur, it is required the presence of a "seed", a small density of free electrons in the conduction band. [10]

When a "long" pulse, with a duration longer than a few picoseconds, is shone on the transparent material the peak intensity of the electric field is typically too low to allow both multiphoton and tunneling ionization, even with a rather high total pulse energy. In this scenario, the only process which can occur is avalanche ionization starting from a seed of electrons due to impurities and dislocations in the material. Since the number of such defects is poorly controllable, the absorption process is not reproducible and the selective modification unattainable. When "short" pulses, of a duration shorter than a picosecond, are delivered to the material the peak intensity is high enough to trigger multiphoton and tunneling ionization which give raise to a modest and controlled density of free electrons. These electrons then, act as a seed for the process of avalanche ionization which determines a vast increase in the electron density. As the electron density rises, the plasma frequency approaches the frequency of the laser,[1] at which point the material becomes strongly absorbing allowing to deposit a substantial amount of energy in the focal volume of the laser beam. The energy absorbed by the plasma is then transferred to the lattice in a time scale much longer than that required for the formation of the plasma.

The modification of the material resulting from this processes of nonlinear absorption depends on several parameters ranging from exposure parameters (such as pulse energy and duration, repetition rate, wavelength, ...) to material properties (like energy bandgap, thermal conductivity and others). Such modifications are permanent when the deposited energy surpasses a given threshold and can be broadly classified in three categories depending on the laser fluence:

[1] We define plasma frequency the quantity $\omega_P = \sqrt{\frac{n_e e^2}{m^* \varepsilon_0}}$, with n_e representing the density of free electrons in the plasma.

- A *smooth modification*, resulting in a positive or negative change in the refractive index, is achieved with a fluence just above the threshold. This is the regime that allows the fabrication of optical waveguides.
- Increasing the fluence sub-wavelength *nanogratings* are formed, which represent a key ingredient for the realization of channels and such empty structures as described in the section 2.4.
- Finally, for an even greater fluence, a *disruptive modification* is observed. In this regime the thermal shock is so important to determine micro-explosions which detach material leaving holes and voids on the substrate. This is the process that is exploited for the fabrication of the shallow trenches described in the section 2.6.

2.2. Irradiation parameters

The permanent modification induced in the material is strongly dependant on the characteristics of the pulse delivered on it as well as the material properties. As it has been already discussed, three main regimes of modification can be identified based on the fluence of the irradiation which is in turn dependant on several parameters. Besides the average power of the irradiation also the translation velocity v of the focal spot relative to the substrate, the dimension of the focal spot w_0, and repetition rate f concur to the determination of the fluence deposited on the material. In fact, the fluence is roughly estimated to be $F \propto w_0 f/v$. [11] In the next sections some of this parameters are examined more in depth.

2.2.1. Writing geometries

Two are the possible fabrication geometries in FLM: longitudinal and transverse geometry, which respectively refers to the direction in which laser beam and sample are translated one with respect to the other as exemplified in 2.2.

- In the *longitudinal* configuration the sample is translated along the direction of propagation of the laser beam. The main advantage of this geometry is that the waveguides written in the material are intrinsically symmetric however their maximum length is constrained by the focal length of the focusing objective. Furthermore spherical aberrations due to the propagation inside the material degrade the quality of the focal spot.
- In the *transverse* geometry the sample is translated perpendicularly to the laser

beam allowing complete freedom[2] regarding the structures inscribed in the material. The drawback of this geometry is the strong asymmetry of the focal spot (more details on the dimension of the focal volume are reported in the section 2.2.2).

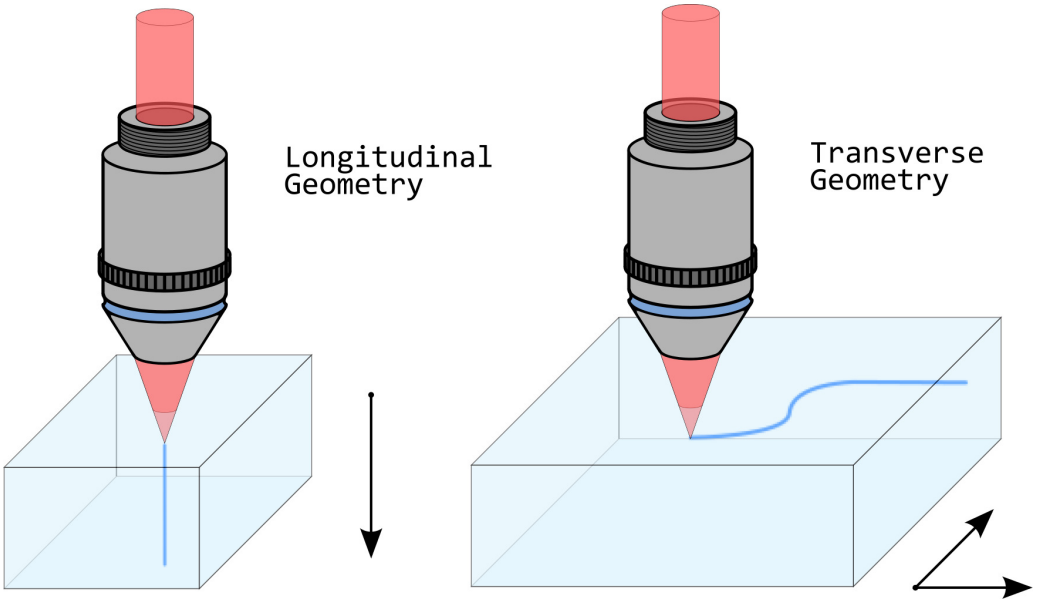

Figure 2.2: Schematic representation of the two FLM fabrication geometries. The arrows represent the directions of translation of the sample with respect to the laser beam.

2.2.2. Dimensions of the focal volume

Femtosecond laser micromachining requires a tight focusing of the laser beam on the sample as it is of paramount importance to obtain a high peak intensity so to drive non linear absorption processes. [12] Neglecting spherical aberrations[3] the spatial intensity profile of the laser beam is well represented by Gaussian optics, according to which the diffraction limited minimum waist radius (half of the spot size) is given by:

$$w_0 = \frac{M^2 \lambda}{\pi \mathrm{NA}}$$

Where M^2 is the Gaussian beam propagation factor, which describes the quality of the beam[4], NA is the numerical aperture of the focusing objective and λ is the free space wavelength.

[2] Besides the depth of the structures which is again limited by the focal length of the objective.

[3] Spherical aberration are admittedly present, unless corrected, especially because of the air-glass interface that is encountered when focusing in the depth of the material.

[4] This factor is expressed as the ratio between the divergence of a generic multimode beam Θ and the diffraction-limited beam divergence θ_n of a Gaussian beam: $M^2 = \frac{\Theta}{\theta_n} \geq 1$ [13].

The Rayleigh range z_0 (half of the depth of focus) inside a transparent material of refractive index n is given by:

$$z_0 = \frac{M^2 n\lambda}{\pi \mathrm{NA}^2}$$

Therefore, the focal volume assumes the shape of an ellipsoid of longitudinal dimensions of $2z_0$ and diameter $2w_0$ thus possessing an aspect ratio of $\frac{\mathrm{NA}}{n}$.

2.2.3. Laser repetition rate

The time required for heat diffusion from the focal spot to the bulk of the material defines two working regimes for the repetition rate of the laser: high and low frequency regimes. The heat diffusion time in glass is estimated to be around 1 μs therefore the transition between the two regimes occurs around a pulse repetition rate of 1 MHz.

In the low frequency regime ($1 \div 200$ kHz) the period between consecutive pulses is longer than the heat diffusion time and the material modification is produced by individual pulses, since the energy deposited by a pulse diffuses away from the focal spot before the next pulse arrives. Conversely, in high frequency regime ($5 \div 20$ MHz), several pulses impinge on the material and deposit energy in the focal volume faster than it can be carried away thus a cumulative modification takes place.

Further distinctions among the two regimes concern the pulse energy and the necessity of overlap between consecutive pulses. In the low frequency regime the pulse energy is typically quite high allowing to work with low focusing objective which grant a longer focal length and more freedom in the geometry of the devices. The downside of this regime is low translation speed that is required to have a good overlap between consecutive pulses (which is, for example, paramount to achieve a smooth waveguide). Clearly, in the high frequency regime, this two considerations are reversed: albeit allowing faster translation velocities a high focusing objective is required posing a constraint on the 3D fabrication capabilities.

Recently it has been found an intermediate working regime around the threshold frequency (200 kHz $\div$ 2 MHz) which has been shown to give the best fabrication results so far.

2.2.4. Laser polarization

The polarization direction of the laser beam is particularly important in the regime of nanograting formation. In fact, as described in the section 2.4 the nanogratings form perpendicularly to the direction of the polarization which, in turn, constitutes an important

factor in the process of chemical etching necessary for the realization of microchannels. This phenomena poses a constraint on the direction in which the channels can be formed unless the polarization is controlled externally and synchronised with the translation of the sample.

2.3. Fabrication of optical waveguides

One major application of FLM is the fabrication of integrated optical circuits whose fundamental component is the optical waveguide. As anticipated in section 2.1 such devices are realized by forming a smooth modification in the glass substrate showing a refractive index contrast that is sufficient to confine light in its core. The entity of the index contrast is around $\Delta n \sim 10^{-4} \div 10^{-2}$ comparable with conventional optical fibers. [8]

While the regime to fabricate such devices has been well defined, the physical principles that govern this type of modification has not yet been fully unravelled. Several mechanisms appear to be responsible for this effect but none of the explanations results to be entirely satisfactory. A complete review of such possible physical phenomena is the one presented by Osellame et al. [10] of which here are presented it basic concepts.

A first mechanism involves the formation of colour centers, that is defects in lattice, caused by the irradiation of the femtosecond laser. Such color centers modify by the Kramers-Kroenig mechanism the refractive index at the wavelength of interest. An alternative phenomenon which plays a role in the formation of this modification is a thermally induced densification of the material. In fact the small volume of glass in focal spot of laser is subject to rapid heating (even of several thousand degrees) which may generate a shock wave because of the rapid expansion, leading to a compression and in turn an increase of the refractive index. [14] An ulterior explanation could reside in a direct structural change in the chemical bonds of the material induced by the femtosecond pulses which in turn lead to a localized change in the density. Yet another mechanism consists in non-uniform cooling. After the irradiation a small volume of glass melts due to the excessive heat accumulated, then, as heat is dissipated outwards of the irradiated region, the external layers cool off and solidify into a lower-density structural arrangement. As the cooling continues inwards the the inner region of the modification is left under pressure and solidifies into a higher density phase, resulting in a refractive index contrast. In practice all these mechanisms may contribute to the determination of such modification and their relative contribution is difficult to disentangle.

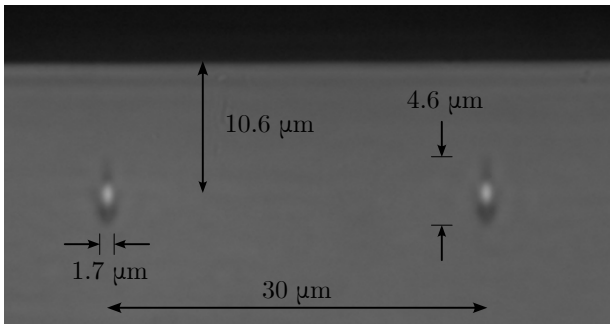

Figure 2.3: Optical microscope image of two FLM-written waveguides in Cornig Eagle XG, 50x magnification.

2.3.1. Waveguides in alumino-borosilicate glass

Alumino-borosilicate is one of the most used glass substrates used for the realization of integrated optical circuits employing FLM. Eaton et al. demonstrated that at high repetition rate (∼1 MHz) a strong heat accumulation effect gives rise to the realization of high quality waveguides reporting propagation losses as low as ∼0.3 dB/cm at 1550 nm as well as good coupling of FLM written waveguides with standard telecom fibers. [15] A subsequent study exploiting such waveguides reported on bending losses as low as ∼0.3 dB/cm at 800 nm and a curvature radius of 30 mm confirming the possibility of realizing more complex photonics circuits with curved waveguides. [16] Arriola et al. [17] reported of a novel fabrication technique involving a two step process, first the waveguides are written in the glass substrate which is then subjected to a thermal annealing treatment that has been shown to eliminate the outer ring profile enabling single mode operation and significantly decreasing the bending losses of such waveguides allowing for sharper bends.

2.3.2. Waveguides in fused-silica

Both pure and doped fused silica have been used to realize low loss optical waveguides. Nasu et al. [18] demonstrated that propagation losses as low as 0.12 dB/cm at telecom wavelength can be attained exploiting femtosecond laser pulses at a 1 kHz repetition rate. To realize symmetric waveguides, while avoiding optical damage, multiple laser scans where delivered on the glass, with a low NA objective, overlapping them with some displacement in the direction of the core width. Working in a different regime Shah et al. [11] reported on the realization of low loss waveguides, with propagation losses around 1 dB/cm, at telecom wavelength by shining fs laser pulses at a 1 Mhz repetition rate on fused silica.

2.4. Microchannel realization by FLICE

Microchannels and other empty structures can be realized with the technique called FLICE, which stands for Femtosecond Laser Irradiation followed by Chemical Etching. As the name suggests, it consists in a two step process: a permanent modification of the material caused by non linear absorption of femtosecond laser pulses, as described in the section 2.1, followed by the removal of the modified zone in an acidic or basic solution bath. The principle lying behind this process, as it will be detailed in the next sections, is that the permanent modifications in the material, caused by the irradiation with a femtosecond laser, determine a localized and controlled increase in the etching rate which, in turn, allows the selective removal of material and thus the realization of buried empty channels and such in the desired geometry.

2.4.1. Nanograting formation

It has been shown that the increased etching rate is linked to the formation of nanogratings in the material induced by the laser irradiation. One of the most accredited theories on the physical processes involved in the formation of such structures deals with a transient nanoplasmonic model. According to this model the starting point is the formation of hotspots for ionization in the focal volume of the laser in correspondence with defects or color centres. Such hotspots then, evolve into spherically shaped nanoplasmas due to a memory effect that increases the ionization rate of subsequent pulses. An effect of field enhancement at the boundaries of such droplets of nanoplasma causes them to grow asymmetrically, taking before the shape of nanoellipsoids and than that of nanoplanes. Such nanoplanes are all aligned perpendicularly to the direction of the laser polarization. Finally, the nanoplanes which are initially aligned but randomly spaced, start to influence the propagation of light upon reaching a critical density of electron plasma. Because of this effect the nanoplanes begin to space themselves with a periodicity of λ/n thus forming a sub-wavelength nanograting. [10]

Recent studies have shown that the formation of these nanograting is accompanied by the formation of a porous material made of nano-scale bubbles which determine a densification of the surrounding volume determining the accumulation of stress in the material. This stress is responsible for variations in the bond angle in the SiO_2 matrix which is in turn cause of the faster etching rate in the laser affect zone. Furthermore, it is believed that the presence of this porous structures may also favour the diffusion of the etchant inside the material. [20]

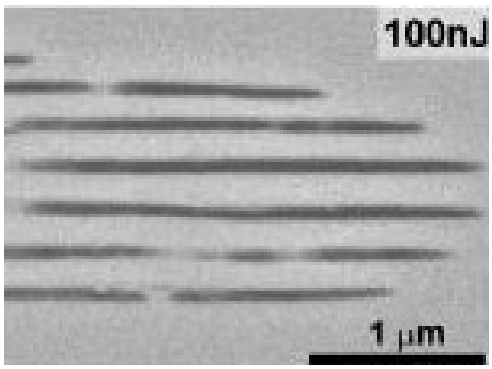

Figure 2.4: SEM image of the nanogratings, after the ecthing process, formed in fused silica thanks to FLM. [19]

As anticipated in section 2.2.4 the polarization of the laser plays a major role in the etching rate enhancement, the reason behind it is that the nanograting always self align orthogonally to the polarization direction. When the polarization is orthogonal to the translation direction the nanograting are aligned with the direction of translation and connect longitudinally, thus favouring the diffusion of the etchant. For these reasons the control of the laser polarization direction is critical for the realization of microfluidic structures exploiting this technique.

2.4.2. Chemical Etching

As anticipated, the second and final step of the manufacturing technique called FLICE, consists in chemical etching which takes place in a bath of aqueous solution with a strong acid or a strong basis. The best results that can be found in the literature regarding this technique concerning chemical etching of fused silica glass with hydrofluoric acid (HF) following the reaction equation:

$$SiO_2 + 4\,HF \longrightarrow SiF_4 + 2\,H_2O$$

Recently, the use of potassium hydroxide has also become particularly widespread as it offers, at the price of much slower etching, a high selectivity which allows the manufacturing of longer channels. [21] Novel studies have analysed this technique applied to aluminoborosilicate glass[5] (like the commercial Eagle XG® sold by Corning) demonstrating the use of both HF and KOH showing showing promising results. [22, 23]

[5] Admittedly the reason behind the enhanced etching rate in this type of material is still under study as the nanograting structure typical of fused silica glass was not observed.

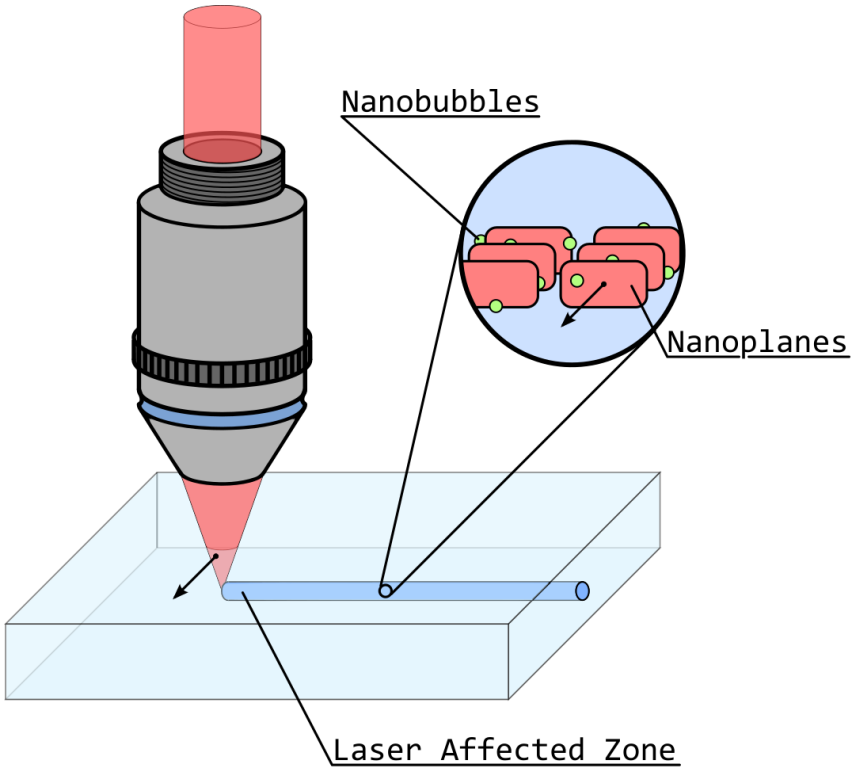

Figure 2.5: Schematic representation of the formation of nanogratings and nanobubbles. The arrows represent the direction of the polarization of the laser.

2.5. Microchannel properties

The FLICE technique allows the fabrication of both surface channels as well as buried ones, even with a dead end. Regarding the first type of channels, there is no limitation on the channel length and shape as the etchant is able to attack the entire volume of the channel provided the easy access from the open surface. When it comes to buried channels, and especially channels with a dead end, one has to face limitations with length, shape and aspect ratio of the channels. In fact, while having the advantage of not requiring a subsequent sealing procedure, in the fabrication of buried channels one faces the issue of a limited diffusion of the etchant inside it. The formation of the channel starts from the open surface, or surfaces, and progressively continues in the depth of the channel as the reaction products are removed and the etchant diffuses further in. The longer becomes the the channel, the harder it is for fresh etchant to replenish the exhausted one, thus the ecthing rate steadily decreases with its length. This causes three issues: 1) the channel are formed with a conical shape since the portions closer to an open surface are subject to a faster etching than deeply buried ones; 2) the maximum length is limited as the etching rate becomes negligible; 3) there is a trade-off in the possible aspects ratios attainable by

tuning the concentration of the etchant.

One method that allows to compensate the conical shape of the channels is to irradiate a channel with a conical shape that is complementary to the one otherwise naturally formed, as represented in figure 2.6. This allows to compensate for the lower ecthing rate in the depth of the channel by providing a increased diffusion of the etchant. This technique has proved to be capable of realizing dead-end buried channels with an almost uniform cross-section as well as more complicated structures thanks to the unique control over the channel cross-section.

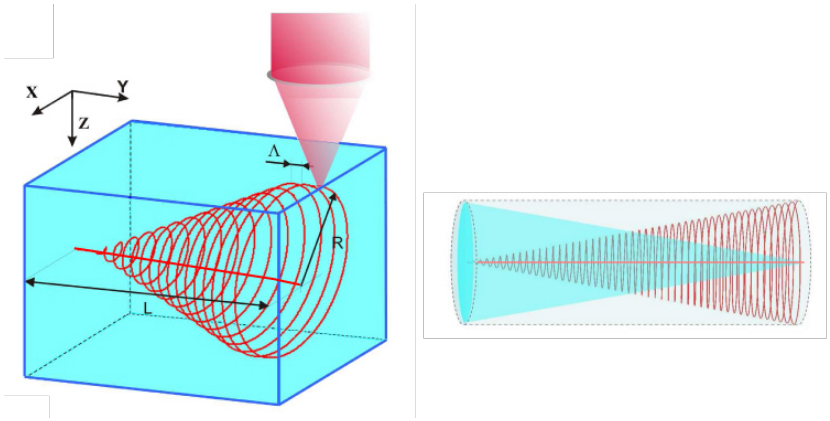

Figure 2.6: Schematic diagram of the conical spiral inscription for channel form factor compensation. [24]

2.6. Thermal Shifters for optical circuits

A common element that is often integrated with integrated optical circuits is thermal shifters. These device allow to modify the optical phase of the light in the waveguides and effectively reconfigure or tune the optical circuit itself as demonstrated by Flamini et al. [25]. Firstly, the optical circuit is written in the glass substrate exploiting FLM. Secondly, a layer of gold, with a thickness of the order of 50-100 nm, is deposited onto it and successively, thanks to femtosecond laser ablation of the gold layer, resistors of desired dimensions and electrical resistance can be patterned onto the surface. Finally, the resistors are connectorized to a voltage supplier which imposes a current flow inside them. Because of the Joule effect the resistors dissipate a power $\mathcal{P}$ which determines a temperature-induced change in the refractive index of the substrate which is linear with the dissipated power. Therefore, tuning the voltage applied to the resistors one is able to induce an optical phase difference between laser beams propagating inside two or more adjacent waveguides. Furthermore, as demonstrated by [26], employing once again the capabilities of FLM to dig trench-like structures around the optical waveguides under the

thermal shifters, and performing a pulse shaping of the electrical signal one can obtain a fast switching of the optical phases of the input laser beams while keeping the power consumption to a minimum.

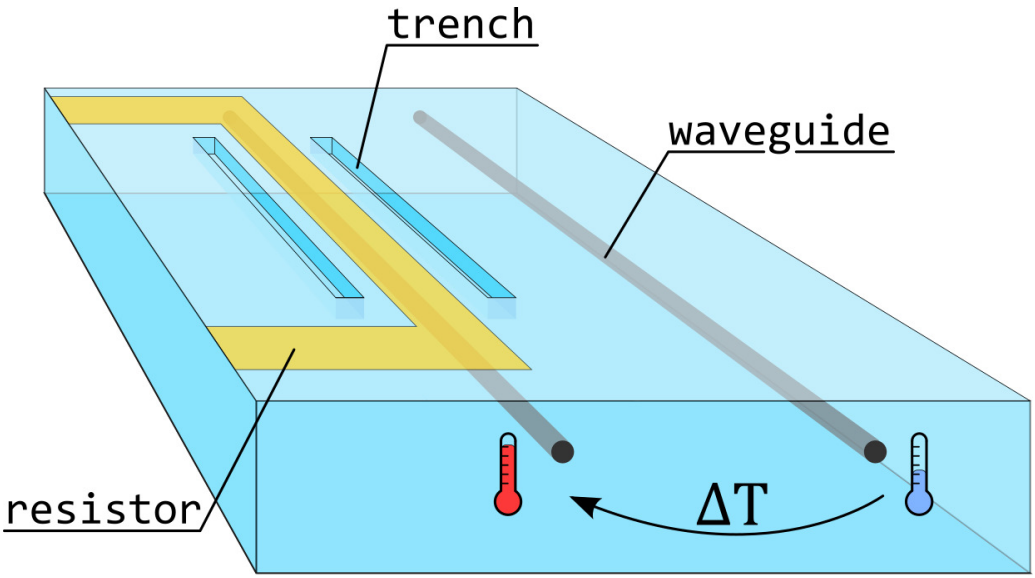

Figure 2.7: Scheme of a thermal shifter with trenches.

3 | Structured Illumination Microscopy

Optical microscopy constitutes one of the major techniques employed for imaging and study of biological samples as it allows to retrieve morphological and structural information from various specimen, ranging from single cells up to macroscopic tissues and small organisms. The main factors that hinder the possibility to image smaller and smaller samples are aberrations and diffraction. There are many types of aberrations, each with a different cause such as non-ideal optical elements, imperfect alignment, wavelength-dependence of the refractive index of the optical elements and others. All Aberrations contribute to the reduction of the image quality that can be retrieved from the sample, for example due to distortion or blur, and effectively limit the resolution of the system. [27] Luckily, many techniques can be adopted, often at the price of a more complex, or more expensive optical system, to alleviate or even eliminate the effect of such aberrations. Even in the absolute absence of aberrations though, a real optical system has limited resolution. In other words, there is an lower limit to the physical dimensions of the features that can be discerned in a sample. This is generally referred to as the Abbe limit or diffraction limit. Both the finite wavelength of illumination and the finite aperture of the optical elements determine this limit in the resolution of the system. In fact, given the illumination wavelength, λ, the refractive index of the medium, n, and the numerical aperture of the system, NA, the lateral and axial resolution of a standard optical microscope is given respectively by:

$$\delta\rho \simeq \frac{\lambda}{2\mathrm{NA}} \qquad\qquad \delta z \simeq \frac{2n\lambda}{\mathrm{NA}^2} \tag{3.1}$$

The lateral resolution $\delta\rho$ describes the minimum distance at which two distinct point-like sources can be distinguished, any closer than this value and the two points are indiscernible from a single one. In other words, it describes the limit on the size of the features of the sample which can be distinguished. The axial resolution δz is linked to the optical sectioning capability of the system which can be described as the possibility to localize

the axial position of a plane source. This capability allows to perform a 3-dimensional imaging of a sample since it gives the possibility to localize its features not only on the plane but in space. The diffraction limit to the resolution of optical microscope has stood unchallenged up until the recent years when several techniques have been demonstrated to be able to surpass this limit and offer a super-resolution. These microscopy techniques include near-field scanning, stimulated emission depletion, localization of photoactivated labels and others. Among such methods, the one we are interested in, is Structured Illumination Microscopy (SIM) which will be detailed in the following paragraph.

The basic concept of structured illumination microscopy is to illuminate the sample with light that exhibits some kind of spatial structure rather than a uniform light. Differently from standard widefield microscopy SIM requires the acquisition of multiple images that are combined in post-processing to obtain the final image. Each of the images are taken with a change of the non-uniform illumination pattern such that the summation of illumination patterns averages out and each sample point is subject to the same illumination intensity on average. At the price of a more complicated acquisition process various SIM techniques have been devised to obtain a resolution beyond the diffraction limit and confer optical sectioning to the system. [28]

The technique that will be detailed in this work is what is referred to as super-resolution SIM devised by Gustafsson et al. [29]. This technique exploits structured illumination to surpass the diffraction limit by a factor of 2 in a standard widefield fluorescence microscope. Furthermore, in a successive work Gustafsson demonstrated the possibility to exploit this same technique combined with a high illumination to reach theoretically unlimited resolution. In these technique it is utilized an illumination intensity is strong enough to give rise to a non-linear response of the fluorophores. In fact, fluorophores respond linearly to the illumination, absorbing a photon and emitting one at lower energy. Yet, on average each molecule can absorb and emit a photon per lifetime τ, which is the fluorescence lifetime of that particular electronic state of the fluorophore. Therefore, if the illumination is strong enough — thus the photon flux is high enough — the fluorophores are brought to saturation and cannot respond linearly to the illumination. If the sample is illuminated with a sinusoidal pattern below the saturation point, the ensemble fluorophores will emit light with the same spatial modulation yet rescaled in intensity. Instead, if the intensity near the peaks of the sinusoid is above the saturation threshold, the response of the fluorophores will be a nonlinear shape, a sinusoid with its top portion flattened out. This nonlinear fluorescence contains harmonics with spatial frequencies multiple of the real illumination pattern which amplify the capability of the technique enabling to reach even higher resolutions. [30]

3.1. Super-resolution SIM

The principle that lies behind the power of structured illumination microscopy can be understood considering the known effect of the moiré fringes, exemplified in figure 3.1. When two fine patterns are superimposed a beat pattern appears in the multiplication of the two. The key point, that is worth highlighting, is that beat pattern exhibits a spatial frequency that is smaller than either the initial patterns. The importance of this statement will be made clear in the following.

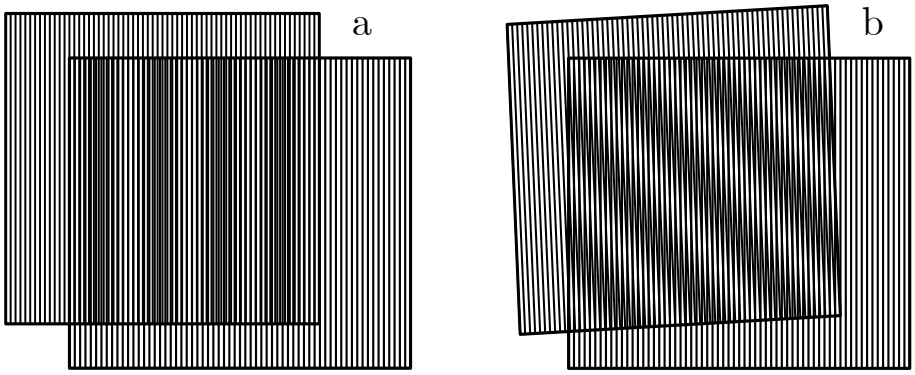

Figure 3.1: Representation of the moiré fringes obtained by the superposition of two patterns. On the left (a) two patterns with different frequency are superposed whereas, on the right (b), two patterns with the same spatial frequency are superposed at an angle.

In the case of structured illumination microscopy, the illumination pattern clearly constitutes one of the two patterns, while the other is constituted by the unknown sample structure, or rather the unknown distribution of fluorophores which reflects the sample structure. In fact, any spatial feature of the sample can be considered as represented by the sum of infinite patterns of ever increasing spatial frequency. Therefore, by illuminating the sample with a pattern gives raise to moiré fringes, whose beat pattern has a spatial frequency smaller than the original ones, that translates information of the sample, initially encoded at a high spatial frequency, to a smaller and detectable spatially frequency. This is the concept that lies behind the super-resolution capability of this technique: high frequency information — that is, high resolution information — is brought to a smaller and resolvable spatial frequency.

To comprehend which is the quantitative improvement on resolution granted by this technique, with respect to standard widefield fluorescence microscopy, it is useful to reason about the sample structure in reciprocal space, that is the space of the Fourier transform of the sample structure in the real space. In this representation the low resolution information of the sample resides close to the origin, whereas high resolution information

resides further away, at high spatial frequency. With a conventional microscope of lateral resolution $\delta\rho$, limited by diffraction, we can only obtain information that falls in a circle of radius $1/\delta\rho$ centred on the origin in reciprocal space. Any information that is encoded at a spatial frequency that does not belong to this disk is not observable.

Structured illumination does not alter the dimension of this disk in reciprocal space but it shifts high-frequency information, that lays outside of it, into this region making it observable. When the sample is illuminated with a structured light, the image that is captured by the microscope contains, on top of the normal image, also moiré fringes arising from the pattern itself and information that falls outside the observable region. The former contribution conveys information that lied inside the observable region while the latter contains high-frequency information whose position has been offset by an amount equal to the spatial frequency of the pattern. Clearly, only the frequency information whose moiré fringes fall inside the observable region can be accessed. Visually it corresponds to the region of reciprocal space constituted by a disk centred around the spatial frequency of the illumination pattern.

Let us consider the simplest case, a structured illumination with a purely sinusoidal pattern of spatial frequency k_{SIM}. In the reciprocal space this pattern corresponds to two deltas centred at $\pm k_{SIM}$ and a third one centred in the origin, which accounts for the inevitable DC component of the illumination[1]. As exemplified in figure 3.2, the spatial frequency information that falls inside the disks centred around $\pm k_{SIM}$ will be made observable thanks to the effect of the moiré fringes. The application of this patterned illumination thus allows to extend the observable region beyond the diffraction limit in the direction of the sinusoidal pattern. In order to improve the resolution in all the directions in real space it is required to rotate the pattern by 120° and 240° to ensure the extension of the observable region in all directions. In fact, by doing so, one can gather almost the entirety of the information that lies in a disk with radius twice as large as the physically observable region, as shown on the right in figure 3.2. In other words, one has effectively doubled the resolution of the optical system.

It is important to point out that employing this method the image that is captured by the microscope is the sum of the multiple contributions, the original ones as well as the frequency shifted ones. In general, it is not possible to separate them using a single image. However, their relative contribution to the image depends on the known and controllable phase of the illumination patter, therefore by tweaking the illumination phase — namely

[1] A true sinusoidal pattern would require a negative intensity in certain portions of space which is obviously nonphysical. For this reason the pattern that can actually be employed is a sinusoid offset by its average value.

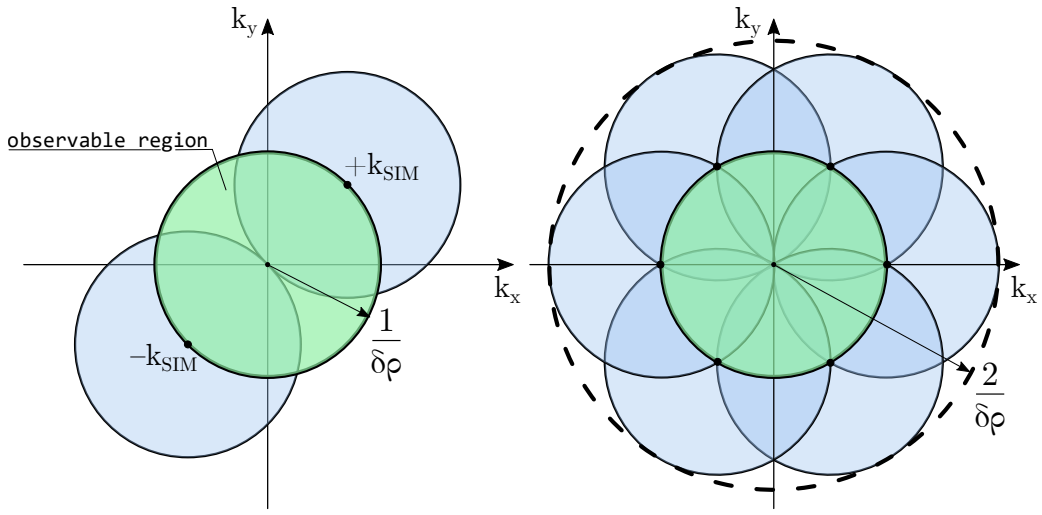

Figure 3.2: Representation in reciprocal space of a sinusoidally structured illumination. In green it is represented the observable region, while in light blue are highlighted the regions of reciprocal space that get shifted by the effect of the moiré fringes. On the left it is visible the effect of a single sinusoidal pattern whereas on the right three of such patterns are combined. The dashed line represents the extended observable region

shifting the pattern in real space — and taking multiple images it is possible to disentangle the different components and restore the original information.

This technique posses several advantages that makes it particularly attractive. Besides the obvious advantage over standard widefield fluorescence microscopy that is represented by the improved resolution, super-resolved SIM offers some advantages over alternative super-resolved microscopy techniques like PALM and STED. Although the resolution achievable with SIM cannot reach the one attainable with localization microscopy such as as PALM, it offers the advantage of not requiring samples stained with specific fluorophores. In fact, there is no need for photoactivable/photoswitchable fluorophores as SIM exploits the same ones used for widefield fluorescence. Furthermore, it requires a much shorter acquisition time in comparison with localization microscopy techniques, characteristic which is necessary to achieve high throughput. Compared to STED and others non-linear illumination techniques linear SIM achieves super resolution with a relatively low light dose on the sample, allowing for low photoxicity. Exploiting non-linear illumination SIM techniques can achieve an even higher resolution albeit at the price of severely limiting the advantages just mentioned. In fact, non-linear SIM requires higher illumination powers, increasing phototoxicity, and/or specialized fluorophores as well as a longer acquisition time hindering its throughput. [31] Furthermore, it has been proven that the use of structured illumination allows to realize optical sectioning of samples in way that is not

dissimilar to the one achieved with confocal microscopy. [32, 33] Finally, this technique is suitable for the combination with light-sheet illumination microscopy which further extends the capabilities of structure illumination microscopy as it will be detailed in section 3.2.

In the next sections are presented two practical implementations of this technique as well as an analytical description of the process of image reconstruction.

3.1.1. Two-beam interference SIM

From a practical point of view a sinusoidal pattern can be easily obtained by the interference of two laser beams propagating in different directions. In fact the intensity in this case takes up the following expression[2]:

$$I(\vec{r}) = I_1 + I_2 + 2\sqrt{I_1 I_2}\cos\left(\Delta\varphi_{12} + \left(\vec{k}_2 - \vec{k}_1\right)\cdot\vec{r}\right)$$

Where I_1, I_2 are the intensities of the two beams, $\vec{k}_1, \vec{k}_2$ their propagation direction and $\Delta\varphi_{12}$ their relative phase difference.

Defining $C(\vec{r})$ the concentration of fluorophores in the sample, the image acquired by a microscope characterised by the point spread function $PSF(\vec{r})$ is determined by the following expression:

$$D(\vec{r}) = [C(\vec{r})I(\vec{r})] * PSF(\vec{r})$$

which corresponds to the the intensity of fluorescent light coming off of the sample $C(\vec{r})I(\vec{r})$, convoluted with the PSF.

Taking the Fourier transform of this expression yields the following expression, where $\mathscr{F}\{PSF\} = OTF$ is the optical transfer function of the system and the products are swapped with convolution products and viceversa.

$$\hat{D}(\vec{k}_\perp, k_z) = \left[\hat{C}(\vec{k}_\perp, k_z) * \hat{I}(\vec{k}_\perp, k_z)\right] OTF(\vec{k}_\perp, k_z)$$

The Fourier transform of the illumination intensity is simply composed by three deltas, the first centred in the origin and the other two centred in $\pm\vec{k}_{\perp,ill} \triangleq \pm\left(\vec{k}_2 - \vec{k}_1\right)$ that is the direction of the sinusoidal pattern given by the interference of the two beams. Furthermore, the phase term present in the cosine function gives rise to two exponential

[2] This expression can be obtained following the same procedure detailed in appendix A applied on two input beams rather than three. Simply imposing the any of the three beams to have zero intensity in equation A.2 yields the two beam case described here.

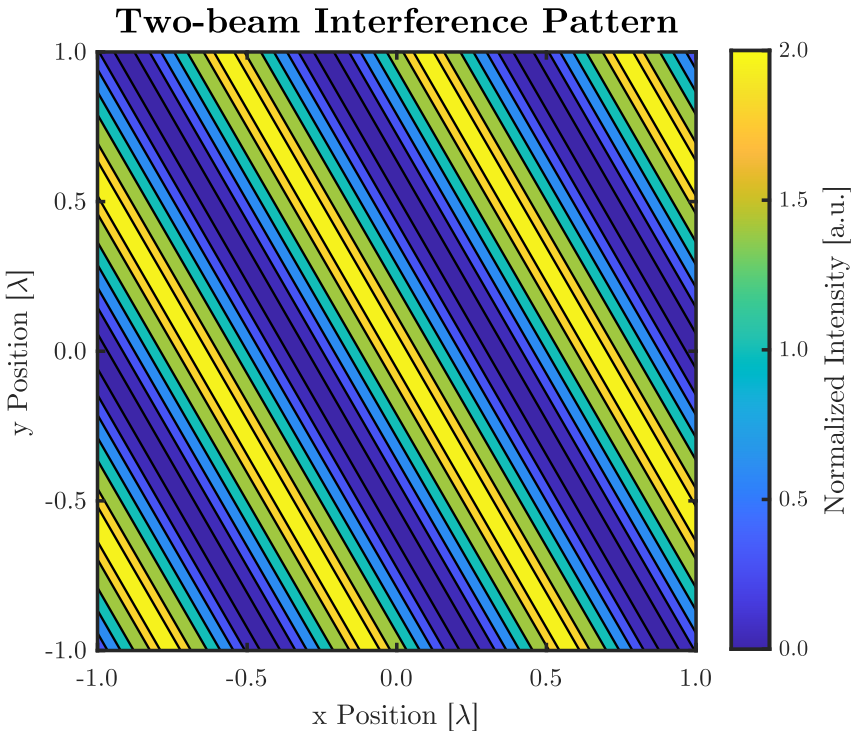

Figure 3.3: Contour plot of the interference pattern arising from two coherent beams propagating in different directions.

terms $e^{\pm i\Delta\varphi_{12}}$. Therefore imposing this expression we obtain the following:

$$\begin{aligned}\hat{D}\left(\vec{k}_\perp, k_z\right) = \alpha_1 \hat{C}\left(\vec{k}_\perp, k_z\right) OTF\left(\vec{k}_\perp, k_z\right) \\ + \alpha_2 \hat{C}\left(\vec{k}_\perp - \vec{k}_{\perp,ill}, k_z\right) OTF\left(\vec{k}_\perp - \vec{k}_{\perp,ill}, k_z\right) e^{-i\Delta\varphi_{12}} \\ + \alpha_3 \hat{C}\left(\vec{k}_\perp + \vec{k}_{\perp,ill}, k_z\right) OTF\left(\vec{k}_\perp + \vec{k}_{\perp,ill}, k_z\right) e^{+i\Delta\varphi_{12}}\end{aligned}$$

Where the α_1, α_2 and α_3 take into account the constants due to the Fourier transform.

In this expression $\hat{D}\left(\vec{k}_\perp, k_z\right)$ is known as it corresponds to the Fourier transform of the captured image. $\vec{k}_{\perp,ill}$ and $\Delta\varphi_{12}$ are also known as the illumination is controlled. Finally, the OTF is known since it depends on the characteristics of the system and is independent from both illumination and sample. Clearly, the only unknown in this equation is the concentration of fluorophores $\hat{C}(\vec{k}_\perp, k_z)$ which is precisely what we want to retrieve from the sample. This term appears three times in the equation: the first term $\hat{C}(\vec{k}_\perp, k_z)$ represents the spatial information that can be normally retrieved in the observable region, while the other two, $\hat{C}(\vec{k}_\perp \pm \vec{k}_{\perp,ill}, k_z)$, represent the information of the sample that is frequency shifted because of the moiré fringes effect. As anticipated before, these three information are simultaneously present in the image extracted and

can only be disentangled by taking multiple images. In fact, by taking three images of the sample and shifting the illumination pattern in space, that is applying three different phase differences $\Delta\varphi_{12}$ between the beams, one can write the following linear system:

$$\begin{bmatrix} \hat{D}\left(\vec{k}_\perp, k_z\right)^{(1)} \\ \hat{D}\left(\vec{k}_\perp, k_z\right)^{(2)} \\ \hat{D}\left(\vec{k}_\perp, k_z\right)^{(3)} \end{bmatrix} = M \begin{bmatrix} \hat{C}\left(\vec{k}_\perp, k_z\right) OTF\left(\vec{k}_\perp, k_z\right) \\ \hat{C}\left(\vec{k}_\perp - \vec{k}_{\perp,ill}, k_z\right) OTF\left(\vec{k}_\perp - \vec{k}_{\perp,ill}, k_z\right) \\ \hat{C}\left(\vec{k}_\perp + \vec{k}_{\perp,ill}, k_z\right) OTF\left(\vec{k}_\perp + \vec{k}_{\perp,ill}, k_z\right) \end{bmatrix}$$

with

$$M = \begin{bmatrix} \alpha_1 & \alpha_2 e^{-i\Delta\varphi_{12}^{(1)}} & \alpha_3 e^{+i\Delta\varphi_{12}^{(1)}} \\ \alpha_1 & \alpha_2 e^{-i\Delta\varphi_{12}^{(2)}} & \alpha_3 e^{+i\Delta\varphi_{12}^{(2)}} \\ \alpha_1 & \alpha_2 e^{-i\Delta\varphi_{12}^{(3)}} & \alpha_3 e^{+i\Delta\varphi_{12}^{(3)}} \end{bmatrix}$$

Taking the phase values $\Delta\varphi_{12}^{(j)}$ such that the three equations of the system are linearly independent a unique solution can be found and the information content o the image correctly retrieved. [34] Repeating the process for three different orientations of the pattern in space the lateral resolution is effectively increased in both directions of space, as described in the previous section.

3.1.2. Three-beam interference SIM

An alternative version to two-beam SIM proposed by the group of Mark Neil [31] is reported in this section. Previously it has been described how employing the interference of two coherent beams one can obtain super-resolved images. To achieve a isotropic resolution improvement the pattern has to be rotated in space so that the observable region in reciprocal space is extended in all directions. The alternative presented here exploits three mutually coherent laser beams instead of just two which lifts the requirement of rotating the pattern. In fact, by computing the interference pattern of three beams — reported in appendix A — obtains the following expression for the illumination intensity:

$$\begin{aligned} I = I_1 + I_2 + I_3 + \\ + 2\sqrt{I_1 I_2}\cos\left(\Delta\varphi_{12} + \left(\vec{k}_2 - \vec{k}_1\right)\cdot\vec{r}\right) + \\ + 2\sqrt{I_1 I_3}\cos\left(\Delta\varphi_{13} + \left(\vec{k}_3 - \vec{k}_1\right)\cdot\vec{r}\right) + \\ + 2\sqrt{I_2 I_3}\cos\left(\Delta\varphi_{23} + \left(\vec{k}_3 - \vec{k}_2\right)\cdot\vec{r}\right) \end{aligned}$$

It is evident in this expression that the overall pattern is the superposition of the inter-

ference of two beams at a time, beam 1 with 2, 1 with 3 and finally 2 with 3. The pattern is composed in fact by three sinusoidal patterns in three different directions, which is precisely the expression presented in the previous section.

In the case of three laser beams propagating at an angle of 120° one with respect to the other the overall pattern obtained is represented in figure A.2. A detailed analyses of the features of this pattern is presented in appendix A.

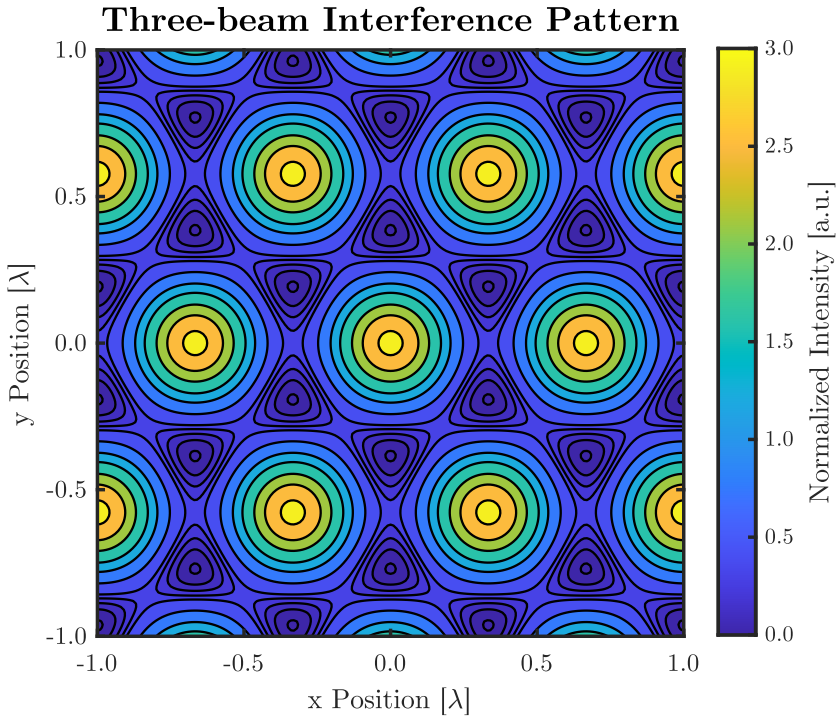

Figure 3.4: Contour-plot of the interference pattern of three beams inclined by 120° with each other.

This approach offers the same resolution improvement that can be attained employing the the two beam resolution pattern at the advantage of a slightly faster acquisition process. In fact, in the case of two beams are required 3 phase shifts × 3 pattern orientations, for a total of 9 images to be acquired. With three-beam interference no pattern rotation is required and only 7 phase shifts are sufficient for the reconstruction, as it will be detailed in the following.

Applying the same exact procedure described in the previous section one can see that the Fourier transform of the illumination pattern is composed of seven deltas centred at $0, \pm\left(\vec{k}_2 - \vec{k}_1\right), \pm\left(\vec{k}_3 - \vec{k}_1\right)$ and $\pm\left(\vec{k}_3 - \vec{k}_2\right)$. For this reason the Fourier transform of the captured image will contain 7 contributions — thus 7 unknowns — that we are required to disentangle. Following the same approach already presented we can acquire

seven images each taken with a different illumination phases $\Delta\varphi_{12}^{(j)}, \Delta\varphi_{13}^{(j)}, \Delta\varphi_{23}^{(j)}$ we can write the linear system:

$$\begin{bmatrix} \hat{D}\left(\vec{k}_\perp, k_z\right)^{(1)} \\ \hat{D}\left(\vec{k}_\perp, k_z\right)^{(2)} \\ \hat{D}\left(\vec{k}_\perp, k_z\right)^{(3)} \\ \hat{D}\left(\vec{k}_\perp, k_z\right)^{(4)} \\ \hat{D}\left(\vec{k}_\perp, k_z\right)^{(5)} \\ \hat{D}\left(\vec{k}_\perp, k_z\right)^{(6)} \\ \hat{D}\left(\vec{k}_\perp, k_z\right)^{(7)} \end{bmatrix} = M \begin{bmatrix} \hat{C}\left(\vec{k}_\perp, k_z\right) OTF\left(\vec{k}_\perp, k_z\right) \\ \hat{C}\left(\vec{k}_\perp - \vec{k}_{\perp,21}, k_z\right) OTF\left(\vec{k}_\perp - \vec{k}_{\perp,21}, k_z\right) \\ \hat{C}\left(\vec{k}_\perp + \vec{k}_{\perp,21}, k_z\right) OTF\left(\vec{k}_\perp + \vec{k}_{\perp,21}, k_z\right) \\ \hat{C}\left(\vec{k}_\perp - \vec{k}_{\perp,31}, k_z\right) OTF\left(\vec{k}_\perp - \vec{k}_{\perp,31}, k_z\right) \\ \hat{C}\left(\vec{k}_\perp + \vec{k}_{\perp,31}, k_z\right) OTF\left(\vec{k}_\perp + \vec{k}_{\perp,31}, k_z\right) \\ \hat{C}\left(\vec{k}_\perp - \vec{k}_{\perp,32}, k_z\right) OTF\left(\vec{k}_\perp - \vec{k}_{\perp,32}, k_z\right) \\ \hat{C}\left(\vec{k}_\perp + \vec{k}_{\perp,32}, k_z\right) OTF\left(\vec{k}_\perp + \vec{k}_{\perp,32}, k_z\right) \end{bmatrix}$$

with

$$M = \begin{bmatrix} \alpha_0 & \alpha_{12}e^{-i\Delta\varphi_{12}^{(1)}} & \alpha_{12}e^{+i\Delta\varphi_{12}^{(1)}} & \alpha_{13}e^{-i\Delta\varphi_{13}^{(1)}} & \alpha_{13}e^{+i\Delta\varphi_{13}^{(1)}} & \alpha_{23}e^{-i\Delta\varphi_{23}^{(1)}} & \alpha_{23}e^{+i\Delta\varphi_{23}^{(1)}} \\ & & & \vdots & & & \\ \alpha_0 & \alpha_{12}e^{-i\Delta\varphi_{12}^{(7)}} & \alpha_{12}e^{+i\Delta\varphi_{12}^{(7)}} & \alpha_{13}e^{-i\Delta\varphi_{13}^{(7)}} & \alpha_{13}e^{+i\Delta\varphi_{13}^{(7)}} & \alpha_{23}e^{-i\Delta\varphi_{23}^{(7)}} & \alpha_{23}e^{+i\Delta\varphi_{23}^{(7)}} \end{bmatrix}$$

where the factors α_j account for the constants arising from the Fourier transform and the intensity of the beams.

Here are reported, for completeness, the values of the illumination phases required to achieve the correct image reconstruction.

$$\begin{cases} \Delta\varphi_{12}^{(j)} = j\frac{2\pi}{7} \\ \Delta\varphi_{13}^{(j)} = j\frac{2\pi}{7} \\ \Delta\varphi_{23}^{(j)} = j\frac{2\pi}{7} \end{cases}, \qquad j = 0, 1, 2, \ldots, 6$$

The criterion behind the selection of such phases is that the sum of the interference pattern, appropriately shifted gives rise to a homogeneous illumination. The calculation of such phases can found in the work of Calvarese [35].

3.2. Selective Plane Illumination and Lattice Light Sheet Microscopy

Selective plane illumination microscopy (SPIM) techniques have revolutionized the field of biological imaging thanks to the various improvements they provide. The aptly-named SPIM technique consists of illuminating the sample exploiting a light-sheet, typically generated shining light on a cylindrical lens, in a direction orthogonal to the detection axis so that only the in-focus plane of the sample is illuminated. [36] The light-sheet is swept across the sample — or viceversa — so that a 3D reconstruction of its structure can be achieved. This approach offers several advantages: for one, the single plane illumination allows to achieve optical sectioning, with axial resolution better or comparable to techniques such as confocal fluorescence microscopy (CPM) and two-photon excitation microscopy (2PEF), with none of the phototoxicity of these techniques. In fact, only the section of the sample that is illuminated by the light-sheet experiences bleaching, while the rest of the sample is not affected. Furthermore, compared to CPM, SPIM offers a much faster acquisition speed as it relies on widefield illumination and detection rather than a scanning illumination. [37] Although theoretically SPIM does not provide an improved lateral resolution, in practical applications, since it is affected by negligible out of focus background light, it can achieve a better effective resolution thanks to the better contrast.

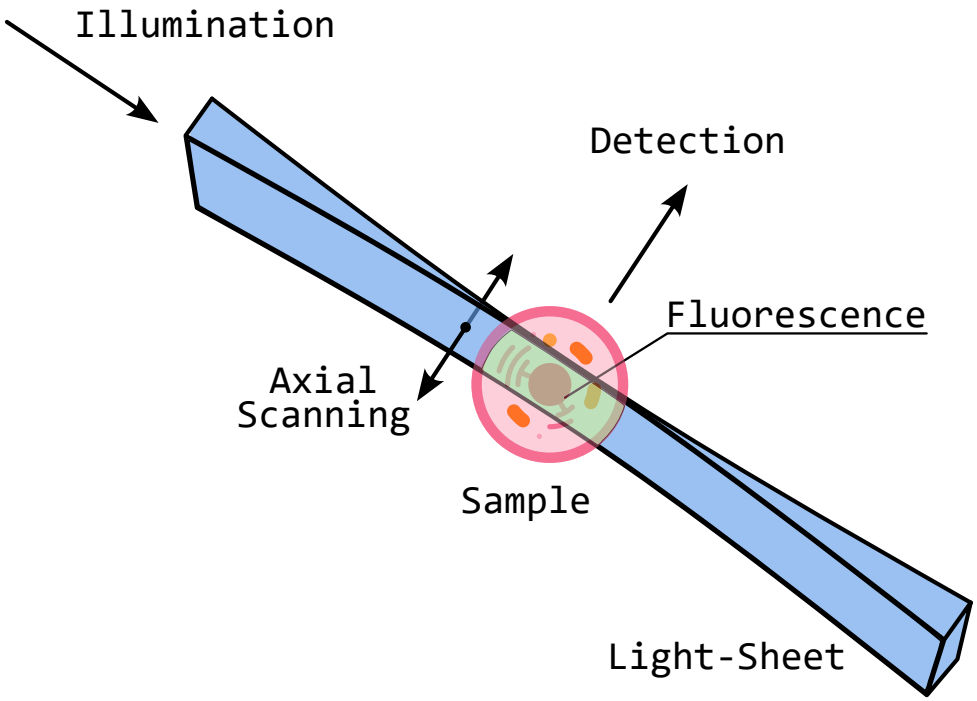

Figure 3.5: Schematic representation of selective plane illumination microscopy.

In recent year a new technique, dubbed lattice light-sheet microscopy (LLSM), has evolved by the combination of SIM and SPIM with the goal of benefiting simultaneously of the optical sectioning of light-sheet microscopy as well as the super resolution attainable with structured imaging. The first demonstration of this approach was carried out by the group of E. Betzig in 2014 [38]. In this work the sample was swept under different illumination beams — Gaussian, Bessel and most notably 2D lattice — so that a single plane of the sample was illuminated at once. They demonstrated the use of a (virtual) light sheet with a lattice modulation allows to either better confine the illumination into a tight plane so to improve on the optical sectioning offered by SPIM, or provide super-resolved imaging. A advantage of these technique consists in the split of the illumination power across multiple sources, which has been showed to be much less phototoxic compared to a single beam illumination with equal power. Further studies exploited LLSM showing how it can be used to provide, along with the aforementioned advantages, the capability of extending the field of view so to image larger samples at high speed. [39, 40]

A different take on LLSM is the one demonstrated by Stelzer et al. [41] in which mutually coherent light-sheets propagating in different directions are made to interfere in the region where the sample is located. Thus the specimen is illuminated by a sheet light featuring an interference pattern like the ones described in the previous section. Super resolution can be then attained exploiting the structured illumination of the light-sheet which simultaneously grants optical sectioning capabilities. This is the approach that will be described in section 3.4 around which this thesis project revolves. In this case, the same approach on light-sheet combined with structured illumination is realized in integrated optics rather than with bulk optics.

3.3. Microscopy on Chip

The field of microscopy in the recent years has proven a particular interest towards the realization of integrated imaging systems, defined as microscopes on chip (MOCs). The main goal of these type of devices is the realization of imagining systems that are compact, easily portable and affordable. MOCs exploit techniques of integrated optics and microfluidics to realize sophisticated optical microscopes and partially substitute more expensive and more complex external bulk optics. One important feature of MOCs is that they exploit microfluidic channels to perform continuous sample delivery, that allows to easily perform studies on large population samples and possibly in an automatic fashion.

Two different approaches to the realization of MOCs can be distinguished based on the presence or absence of integrated optical elements on the device. Off-chip MOCs exploit

microfluidic elements for the delivery and manipulation of samples which are than imaged with external bulk optics. On-chip MOCs instead, feature optical components fully integrated on the same platform guaranteeing superior compactness and portability as well as ease of use and reliability. In fact, by integrating optical systems directly on the platform hosting the microfluidic system guarantees optimal and stable alignment of the components simplifying its use. Thanks to the drastically decreased costs, high-quality imaging could be made readily accessible for developing countries lacking the large imaging infrastructures otherwise required. Furthermore, point of care diagnostics can benefit from the realization of powerful and easy to use imaging systems.

(MOCs) exploit different optical investigation techniques tailored to the specific need of the specimen to be analysed ranging from single cells (10-20 μm) to small animal embryos ($\sim$1 mm). The main categories of implemented microscopy methodologies in MOCs are transillumination and fluorescence. The first one include methods that employ light that is transmitted through the specimen that is then collected by a detector positioned on the opposite side. It includes techniques such as bright-field, phase contrast and holographic microscopy. The main advantage of these techniques is that they are label-free which allows direct analysis of the samples without requiring treatment or staining. The second category, fluorescence microscopy, employs samples that are stained with fluorescent markers that instead allow higher specificity compared to label-free techniques. Among fluorescent microscopy techniques one important imaging method is that of selective plane illumination microscopy which can particularly benefit from the integration on microfluidic platforms and can be used to realize high-throughput imaging devices with optical sectioning capabilities. [42–46]

3.4. PROCHIP project

The thesis work that is here presented has been carried out within the PROCHIP project, led by the CNR IFN and founded by the European Union. [47] The goal of this project is to realize a microscope on chip featuring a microfluidic channel for automatic sample delivery and an integrated optical circuit to illuminate the specimens. This device has to be able to realize super-resolved 3D imaging of single cells stained with fluorescent markers[3]. The technique that is employed is SIM light sheet microscopy in which three light-sheets illuminate the single cells flowing at constant rate through a microfluidic channel. The optical sectioning guaranteed by the light-sheet illumination combined with

[3] The markers utilized in this project are Alexa Fluor 488 and Alexa Fluor 561. For this reason the main wavelengths considered in this work are 488 and 561 nm.

the constant flowing rate of the cells allows, by acquiring multiple images, to perform a 3D reconstruction of the single cells. Such light-sheets, generated by shining a mutually coherent Gaussian laser beams on cylindrical lenses, are made to interfere on the channel. The interference of the three beams determines a pattern, as the one described in section 3.1.2, which serves as a structured illumination. Therefore, the techniques of structured illumination microscopy can be exploited allowing to beat the diffraction limit and improve the lateral resolution by a factor of two. As it has been detailed in the section dedicated to SIM, the interference pattern has to be shifted for the reconstruction algorithm to function, thus it is required that the optical phase of the input laser beams can be tweaked at will. To control the phase of the input beams thermal shifters are utilized, exploiting the principle of the thermo-optic effect described in section 1.3. This chip will be realized with FLM technique, specifically, optical waveguides are directly inscribed in the glass chip whilst microfluidic components are realized with the FLICE technique, both described in Chapter 2.

At the current state of the project a full on single chip integration of all the components is yet to be achieved. In fact at the state of the art, high quality photonics circuits can be realized in alumino-borosilicate glass whilst microfluidic strutures are better realized on fused-silica.

4 | Materials and methods

4.1. Device fabrication

4.1.1. Materials

All the devices presented in this work have been fabricated in Alkaline Earth Boro-Aluminosilicate glass substrates produced and sold by Corning® under the commercial name EAGLE XG®. The chips utilized have dimensions (X × Y × Z) of 25 mm × 25 mm × 1 mm or 50 mm × 25 mm × 1 mm depending on the footprint of the device to realize. The two opposing faces are pre-polished and ready for fabrication.

4.1.2. Fabrication setup

Laser Source

The laser utilized for the fabrication is a cavity-dumped diode-pumped Yb:KYW oscillator, developed in 2005 in the laboratories of the Max Planck Institute of Heidelberg (Germany) [48]. This laser features an emission wavelength of 1030 nm, ∼300 fs pulses at a repetition rate of 1 MHz. The same laser has been utilized for different processes as the waveguide inscription, with the methods described in section 5.1, the ablation of shallow trenches and the patterning of the resistors for the thermal shifters described in the section 2.6.

The focusing optics utilized is a 50× magnification objective, with 0.65 NA, working distance 5.09 - 4.35 mm and a correction collar for cover glass with thickness up to 1.2 mm (Olympus LCPLN50XIR). The collar was set for the correction of 1.2 mm of glass.

The power is set utilizing a powermeter (Coherent® LabMax-TOP) and a linear polarizer positioned before the focusing objective.

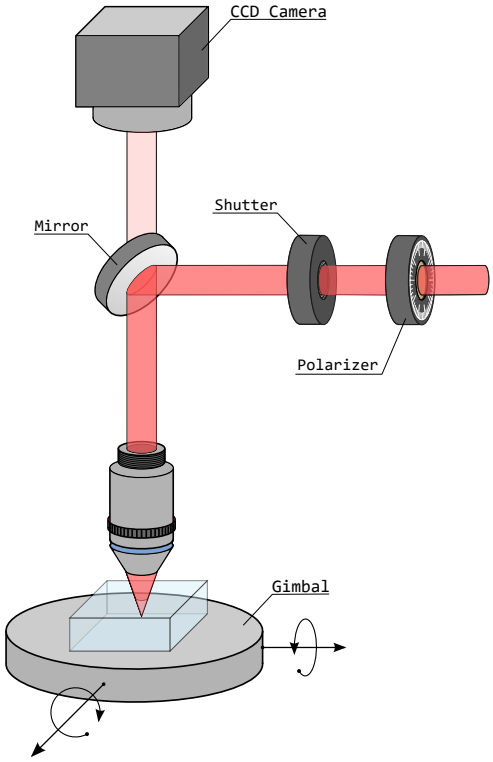

Figure 4.1: Schematic of the setup Representing from right to left, polarizer, beam shutter, focusing objective, gimbal and CCD camera.

Translation axes stage

The fabrication of the devices is realized by translating the glass chip in the three directions under the focus of the femtosecond laser with a high precision translation system (Aerotech FIBERGlide 3D). This three-axes air-bearings linear translation stage, with spatial resolution of 100 nm, is controlled by a dedicated software (Aerotech Automation 3200) which allows to drive the stages through G-code programs. The same program also delivers the trigger signals for the mechanical shutter (Thorlabs SH05/M) present in the line which allows to interrupt the laser beam.

On this stage furthermore, it is mounted a gimbal (Thorlabs GM100/M) that allows to finely control the tilt of the glass substrate to ensure the perfect orthogonality of the chip with the laser beam. To control the tilt of the chip it is observed the back-reflection of the laser beam at the air-glass interface thanks to a CCD camera mounted above the focusing optics. In fact, when the laser beam is perfectly focused on an interface the back reflected beam is registered by the CCD camera. Then, the glass chip is translated under the laser beam and its tilt is recursively tuned until the spot of back-reflected light is visible and unchanging across the whole surface of the glass chip.

4.1.3. Sample treatments

Thermal annealing

The inscription of the waveguides causes the accumulation of a lot of stress in the material. This determines the presence of a uniform ring, with a lower index contrast, around the core of the waveguides that has been showed to lower the performances of this kind of femtosecond-laser written waveguides. It has been demonstrated that a process of thermal annealing can remove the external stress ring, while preserving the high index contrast between the core and the surrounding glass, and thus improving the bending losses of the waveguides. [49]

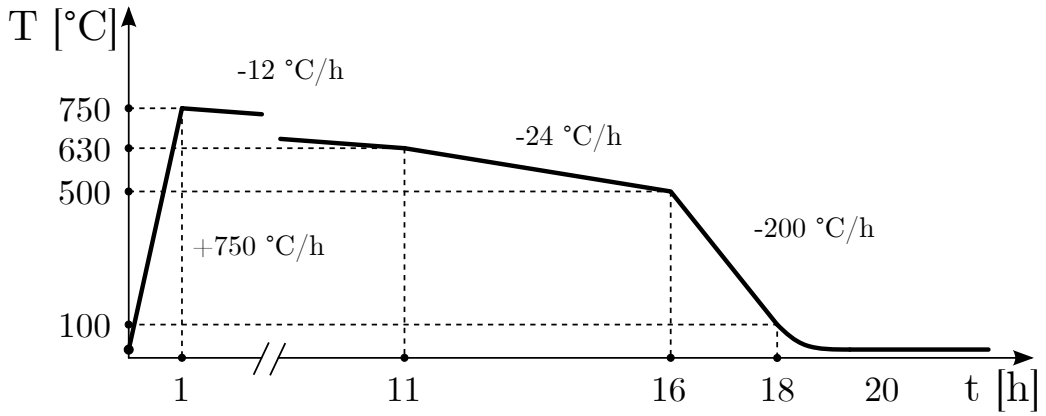

Figure 4.2: Thermal annealing treatment.

This thermal treatment consists of heating up the glass substrate above the annealing temperature, 722°C for EAGLE XG® [50], followed by a slow cooling below the strain point (669°C) which allows the removal of stress and birefringence. The treatment followed, represented in figure 4.1.3, has been optimized by the research group with an industrial oven (Nabertherm P330).

Surface polishing

After the fabrication and thermal annealing, the glass chip has to undergo a process of surface polishing with the goal of removing irregularities and scratches that are present on the input and output facets of the device. The high roughness of the surface would otherwise lead to a poor coupling, huge power losses and ultimately preventing the study of the optical components inscribed in the glass chip. An ulterior reason for the polishing process is to remove the tapered segments of the waveguides in correspondence of the two surfaces. In fact, the waveguides are written on the bottom surface of the glass chips (1

mm of thickness), therefore, when writing close to the edge of the chip, a considerable portion of the impinging laser beam is deflected by the edge, thus leading to an improper and not controlled modification of the material. For this reason the waveguides close to the edges show a tapered segment long approximately ∼500 µm. This portion of the waveguide typically presents a lighter and smaller modification and presumably a lower refractive index contrast which spoils the properties of the remainder of the waveguide. In fact, if not removed it leads to significantly higher losses. Therefore, in the polishing process the two facets are abraded enough to remove the tapered segment in its entirety. Or, alternatively, a slice of glass is cut from the two facets with a diamond-wire glass cutter (Well 3241) prior to the polishing procedure.

4.2. Characterization setup

The setup that has been used is schematized in figure 4.3. A single mode fiber is coupled on one extreme to a laser source while, at the other end, the fiber has been exposed peeling the protective sheath and then cut with a fiber cutter (Fujikura - Optical Fiber Cleaver CT06) which ensures a clean and planar cut of the fiber. This exposed end of the fiber as well as the device are mounted respectively on a three axes (Thorlabs NanoMax 300 - MAX313D/M) and a four axes (Thorlabs MBT402D/M) micromanipulators ensuring a precise positioning and alignment required to butt-couple the fiber to device in order to inject power into it in a controlled fashion. The butt-coupling is assisted with a stereo-microscope (Leica MZ125), working in reflectance geometry, offering a top view of the system. This allows to position the fiber-tip in contact with the glass chip without introducing tension which could both damage the fiber-tip and incline it with respect to the facet of the device, providing a sub-optimal coupling. The light at the output of the device is collected by a microscope objective (with magnifications ×10, ×20, ×40), also mounted on a three axes micromanipulator (Thorlabs NanoMax 300 - MAX313D/M), which delivers light either on a powermeter (Ophir Photonics Group Nova II) or a CCD camera (Thorlabs DCU224M). Furthermore, for the characterization of the directional couplers, a mechanical iris is inserted after the objective to selectively block the output of one of the two ports.

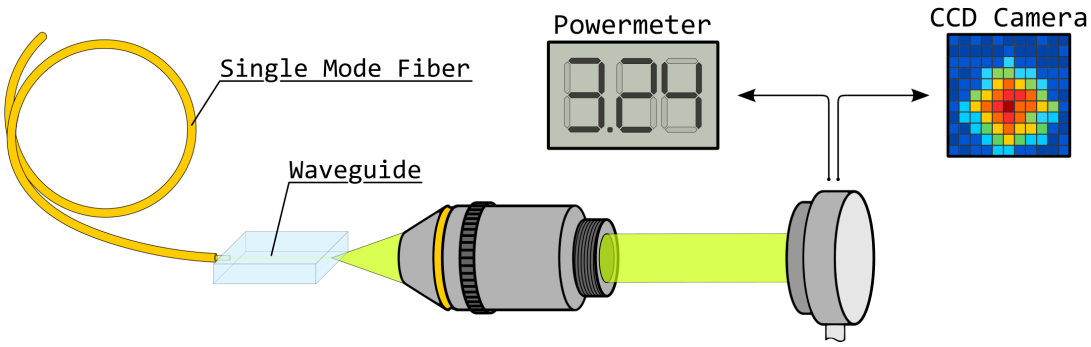

Figure 4.3: Schematic of the characterization setup.

4.2.1. Laser Sources

Here are reported the laser sources that has been used in the characterization setup.

	Wavelength	Laser Source	Delivery Fiber
	488 nm	COHERENT® OBIS 488LS	Thorlabs P3-488PM-FC-2 + P3-460B-FC-2
	532 nm	Uniphase μgreen 4301-010	Thorlabs P5-460B-PCAPC-1 + P3-460B-FC-2
	561 nm	COHERENT® OBIS 561LS	Thorlabs P3-488PM-FC-2 + P3-460B-FC-2
	607 nm	CNI laser MRL-FN-607	Thorlabs P1-460B-FC-2
	635 nm	Thorlabs TLS001-635	Thorlabs P1-460B-FC-2

4.3. Characterization methods

4.3.1. Waveguides characterization

The characterization of the waveguides entails several aspects which are related to how much power is lost in the coupling and collection of power to and from the waveguide. Such characterization is performed exploiting the setup detailed in the section 4.2.

One first thing that has to be assessed whether the waveguide is single mode, thus only sustaining the fundamental Gaussian mode, or multi-mode, hence sustaining at least one mode of higher order as well as the fundamental. This characterization is carried out by analyzing the shape of the spot on the CCD camera and investigating the presence of multiple lobes. As described in the following, the intensity profile is fit against a Gaussian profile which allows to gauge the presence of additional modes superposed to the fundamental.

Secondly, the Insertion Losses (IL) of the waveguide are measured, which describe how much power is lost[1] from the source to the powermeter because of the presence of the waveguide itself.

$$\text{IL [dB]} = -10 \log_{10}\left(\frac{P_{out}}{P_{in}}\right) \tag{4.1}$$

Where P_{out} is the power reaching the powermeter after the propagation inside the waveguide and P_{in} is the power measured at the exit of the single mode fiber that is used to couple power in it.

To measure the former, the setup used is precisely what has been detailed in the Characterization setup section, while, the latter, is measured by removing the device and positioning the tip of the fiber in the focal plane of the collection objective. Notice that this procedure rejects spurious losses inevitably present in the setup e.g., transmission losses of the objective and reflections at the interfaces.

Several factors contribute to the insertion losses and will be detailed in the following.

- Coupling Losses: These represent the losses that are encountered when light is coupled from the input fiber to the waveguide because of an imperfect spatial overlap of the two modes. In fact, if the waveguide is multimodal or has a mode profile that is asymmetric or has different dimensions compared to the input fiber, power will be lost in the coupling. These losses are described by the following expression:

$$\text{CL [dB]} = -10 \log_{10}\left(\frac{|\iint E_{SMF}\, E_{WG}\, dxdy|^2}{|\iint E_{SMF}\, dxdy|^2\, |\iint E_{WG}\, dxdy|^2}\right) \tag{4.2}$$

  Where the argument of the logarithm is the normalized overlap integral of the two modes, E_{SMF} of the input single mode fiber and E_{WG} of the waveguide. To measure these losses the CCD is used to acquire the intensity profile of both modes which are than used to compute the overlap integral through a software.

- Fresnel Losses: These losses are caused by the reflections at the interfaces of the device due to the air-glass refractive index mismatch. Exploiting the Fresnel equation, under the assumption of orthogonal incidence of the light, to compute the reflectance we obtain the following:

$$\text{FL [dB]} = -10 \log_{10}\left[1 - \left(\frac{n_{glass} - n_{air}}{n_{glass} + n_{air}}\right)^2\right] \tag{4.3}$$

[1] It is worth pointing out that with this coefficient, just like all the following, the losses are reported as a positive quantity in dB, which is the reason for the minus sign at the beginning of the expression. Since no power is generated inside the waveguides the result of the logarithm is always negative.

This expression amounts to the losses for each interface. In the characterization of the waveguides we will consider these losses to be only present at the output interface. In fact when we butt-couple the input fiber with the device, a Fabry-Pérot (FP) interferometer is formed as both the interfaces, fiber-air and glass-air, act as mirrors of reflectance ∼4%[2]. Fabry-Pérot cavities always have peaks of transmission equal to 1, which means that, under the assumption of realizing the best possible butt-coupling, we should fall in a maximum of transmission of the FP, hence we can drop the Fresnel losses at the input interface.

- Propagation Losses: As light propagates inside the waveguide it experiences absorption and scattering because of the presence of impurities or defects. [1] These phenomena account for a loss of power that is dependent on the distance travelled inside the waveguide and customarily expressed in dB/cm. Considering a straight waveguide of length L, once we subtract coupling and Fresnel losses we obtain the losses due to the propagation as a function of the distance travelled as such:

$$\text{PL [dB/cm]} = \frac{\text{IL} - \text{CL} - \text{FL}}{L} \tag{4.4}$$

- Bending Losses: In a curved waveguide there is distortion of the mode profile which leads to a portion of power to be transmitted to external radiative modes, the smaller the curvature radius the bigger the loss of power. It has in fact been shown that the losses increase exponentially with increasing curvature [51]. Furthermore, the entity of this losses is also dependent on the refractive index contrast between the waveguide and the substrate. To characterize these losses the insertion losses of different waveguides must be confronted: one straight waveguide and one waveguide containing a curved segment of length L_{curved} with curvature radius R. The two waveguides ought to be identical under any other aspect so that the coupling losses and propagation losses can be assumed to be equal.[3] Since the Fresnel losses are also identical the eventual difference between the two insertion losses is ascribable to the Bending Losses, which are expressed as a function of the length of the curved segment:

$$\text{BL [dB/cm]} = \frac{\text{IL}_{curved} - \text{IL}_{straight}}{L_{curved}} \tag{4.5}$$

[2] Calculated with the Fresnel equation for the reflectance of light incident on an interface between air $n_{air} = 1$ and glass $n_{glass} \simeq 1.5$.

[3] Ideally the two waveguides should have identical length, if not the case the measured insertion losses must be re-scaled such that the same amount of power loss is considered due to the propagation inside the waveguide.

4.3.2. Coupler characterization

The characterization of a directional coupler is fairly straightforward: light is injected in one of the two inputs and the output power of the two ports is measured. The butt-coupling is not as crucial as it is in the characterization of waveguides, the only important aspect to consider is to make sure the totality of the input power is coupled in a single port otherwise the response of the devices would be different from what expected.[4] Then, the power of the two output ports is normalized to the total amount of power exiting the device as such:

$$P_{BAR}\,[\%] = \frac{P_{BAR}}{P_{BAR} + P_{CROSS}}\,, \qquad P_{CROSS}\,[\%] = \frac{P_{CROSS}}{P_{BAR} + P_{CROSS}}$$

Where we recall the notation presented in the section 1.2.1, P_{BAR} is the power measured measured at the exit of the same waveguide in which light is coupled while P_{CROSS} is the power transferred to the adjacent waveguide.

This way large sets of couplers can be studied to infer the dependence the geometry of the coupler as well as the fabrication parameters have on the splitting of power at the two output ports.

[4] In theory one could also inject power both ports and study their behaviour with the theory presented in the section 1.2.1 only changing the initial conditions appropriately. The caveat is that the ratio of input power must be known, which is, in general, not trivial.

5 | Waveguides and coupler optimization

The goal of this project is to manufacture a photonic device which takes laser light from one input and splits its power equally in three different output waveguides. Going forward I will refer to such a device as *tritter*. Several different methods can be employed for the realization of this device, both active, such as with re-configurable Mach-Zehnder interferometers, and passive, such as with directional couplers and Y-junctions [52]. In this work it was decided to realize this guiding structure exploiting the well-known capabilities of directional couplers. As one can see in the figure 5.1 we aim at achieving the desired splitting ratio by cascading two couplers which ought to be tuned to have a splitting ratio of 33%-66% and 50%-50% respectively.

In the figure are also schematized two other important elements; the two thermal shifters. The devices are required to impart a phase shift to the light travelling in the different waveguides which is necessary for the super-resolution microscopy for which this device is designed. The present work will not deal with the realization of the thermal shifters and their configuration which has been already dealt with in precedent projects.

Finally, in the *fan-out region*, the output waveguides are positioned to allow the butt-coupling with commercial standard fibre arrays.

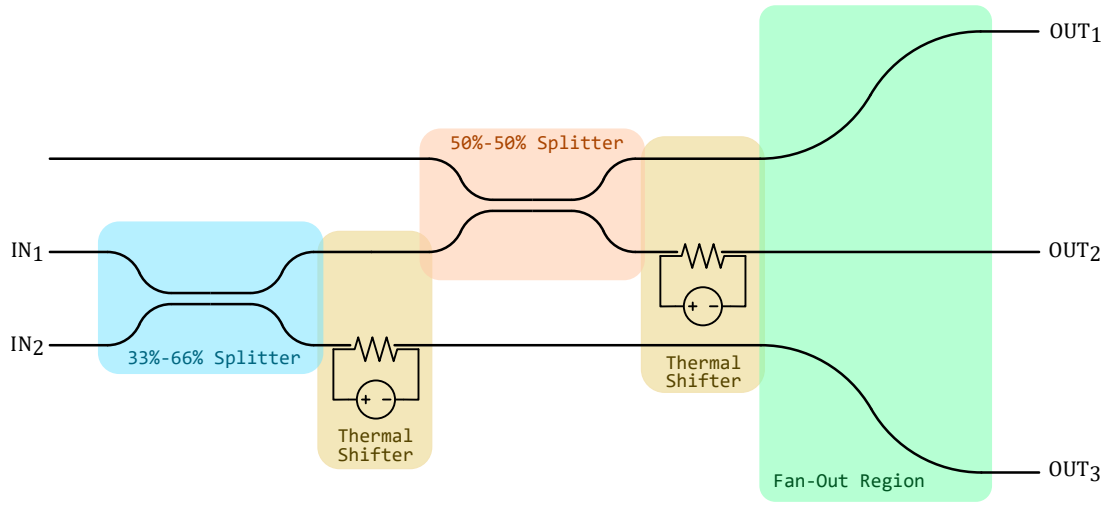

Figure 5.1: Schematic representation of a tritter. Not to scale

This chapter first analyses FLM-inscribed optical waveguides as they constitute the basic elements required to realize an integrated optical system. After the identification of a set of parameters that allow us to reliably fabricate high-quality waveguides, we will deal with the realization of directional couplers and extrapolation of their characteristics. Here is shown how directional couplers can be controlled to realize the desired splitters by tuning the fabrication parameters.

The following chapter will describe the work carried out in the realization of a tritter working simultaneously at the two wavelengths of interest of 488 and 561 nm. Successively, more wavelengths are considered in the effort to realize multi-colour devices, that is tritters working at multiple wavelengths or in an extended bandwidth.

5.1. Optical waveguides optimization

In this section are presented the results of the study of optical waveguides realized in alumino-borosilicate glass with the methods described in 4.3.1. All the waveguides described in this work have been inscribed at a depth of 15 µm inside the glass, measured from the bottom surface. The waveguides are fabricated close to the surface since it allows for a fast dynamic of the thermal shifters that will be successively realized. [26] A first preliminary study has been carried out to identify a good set of fabrication parameters for the realization of the waveguides. The goal was to realize single-mode waveguides with propagation and coupling losses as low as possible for the two working wavelengths 488 nm and 561 nm. Furthermore, for such waveguides, the dependence of the bending losses with the radius of curvature has been analysed.

The first study carried out was a large scan of multiple parameters in a window centred around values that had already shown promising results in previous studies. A total of 60 waveguides have been fabricated varying 3 parameters:

- Writing velocity: 30, 40, 50 mm/s;
- Irradiation power: 190, 210, 230, 250, 270 mW;
- Number of scans:[1] 8, 12 scans.

The 30 combinations of the parameters have then been repeated twice.

Initially, the waveguides have been characterised at wavelengths 488 and 561 nm. The results of the propagation losses measured at 561 nm are presented in figure 5.2, the losses measured at 488 nm reported an analogous behaviour. Regarding the irradiation power, waveguides written with 190 mW were weakly guiding while the best results were visible with the powers 230 mW and 250 mW, proving the existence of a good working window for low-loss waveguides at both the investigated wavelengths 488 and 561 nm.

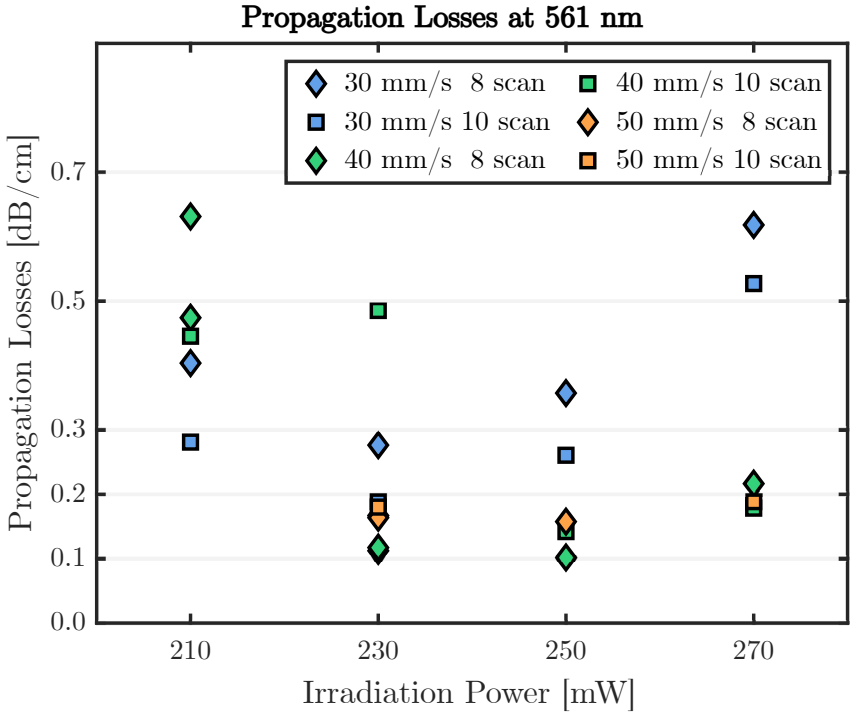

Figure 5.2: Propagation Losses of FLM-inscribed waveguides measured at 561 nm. The three writing velocities are highlighted with different colours, while the diamond and square-shaped markers indicate the number of scans.

[1] All the waveguides that will be described in this work are multiscan, meaning that the same line is irradiated in the same direction repeatedly, for a given number of scans.

This study confirmed the good choice of the set (230 mW, 40 mm/s, 8 scans) which is the set that has been used in prior works. Furthermore, the writing velocity of 50 mm/s also showed to lead to good waveguides. The number of scans didn't seem to have an impact on the results thus it was chosen to consider the lower repetition waveguides which allow for faster fabrications.

The following study analysed thoroughly a smaller set of parameters and investigated the characteristics of the waveguides at multiple wavelengths. In fact, a total of 15 straight waveguides have been fabricated with the following parameters:

- Writing velocity: 30, 40, 50 mm/s;
- Irradiation power: 230 mW;
- Number of scans: 8
- Depth: 15 μm from the closest surface.

Thus each set of fabrication parameters has been repeated and measured 5 times to obtain a statistically significant estimation of the losses.

Each and every waveguide measured supports a single mode at the wavelengths considered 488, 532, 561 and 635 nm and thus are perfect for the scope of this work. Furthermore, all waveguides are characterized by low losses comparable with state-of-the-art FLM waveguides [53]. Figure 5.3 reports the average value of the propagation losses, as well as the error bars of plus minus one standard deviation, of the waveguides fabricated with different parameters at various wavelengths.

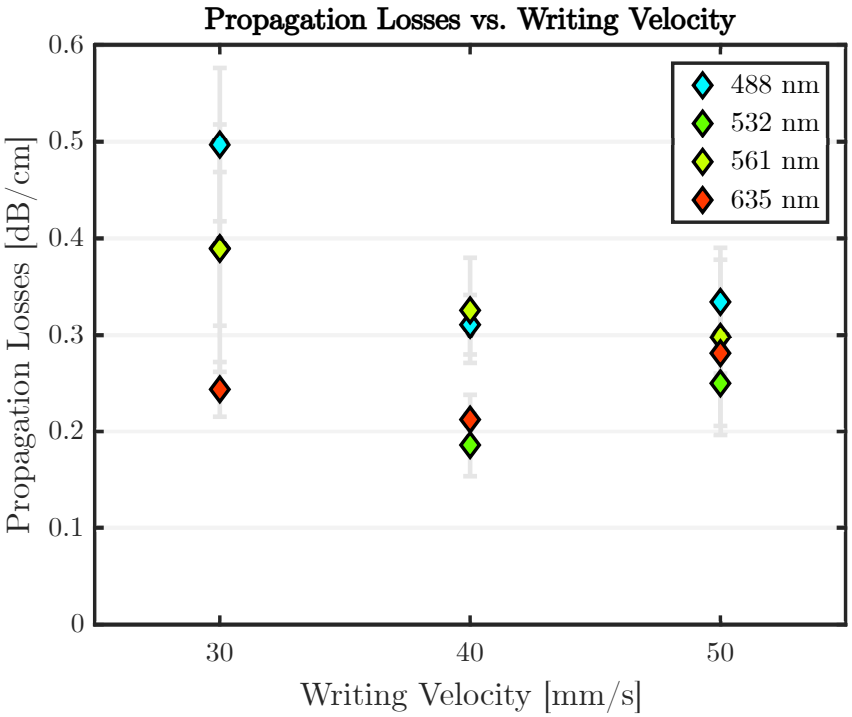

Figure 5.3: Propagation Losses of FLM-inscribed waveguides at different translation velocities and wavelengths.

No particular trend is evident in the measured data but it indicates the presence of a good working window both in terms of writing velocity and guided wavelengths which covers a considerable portion of the visible spectrum. Regarding the wavelengths 488 and 561 nm, the writing velocities of 40 and 50 mm/s show similar performances, both better than the waveguides fabricated at 30 mm/s. The wavelengths 532 nm and 635 nm both show the best performances at the writing velocity of 40 mm/s.

Figure 5.4 reports the modes measured at the CCD camera for a single waveguide written at 40 mm/s at the four wavelengths analysed. The average dimensions of the modes are reported as well.

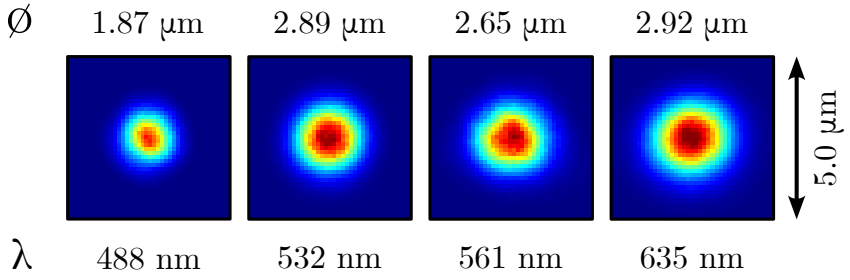

Figure 5.4: Waveguide modes measured with a CCD camera.

Admittedly some of the waveguides characterized in the first study reported propagation losses that are lower than the ones that were extracted from the second study. This performance difference could be determined by variability either in the fabrication procedure or in the measurement process or both. Many factors can, in fact, influence the characteristics of the fabricated waveguides, to cite a few, a small change in the writing depth or the duration of the laser pulses may affect the modifications induced in the substrate. Nonetheless, the latter results are considered more reliable due to the greater number of repetitions.

To study the bending losses it was prepared a set of waveguides characterised by curved portions with curvature radii of 20, 30 and 40 mm. The choice of this working range was also dictated by the existence of precedent studies which investigated a larger range of radii. The other fabrication parameters have been fixed to P = 230 mW, v = 40 mm/s and 8 scans. The writing depth has also been kept fixed at 15 μm. In figure 5.5 are reported the bending losses retrieved at the four wavelengths 488, 532, 561, and 635 nm. The logarithmic scale of the plot highlights the exponential decay of the bending losses as a function of the curvature radius, which is accurately confirmed by the performances of the waveguides at all the wavelengths except for a small variation in the 488 nm case.

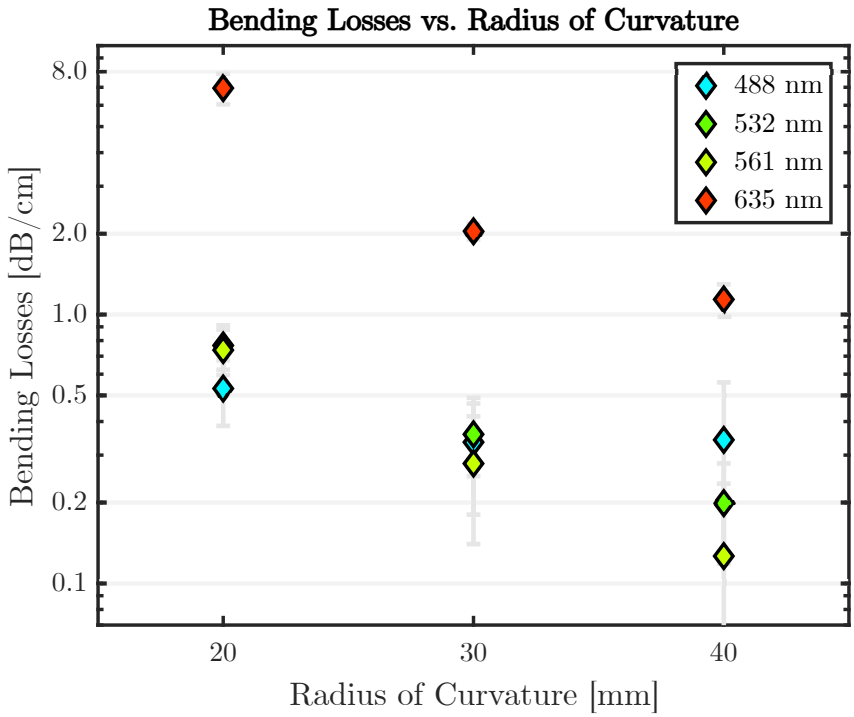

Figure 5.5: Bending Losses of FLM-inscribed waveguides with curvatures of different radii measured at multiple wavelengths. (logarithmic scale on y-axis)

As visible in figure 5.5, the wavelength 635 nm reports high values of bending losses which is reasonable considering that this kind of losses have a strong dependence on the wavelength. [1] Nonetheless, even at 30 mm of curvature considering the case of a coupler with external distance 30 μm and interaction distance 3 μm the curved portion amounts to $\sim$ 2.5 mm thus the coupler would have $\sim$90% transmittance at 635 nm and $\sim$97% at the other three wavelengths. It was chosen to work at the radius of 30 mm since the losses are still contained while allowing for more compact devices with respect to bigger radii of curvature.

In table 5.1 are reported the fabrication parameters that have been chosen for the realization of the directional couplers based on the results obtained and shown in this section. It is worth specifying that the approach that will be followed for the realization of the couplers, for what concerns the number of scans required to fabricate the waveguides, is to alternate the writing of the two arms of the coupler. The aim of this approach is to minimize the possible disturbance caused by the process of inscribing a waveguide at a close distance from another one. By alternating the writing procedure it is expected that any form of fabrication cross-talk averages out limiting its possible impact. More considerations on this matter will be presented in section 6.2.1. All the synchronous directional couplers studied were fabricated with these parameters, while the asynchronous couplers reported in section 6.2.1 will deal with some variations on some of the parameters as will be detailed in the dedicated paragraph.

Writing Velocity	**Irradiation Power**	**Number of Scans**[2]	**Radius of Curvature**	**Writing depth**
40 mm/s	230 mW	8	30 mm	15 μm

Table 5.1: Summary of the parameters selected for the fabrication of the directional couplers.

Finally, here in table 5.2 are reported the results regarding the performances of the waveguides realized with this set of fabrication parameters. The indicated values are obtained by averaging all the measurements performed. Furthermore, it is reported the value of the standard deviation describing the dispersion of the data points.

[2] Single propagation direction.

Wavelength	Propagation Losses [dB/cm]	Bending Losses [dB/cm]	Coupling Losses [dB]
488 nm	0.311 ±0.031	0.335 ±0.155	0.132 ±0.040
532 nm	0.186 ±0.032	0.359 ±0.108	0.038 ±0.011
561 nm	0.325 ±0.054	0.279 ±0.139	0.038 ±0.009
635 nm	0.212 ±0.026	2.039 ±0.136	0.128 ±0.011

Table 5.2: Results of the losses characterising the waveguides realized with the chosen set of fabrication parameters.

5.2. Directional coupler optimization

This section presents the study that has been performed to experimentally verify the directional couplers behaviour, as foreseen by theoretical considerations, as well as the analysis performed for the extraction of the parameters that describe these devices. In particular, in section 1.2 has been detailed the behaviour of directional couplers, which resulted in a set of equations describing the distribution of output power of the two waveguides. Here is reported for convenience the final result of coupled mode theory (CMT) applied to synchronous directional couplers, showing the oscillating behaviour of the transmitted power at the two output ports as a function of the coupling length (1.18).

$$\begin{cases} P_{BAR} &= \cos^2(kL + \varphi_0) \\ P_{CROSS} &= \sin^2(kL + \varphi_0) \end{cases}$$

In these equations are evidenced two important parameters that describe the behaviour of directional couplers: i) the coupling coefficient k, which represents the efficiency of coupling of the modes of the two adjacent waveguides and controls the frequency of the power exchange between the two as light propagates; ii) the initial phase φ_0 which is an additional contribution linked to the power coupling taking place in the bent region of the coupler. To be able to realize a desired splitting ratio these parameters must be known and controllable.

The simplest approach that can be followed to verify experimentally that the realized devices behave as expected by CMT, is to fabricate large batches of couplers keeping fixed every parameter but the interaction length L. In fact, realizing a coupler with increasing interaction length allows sampling of the power present in each waveguide as

light propagates through the device. Since no other fabrication parameter is changed, it is expected that both k and φ_0 remain constant as they only depend on the geometrical dimensions of the devices in the direction transversal to the propagation of light. In other words, the interaction length has no impact on these parameters which only depend on the distance of the waveguides. Thus, by taking a sufficiently large number of data points the sinusoidal behaviour of the output power predicted by the theory can be put to the test. Furthermore, these data points can be numerically fitted with a function like the one reported above, leaving the k and φ_0 as free parameters. Once extracted, these parameters give us control over the splitting ratio by tuning L.

The second approach that is presented here deals with the study of the dependence of the coupling coefficient and the initial phase with the distance of the waveguides. Recalling the expression describing the coupling coefficient (1.8), one can see that k depends on the overlap of the tail of one mode with the other thus, clearly, by changing the distance of the waveguides one can impact the coupling coefficient. As described by Alexander Szameit et al. [54] k appears to have an exponential dependence on the distance d of the waveguides of the sort:

$$k = a\, e^{-b \cdot d}$$

Such exponential dependence stems from the Gaussian profile of the modes, whose tails decrease exponentially away from the centre of the waveguide. Regarding the additional phase, φ_0 directly depends on the coupling coefficient thus it is expected to follow an analogous dependence.

To test these exponential dependencies and extract the coefficients a and b the best approach is to fabricate a batch of couplers keeping all the parameters, but the interaction distance d, fixed. This approach is less straightforward than the previous one, but it consists of sampling the power at the output of a coupler with fixed interaction length L where the coupling coefficient is varying exponentially. The resulting figure is a sinusoidal function with a frequency that changes exponentially, thus, going in the direction of decreasing d, the oscillations get faster and faster. To fit the data extracted from this kind of fabrication a specific code was developed which could simulate the behaviour of a generic directional coupler. This code takes into account the exponential dependence of the coupling coefficient with the distance of the waveguides and allows to estimate it. The theoretical and numerical considerations, as well as the code that has been developed for this purpose, are reported in detail in appendix B.

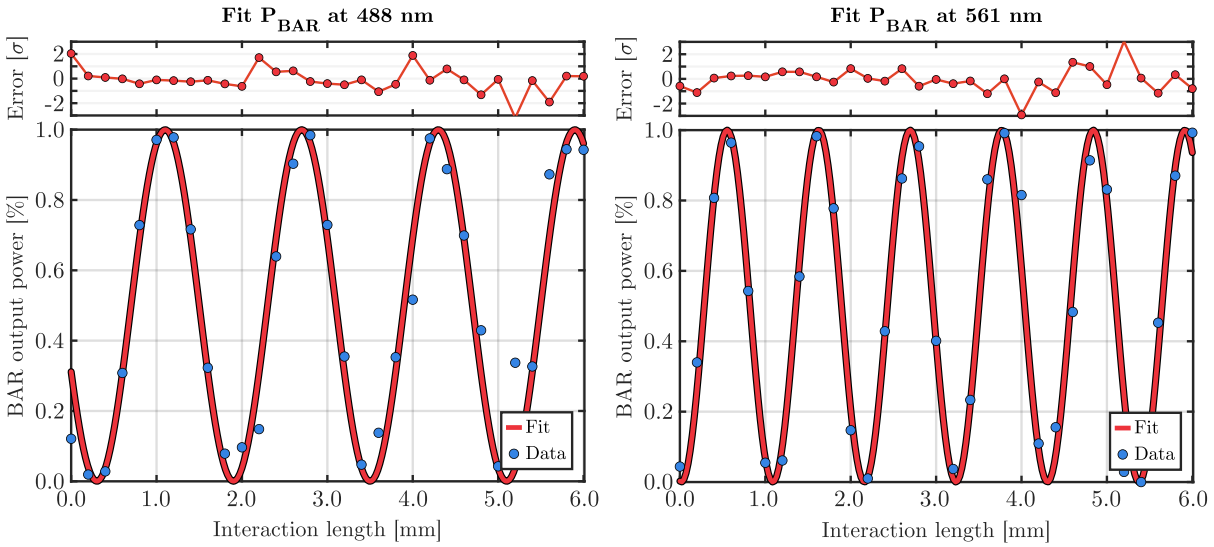

Figure 5.6: Bar output power measured at 488 nm (left) and 561 nm (right) of a set of couplers with $d = 3.5\,\mu m$ and L from 0 to 6.0 mm with step 0.200 mm.

5.2.1. Study on interaction length dependence

The results that are here reported regard the first approach mentioned in the previous section. Multiple sets of couplers were realized at different interaction distances and varying the interaction length. Figures 5.6 and 5.7 present four plots reporting the experimental data points, as well as the best fit realised, taken at the two wavelengths 488 and 561 nm. The selected interaction distances are 3.5, 4.0, 5.0† µm while the 31 values of interaction lengths were sampled at variable steps in a range starting from 0 up 6.0, 9.6, 12.0† mm, respectively.

In the figures, it is evident that the power at the output of the coupler follows a sinusoidal behaviour as expected from coupled mode theory. Furthermore, the intervals tested allow us to confidently state that the coupler experimental data points remain in line with the model even after multiple oscillations of the power between the waveguides, that is at long propagation length. Even though these results suggest that the quality of the fabrication deteriorates at longer propagation length as the data points follow less accurately the fit. This can be noticed by looking at the distribution of the errors above the plots which hints towards a correlation of the error magnitude with the interaction length. This fact is not entirely unexpected since the lateral dimensions of the waveguides are comparable with their distance in the interaction region, thus it is possible that the presence of one waveguide causes a disturbance to the other that might be negligible at short interaction

† Not shown

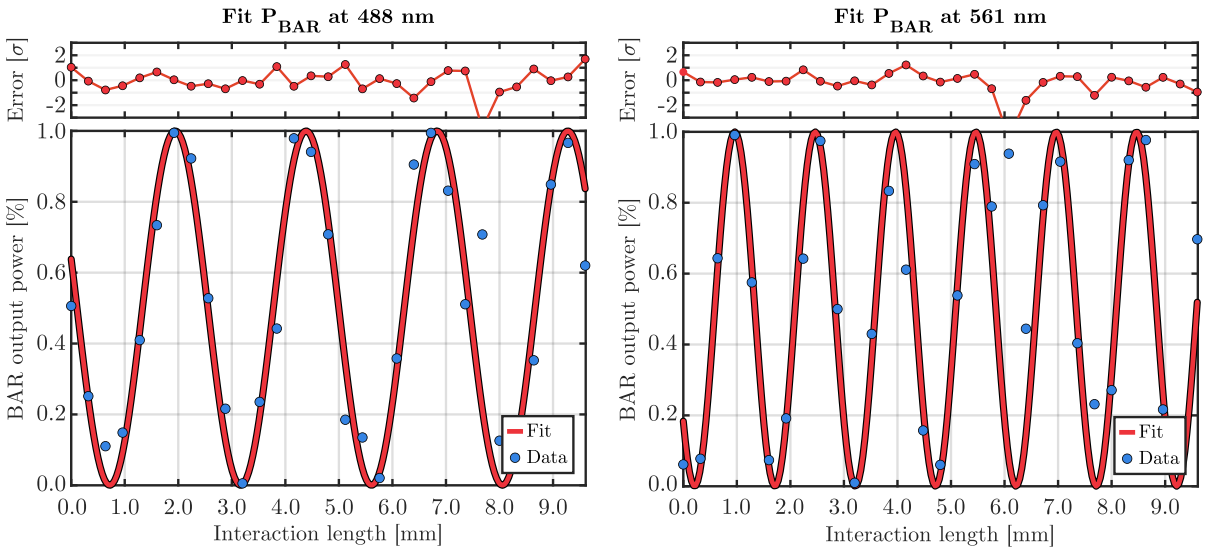

Figure 5.7: Bar output power measured at 488 nm (left) and 561 nm (right) of a set of couplers with $d = 4.0\,\mu m$ and L from 0 to 9.6 mm with step 0.320 mm.

lengths but becomes more impacting as the length increases. Nonetheless, the error remains contained even at the longest interaction length tested of 12 mm proving the existence of an ample working range. Calculating the Pearson correlation coefficient to estimate the correlation between the normalized fitting errors, taken in absolute value, and the interaction length suggested the existence of a weak correlation. In fact, the correlation coefficients obtained by each of the 9 fit analysed remained confined in the interval $0.175 < r < 0.42$ and averaged on the value $r = 0.295$. This result tells us that most likely there is no direct correlation between the magnitude of the errors and the interaction length. We can thus expect to be able to accurately obtain couplers even at long interaction lengths.

Realizing multiple sets of couplers with different interaction distances one could theoretically also estimate the exponential dependence of the coupling coefficient by fitting the "data points" corresponding to the values of the coupling coefficients extracted from each set of couplers. However, this approach is riddled with an issue regarding the propagation of errors stemming from the noisiness of the experimental data points and the trustworthiness of the fitting procedure. In fact, all the measurements of the couplers realized are affected by noise related to the measurement procedure itself along with the intrinsic variability of the fabrications. This noise will impact the fidelity of the sinusoidal fit of such points leading to an estimation of the coupling coefficient that is inevitably not perfectly accurate. Utilizing the values extracted with such a procedure to realize the additional exponential fit could lead to unreliable results. Secondly, to realize a robust

and well-grounded fit of the exponential dependence of k one would like to have many data points. Unfortunately, to obtain each of these points it is required to measure a sizable number of couplers to correctly fit the sinusoid, thus leading to a particularly cumbersome measurement. For these reasons the approach followed is the one detailed in the next section.

5.2.2. Study on interaction distance dependence

Here are reported the results obtained in the study of the dependence of the coupling coefficient with the interaction distance of the waveguides. Multiple sets of couplers were fabricated varying d while keeping fixed all the other parameters. The values of the splitting ratio of the various couplers measured were then fitted with the code simulating the behaviour of a coupler reported in appendix B, as already mentioned. This code imposes a dependence of the type of a decreasing exponential as expected from theoretical considerations and returns the two parameters a and b that described the exponential dependence extracted from the measured data points. Thus, through this fitting procedure, the dependence of the coupling coefficient with the distance of the waveguides is extracted, rendering, in effect, the interaction distance to be a parameter that can be controlled, just like the interaction length, to tune the splitting ratio of the coupler. Furthermore, also the dependence of the initial phase φ_0 with d can be extracted simultaneously.

In figure 5.8 is reported the power measured at the output of a set of 16 couplers fabricated with interaction distance variable between 3.0 µm and 6.0 µm with constant step and interaction length fixed to 0 mm. Furthermore, it is also reported the best fit of the data points realised with the procedure just mentioned.

This kind of approach allows for an accurate estimation of the dependence of k with the interaction distance since each one of the couplers measured corresponds to a data point utilized for the fitting procedure, leading to robust and high-fidelity results.

Length dependence on the coupling coefficient

Confronting the data resulting from this kind of fitting procedure and the one detailed in the previous section some discrepancies emerged. In fact, it appeared that the coupling coefficient calculated from the equation $k = a\ \exp(-b \cdot d)$ staring from the parameters obtained by the fits, systematically overestimated the value of k retrieved by fitting the sinusoidal response of the coupler. This behaviour has been observed at all the wavelengths analysed. To understand the nature of this issue multiple sets of couplers with variable interaction distance have been realized, like the one just presented, where the interaction

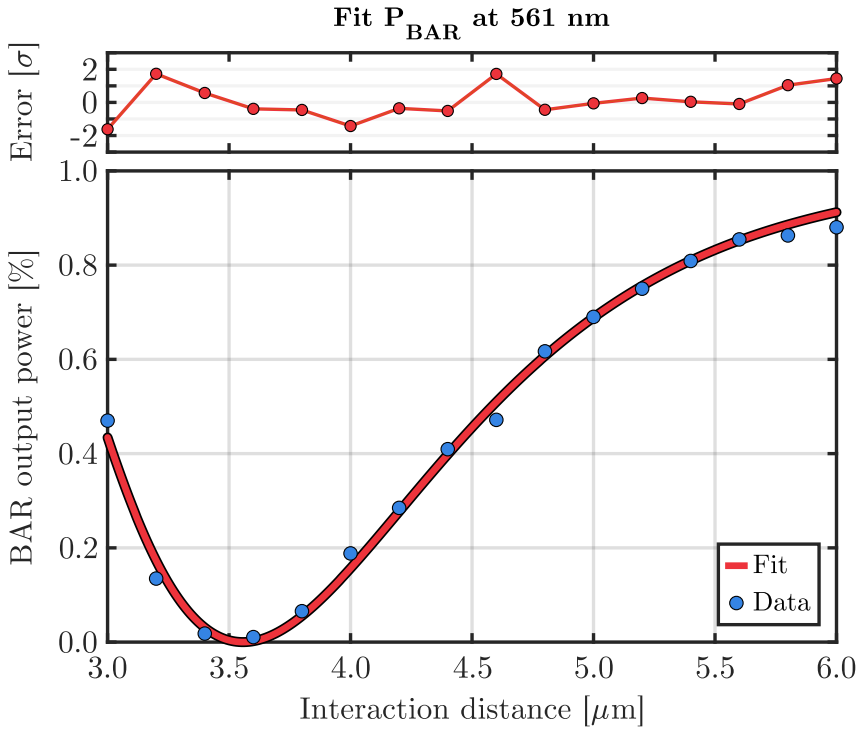

Figure 5.8: Bar output power measured at 561 nm of a set of couplers with $L = 0$ and d variable from 3.0 to 6.0 µm with step 0.2 µm.

length was fixed to a constant value $L \neq 0$. The lengths that have been explored are $L = 0.2, 0.5, 1, 2, 3$ mm.

The various sets of couplers have been measured yielding graphs like the one represented in figure 5.8. Each of the sets of experimental data has been fitted with the procedure described in this section and multiple couples of parameters $a^{(L)}$ and $b^{(L)}$ have been retrieved[3]. Graphically, it has been verified that the functions $k^{(L)}(d)$ retrieved from the different sets of couplers were different from each other and ordered with respect to the interaction length used, as can be seen in figure 5.9. In other words, it appeared to exist a monotonic dependence of the functions $k^{(L)}(d)$ on the value of the interaction length. To explore more clearly this dependence a number of interaction distances d_j have been selected. Then the coupling coefficient has been calculated at this value from each of the functions $k^{(L)}(d)$ retrieved. Finally, these values have been plotted versus the value of L leading to a chart like the one presented in figure 5.10.

[3] The notation utilized here with the superscript $^{(L)}$ is being used to explicitly state that the value considered has been retrieved for each of the sets of couplers fabricated at the different value of L.

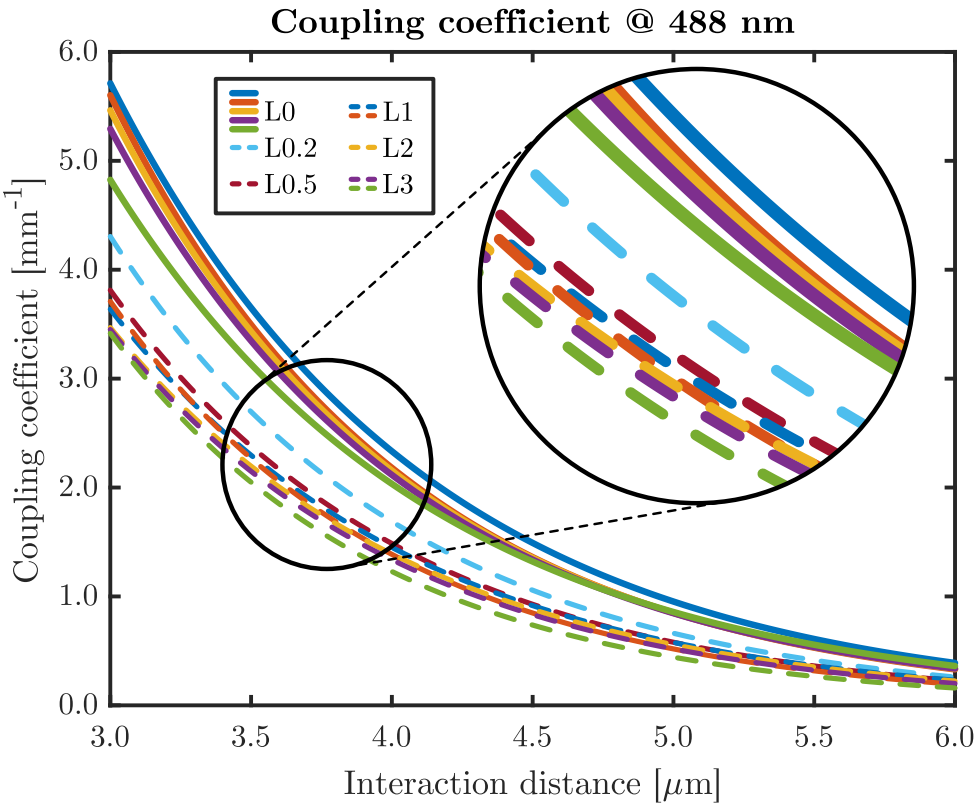

Figure 5.9: Representation of the functions $k^{(L)}(d)$ retrieved from several fit of couplers characterised by different values of interaction length. The solid lines represent $L = 0$ while the dashed ones $L > 0$. The zoom of one section highlights the distribution of the functions.

It can be seen here clearly the existence of a nonlinear dependence of $k(d)$ with respect to the interaction length. Furthermore, this chart highlights the fact that the values of k seem to stabilize after a transitory at a small interaction length. That is to say that the function $k(d)$ retrieved from a fit carried out at a "long" interaction distance is independent of L.

Considering the theory of directional couplers it is clear that such a dependence of k on L has no reason to exist. Therefore the error must arise from the fitting procedure carried out. We hypothesize that at small interaction lengths the fitting procedure is less accurate. In fact, as the contribution of the coupling given by the factor kL becomes smaller or comparable to the factor φ_0, corresponding to the coupling in the curved regions, it is possible that the retrieval of k with this fitting procedure becomes inaccurate and introduces an uncontrolled overestimation of k.

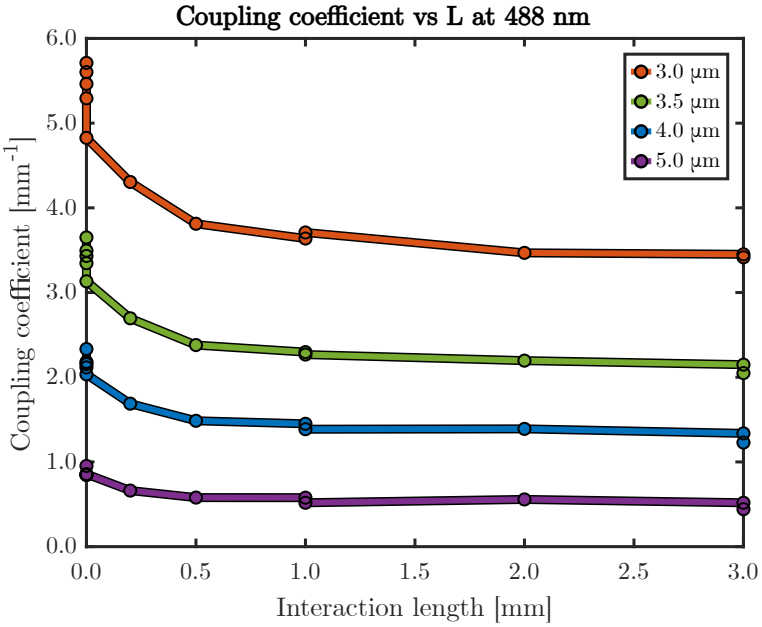

Figure 5.10: Coupling coefficient calculated at multiple d from fits of couplers realized at different fixed interaction L.

This study furthermore evidenced that the functions $k(d)$ retrieved at long interaction lengths were predictive of the coupling coefficients experimentally observed in the sinusoidal behaviour of the couplers. Therefore, it appears to be a good practice to retrieve the dependence of k from the interaction distance from the fit of couplers with an interaction length fixed at a high value. The length of $L = 3$ mm appeared to give robust predictions of the coupling coefficient of the couplers realized.

5.2.3. Analysis of the wavelength dependence of directional couplers

In section 1.2.2 it has been presented the wavelength dependence of directional couplers by studying the analytical expression of the parameters governing the interaction of optical modes supported by the waveguides. Here it is presented the study conducted on the effective dependence on λ of the coupling coefficient. Figure 5.11 summarizes a few results collected. The solid lines represent the coupling coefficients retrieved from the fit of two sets of couplers with variable interaction distance and fixed interaction length $L = 3$ mm. Collectively, the measurements have been taken at the wavelengths 488, 532, 561, 607 and 635 nm. From the experimental data points, the functions $k(d)$ have been extracted at each wavelength. Here are represented the coupling coefficients calculated at $d = 4.0$ μm from such fits. The green markers instead represent the values of the coupling coefficient

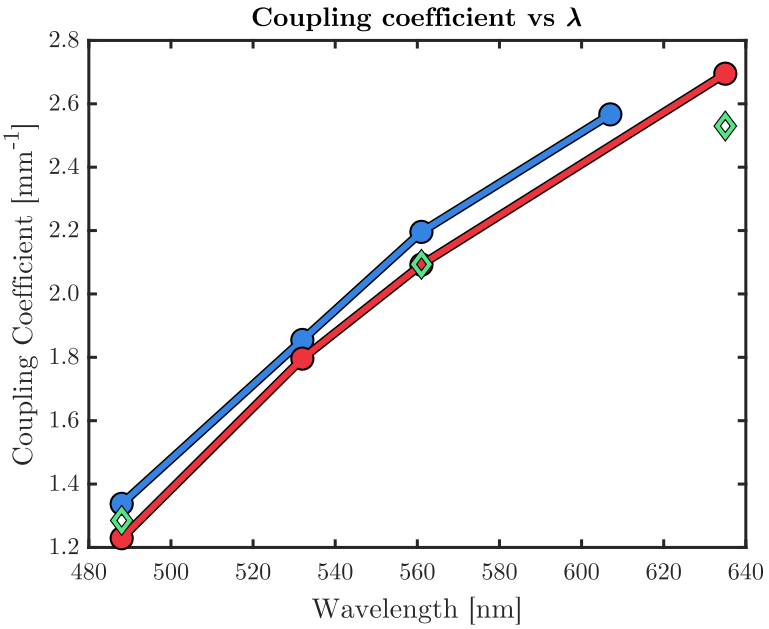

Figure 5.11: Experimental results of the coupling coefficient at $d = 4.0$ µm at multiple wavelengths. The red and blue lines represent the k retrieved from two distinct fits of k vs. d. The green marks the values of k of three fits vs. L.

extracted from the fit of the data belonging to three sets of couplers with variable L and fixed $d = 4.0$ µm. These last points are taken at 488, 561 and 635 nm.

It can be seen that there is a good agreement between the different types of fit and different fabrications. In fact, all these data points strongly suggest the linear dependence of k with the wavelength foreseen by the theory. We can therefore confirm that the synchronous coupler behaves as expected also concerning the wavelength dispersion. Furthermore, it confirms that a linear interpolation of such data can be confidently utilized to estimate the coupling coefficient pretty much over the entire visible spectrum.

Such linear dependence is not limited to the interaction distance selected, in fact, all the values of d investigated, thus in the range $3.0 - 6.0$ µm, are characterized by a similar dependence.† However, the slope $\partial k/\partial \lambda$ is not constant with the interaction distance. For this reason, to obtain complete control of the coupling coefficient a linear fit in wavelength of k computed at multiple interaction distances has been executed. In other words, it has been extracted from the data retrieved a 2D map of the coupling coefficient $k(d, \lambda)$. This allows investigating simultaneously different coupler geometries and their response at all wavelengths.

† Not shown.

From these studies has clearly emerged that the parameters describing the behaviour of directional couplers have a strong wavelength dependence, as expected from theoretical considerations. This wavelength dependence does not allow for the realization in a straightforward fashion of the desired splitters, that could work at multiple wavelengths or in a given bandwidth. For this reason, more complicated approaches have to be devised. The next chapter presents two distinct approaches that have been conceived with this aim.

6 | Multi-colour splitters

This chapter presents the work carried out towards the realization of multi-colour tritters, exploiting the information described in the previous chapter. Two distinct approaches are presented here. The first kind of device detailed is a splitter that is designed to meet the requirement of a specific splitting ratio at distinct wavelengths. The second kind of device is aimed at realizing splitters with the desired behaviour over an extended bandwidth, within a given tolerance.

6.1. Multi-colour tritter

In the field of biology, the measurements obtained by the imaging of a sample are considered significant when at least two fluorescent markers are evaluated. Typically, commercial fluorophores are designed to absorb specific illumination wavelengths, for this reason, it is worth investigating on the realization of power splitters working at selected wavelengths. The two following sections present the results of the study conducted towards the realization of tritters with operation at two and three selected wavelengths simultaneously. The method utilized will be described and its pros and cons will be highlighted. Furthermore, the results obtained from the experimental verification of such method will be presented.

6.1.1. Dual-Color Tritter

Here is reported the approach that has been followed to realize a tritter working at two distinct wavelengths. As it has been briefly introduced at the beginning of the previous chapter, what we refer to as a tritter is a device that splits the input power injected in a waveguide into three adjacent waveguides as equally as possible. The simplest geometry to achieve this power splitting is to first split the input power among two waveguides with ratios $33.\bar{3}\% - 66.\bar{6}\%$, then the waveguide in which is coupled $66.\bar{6}\%$ of the input power must split it with ratio 50%-50% with a third waveguide. Clearly, cascading these two different power splitters will result in the input power being shared equally by three waveguides. To realize such splitters synchronous directional couplers will be employed. Recalling the results of coupled mode theory presented in chapter 1, the power coupled

in the two waveguides is described by the equations 1.18, reported here for convenience.

$$\begin{cases} P_{BAR} &= \cos^2(kL + \varphi_0) \\ P_{CROSS} &= \sin^2(kL + \varphi_0) \end{cases}$$

As it has been discussed and analysed in the previous section both the coupling coefficient k and the initial phase φ_0 vary with the distance of the two waveguides, thus by fixing this distance the period of the sinusoid is known and the initial phase is also set. Then by choosing the correct length of the interaction region the desired splitting ratio at a single wavelength can be attained.

In order to obtain the same splitting ratio at two different wavelengths one has to find a geometry that satisfies both conditions. In other words, the two sinusoids describing the power coupled in the waveguides concerning both wavelengths match at the desired splitting ratio. This procedure is carried out numerically by scanning through possible combinations of interaction distances d and interaction lengths L until a geometry is found that yields an overall error from the target splitting ratio small enough.[1] In this case, error is meant as the distance of the BAR output power from the target value summed over both wavelengths. Typically, many solution geometries are easily identified with such a method and the error from the target is smaller than 0.5% at both wavelengths thus negligible if compared with the potential error stemming from the non-perfect reproducibility of the fabrications. Algorithm 6.1 reports the pseudo-code of the procedure used to identify the coupler with desired splitting ratio.

[1] Notice that standard minimization methods pre-built in common software like Matlab, are not viable since the error function, as it was defined above, presents plenty of local minima such algorithms tend to fall into, failing to identify more optimal solutions.

Algorithm 6.1 Dual colour coupler finder

```
Define target splitting ratio T
for d in range do
    Calculate coupling coefficient k and φ0 at each wavelength
    for L in range do
        Compute BAR(k, L, φ0) power at each wavelength
        Calculate distance from target ε = Σλ|BAR − T|
        if ε is the smallest then
            Save current geometry [d, L]
        end if
    end for
end for
Return best geometry found
```

This approach could theoretically be used to realize devices working at two arbitrary wavelengths but in practice, multiple constraints restrict the realm of possible devices that can be realized.

- Concerning the distance of the selected wavelengths, it is easy to picture that the closer two wavelengths are, the higher the number of power oscillations required before the sinusoids accumulate a significant phase difference is. Consider the case of two sinusoids — corresponding to two distinct wavelengths — of frequencies k_1, k_2 and phases φ_1, φ_2. We want to identify the length L such that both sinusoids take value T, thus:

$$\cos\left(k_{1,2}L + \varphi_{1,2}\right) = T$$

$$k_{1,2}L + \varphi_{1,2} = \cos^{-1} T + 2m_{1,2}\pi$$

$$L = \frac{\cos^{-1} T + 2m_{1,2}\pi - \varphi_{1,2}}{k_{1,2}}$$

  Now imposing the length L equal for both wavelengths:

$$\frac{\cos^{-1} T + 2m_1\pi - \varphi_1}{k_1} = \frac{\cos^{-1} T + 2m_2\pi - \varphi_2}{k_2}$$

$$m_1k_2 - m_2k_1 = \frac{\varphi_1k_2 - \varphi_2k_1 - \cos^{-1} T\left(k_2 - k_1\right)}{2\pi}$$

  Now, in the case of nearby wavelengths, the frequencies of the two sinusoids will be similar but not equal. Thus we impose that the phase difference accumulated is the smallest possible still able to grant the perfect match at the target T. Therefore

setting $m_{1,2}$ such that $m_2 = m_1 + 1$ we obtain the following: [2]

$$m_1 = \frac{k_1}{k_2 - k_1} + \frac{\varphi_1 k_2 - \varphi_2 k_1}{2\pi\,(k_2 - k_1)} - \frac{\cos^{-1} T}{2\pi}$$

This expression tells us that as the difference between the frequencies k_1, k_2 gets smaller, the larger is the propagation length required to obtain a solution, since

$$L \propto m_1 \xrightarrow{k_2 - k_1 \longrightarrow 0} +\infty$$

Through numerical simulations it was evidenced that selecting wavelengths with a distance below ∼30 nm lead to no viable solutions to be identified in the desired working range $3.0\,\mu m \leq d \leq 6.0\,\mu m$, $0\,mm \leq L \leq 5.0\,mm$.

- Even with an appropriate selection of the working wavelengths, the device has limitations on the length of the interaction regions. In fact, firstly there is to consider the physical limitations of the substrate dimensions and secondly, the goal of the project is to realize reasonably compact devices thus the interaction regions must be limited in dimensions.

- Both these issues can be relieved by designing devices with smaller interaction distances since the frequencies of the sinusoids increase. In reality, though, there is a lower limit for the distance of the waveguides. In fact, the fabrication through FLM of waveguides too close to one another can deteriorate their guiding properties causing them to behave improperly. Furthermore, the coupled mode theory that is used to describe the behaviour of directional couplers stands on the assumption of weak coupling, thus it is fair to say that positioning two waveguides in close proximity to one another could determine a violation of this assumption and lead to devices with properties not correctly resembled by the theoretical simulations.

This method allowed to identify geometries of directional couplers with BAR output powers $33.\bar{3}\%, 50\%$ and $66.\bar{6}\%$, at the working wavelengths 488 nm and 561 nm. With these simulations, we have thus verified the possibility to obtain the desired device. The next section will detail the realized configuration as well as the experimental results obtained.

Following the procedure described in the previous section, two geometries were selected to realize the two couplers to be cascaded to realize the tritter. In the table 6.1 are reported such geometries as well as the error from the target splitting ratio at both wavelengths.

[2] Imposing this relation between the values of $m_{1,2}$ is requiring that the two sinusoids meet at the target after only one period of shift. Imposing a bigger phase difference will require even longer propagation lengths.

Interaction Distance	Interaction Length	Target Splitting Ratio	Error at 488 nm	Error at 561 nm
3.565 µm	1.4264 mm	$66.\bar{6}$ %	-0.202 %	+0.008 %
3.950 µm	1.2412 mm	50.0 %	+0.102 %	-0.009 %

Table 6.1: Description of the couplers chosen to realize the dual colour tritter 488/561.

To account for the intrinsic and uncontrollable variability of the fabrications it was realized not just the target device but also a number of other devices where the interaction length was varied in the neighbourhood of the target one. The reasoning behind this choice is that a variation in the value of the coupling coefficient will have the effect of stretching or contracting the expected sinusoidal behaviour of the power in the waveguides, thus causing the fabricated device to miss the target splitting ratio value. Therefore, fabricating devices with varied interaction lengths should allow the identification of a device delivering the desired output power split. In fact, it was chosen to vary the interaction length from 80% of the target length up to 132% with a variable step of 2% and 1%. The interaction lengths of both couplers constituting the tritter were varied by the same amount relative to the target value, as it has been assumed that a fluctuation in the value of the coupling coefficient, due to the intrinsic variability, will impact equally both couplers.

Regarding the other parameter that can be tuned, the interaction distance, it was chosen to keep it fixed. Since varying this parameter, the coupling coefficients at both wavelengths are affected, thus impacting also on the target length required to obtain the desired splitting ratio, leading to the necessity to alter both parameters at once, vastly complicating the design procedure. As a matter of fact, since the periods of the two sinusoids change by different amounts in response to the same change on d, the error from the target splitting ratio is likely to increase significantly.

To evaluate the performance of the tritter we decided to evaluate not only the splitting ratio but also an important parameter in the field of microscopy. The chosen parameter is the modulation ratio which is introduced and evaluated in appendix A. Here is reported its final expression A.5 as a function of the intensities of the output beams.

$$M = \frac{\sqrt{I_1 I_2} + \sqrt{I_1 I_3} + \sqrt{I_2 I_3}}{I_1 + I_2 + I_3}$$

This parameter allows a straightforward analysis of the data and allows us to link the issues of intensity unbalance to a relevant concept in microscopy, which is the ultimate

application of the devices realised in this project. In fact, the modulation depth of the final pattern, and thus of the raw image of the specimen, is an important factor in determining the reconstructed image quality — with the methods described in the chapter 3 — as it affects the amount of frequency-shifted information that can be retrieved in the reconstruction [55].

The batch of the fabricated devices were then measured at both target wavelengths. Table 6.2 reports the output power measured at the three outputs as well as the modulation ratio of the best device fabricated. Notice that the best device does not exactly correspond to the target device reported in table 6.1 but it is in close proximity. In fact, the selected device corresponded to a variation of the interaction lengths of the couplers, with respect to the design value, of +2%. To identify this device was considered the value of the modulation ratios averaged over the two wavelengths, thus the device with the overall better performance considering both colours.

$\lambda = 488\ nm$		$\lambda = 561\ nm$	
Output Power	**Modulation Ratio**	**Output Power**	**Modulation Ratio**
38.9 %		32.8 %	
33.8 %	99.24 %	35.8 %	99.89 %
27.4 %		31.4 %	

Table 6.2: Results of the best dual colour tritter 488/561 fabricated.

The results here gathered appear to be optimal as the modulation ratio does not drop even 1% below the ideal value, proving that the method described in this section for the realization of splitters with accurate splitting ratios at multiple wavelengths is indeed valid.

6.1.2. Tri-Color Tritter

It is easy to comprehend that the same conceptual approach presented in the previous section for the realization of dual-colour couplers, could be, in principle, applied to an arbitrary number of wavelengths. In fact, at each wavelength corresponds a sinusoid with a given initial phase and frequency, thus if these features are known for each one of the wavelengths of interest it is sufficient to find the geometry that allows for these sinusoids to reach the target splitting ratio simultaneously. This analysis can be realized with the

same exact algorithm 6.1 presented previously, which has been written on purpose to be compatible with an arbitrary number of wavelengths. In practice, however, the addition of multiple target wavelengths restricts the space of possible solutions until eventually, no valid design can be found.

To test the capabilities of this approach it was chosen to tackle the more challenging issue of realizing a tritter designed to work at three wavelengths simultaneously. Along with the two wavelengths utilized in the previous case, 488 and 561 nm, the wavelength of 635 nm was chosen as the third target. In table 6.3 are reported the two coupler geometries that have been selected for the realization of this device, along with the target spitting ratio as simulated with the data available. To counteract the effects of the fabrication variability 44 devices were realized varying the interaction length from 80% to 120% of the target value with variable steps of 2%, 1%, 0.5% and 0.1%.

Interaction Distance	**Interaction Length**	**Target at 488 nm**	**Target at 561 nm**	**Target at 635 nm**
4.305 μm	4.0190 mm	33.5 %	35.4 %	33.2 %
5.465 μm	2.6880 mm	50.1 %	48.9 %	50.0 %

Table 6.3: Description of the couplers chosen to realize the dual colour tritter 488/561.

Here in table 6.4 are reported the results of the best tritter working at the design wavelengths of 488, 561 and 635 nm. It is worth highlighting that also in this case the best device was identified in the close neighbourhood of the target design reported in table 6.3. In fact, this device corresponded to a variation of +1.4% with respect to the design interaction lengths.

$\lambda = 488\,nm$		$\lambda = 561\,nm$		$\lambda = 635\,nm$	
$\mathbf{P_{out}}$	**M**	$\mathbf{P_{out}}$	**M**	$\mathbf{P_{out}}$	**M**
29.1 %		26.2 %		46.1 %	
41.7 %	98.88 %	35.5 %	99.06 %	27.8 %	97.41 %
29.1 %		38.3 %		26.1 %	

Table 6.4: Results of the best tri-colour tritter 488/561/635 fabricated.

The trend of the measured output power was rather more noisy than in the case of the devices shown in the previous section, nonetheless, it was possible to identify a device capable of splitting the input intensity with reasonable accuracy at three distinct wavelengths. In fact, the modulation ratio still takes almost unitary value at all three wavelengths.

Closing this section is worth highlighting that the approach described has been simulated for the realization of a device working at four distinct wavelengths. It has been found a possible implementation of a tritter at the working wavelengths of 425, 503, 581 and 660 nm. The wavelengths have been selected considering the existence of a fluorophore that could be excited with such photon energies, but the choice was strictly linked to the existence of a viable device geometry. In fact, most of the combinations of wavelengths that have been tested did not yield satisfactory results in the range considered. For this reason, it is hard to envisage a device exploiting this design principle that could work at 5 wavelengths or more, although the relaxation of some constraints, e.g. allowing for longer interaction length, could alleviate this issue and grant a broader range of solutions to be identified.

6.2. Broadband tritter

This section will present the study realized towards the realization of broadband couplers, that is devices working as power splitters in a given band of wavelengths. Conversely to the method presented in the previous section, these devices are not targetted at single wavelengths but at a broad spectrum. To realise these devices the properties of asynchronous directional couplers will be employed.

6.2.1. Asynchronous couplers

In this section, it is analysed the exploitation of asynchronous couplers to obtain an improved spectral response compared to the synchronous counterpart. Recalling section 1.2, a coupler is defined as asynchronous when it is composed of non-identical waveguides respectively characterised by the propagation constants β_1 and β_2 of their guided modes. The parameter $\Delta\beta \triangleq \beta_1 - \beta_2$, defined as detuning, is an important factor in determining the behaviour of the coupler as it will be detailed in the following. As described above, the response of directional couplers is strongly dependent on the wavelength of the light injected into them. This dispersion of the response in a directional coupler is determined by the direct wavelength dependence of the coupling coefficient. Selecting a target splitting ratio and a tolerance on this value, we define as bandwidth the range of wavelengths at which the output power is, within the given tolerance, close to the desired splitting

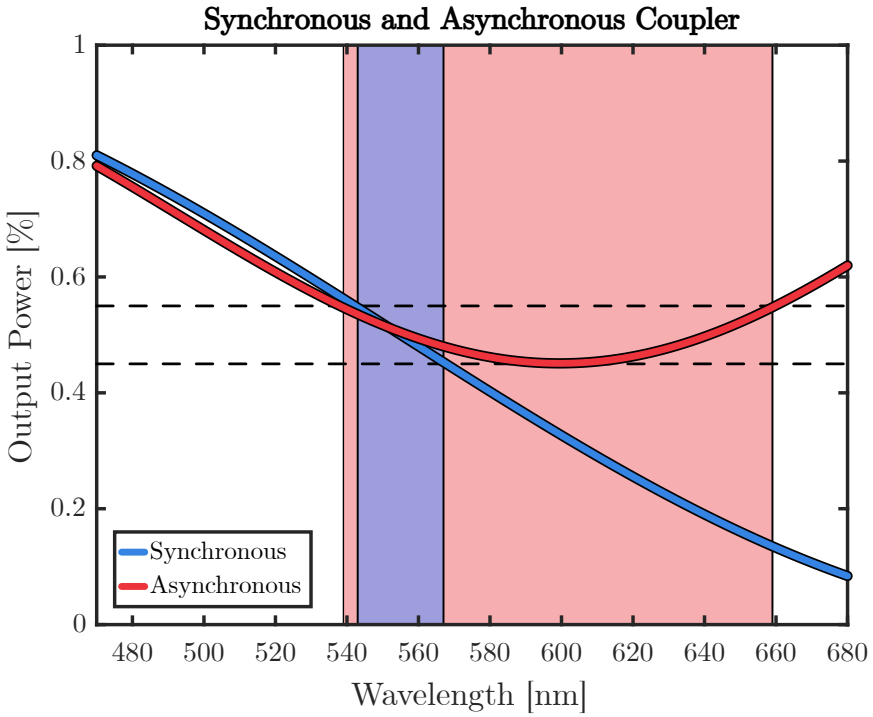

Figure 6.1: Comparison of output BAR power with respect to λ of synchronous and asynchronous couplers.

ratio. Because of the strong dependence of k on λ, the bandwidth of synchronous couplers demonstrates to be quite small. In figure 6.1 is represented, with a blue line, the behaviour of a synchronous coupler with $P_{BAR} = 50\%$ at $\lambda = 555$ nm. Its bandwidth, with the choice of tolerance of $\pm 5\%$, is the one highlighted in blue. The red colour instead represents the response of an asynchronous coupler ($\Delta\beta = 1.89k$ at $\lambda = 555$ nm) and its corresponding bandwidth, measured with the same tolerance. It is evident that the asynchronous coupler offers a much broader bandwidth than its synchronous counterpart.[3]

The wavelength dependence of an asynchronous coupler is quite complex to analyse as it is influenced by the parameter $\Delta\beta \sim {}^1/\lambda$. It is therefore not straightforward to comprehend the possible advantages of the exploitation of this kind of device. Recalling the results of coupled mode theory, the output power of an asynchronous coupler reads as follows:

$$P_{BAR} = 1 - \frac{k^2}{k^2 + \frac{\Delta\beta^2}{4}} \sin^2\left(\sqrt{k^2 + \frac{\Delta\beta^2}{4}} L + \varphi_0\right)$$

Analysing the coefficient which multiplies the *sin* function, one can see that with a strong detuning — that is with a high value of $\Delta\beta$ relative to k — the dynamic of the sinusoidal

[3] Of course this can be obtained with an accurate selection of the parameters.

function is reduced. This means that the dispersion of the wavelength caused by the argument of the sin function is diminished. Notwithstanding the complexity of the wavelength dependence of this kind of device, numerical simulations have proven the existence of potential for improvement in the bandwidth of directional coupler splitters. Therefore, bearing this goal in mind, this section will tackle the work performed in the realization of asynchronous couplers.

Realization of detuning

To realize asynchronous couplers it is necessary to fabricate waveguides that are characterized by two different propagation constants $\beta_{1,2}$ of their respective guided mode. Since the propagation constant is dependent on the refractive index of the waveguide by tuning the fabrication parameters it is possible to realize detuned waveguides, resulting in $\Delta\beta \neq 0$. Here are presented four methods that have been tested to achieve this goal.

Quill-effect The quill effect describes the peculiar phenomenon, that is experienced in femtosecond-laser written structures, according to which the writing direction influences the modification of the material. This means that the structures that are inscribed in the material possess different properties when they are written in different directions. This effect can be caused by an anisotropy of the frequency distribution — that is, a frequency chirp — of the laser pulses which causes a tilt of the intensity distribution of the pulse. [56] Since the writing direction can affect the structure that is inscribed in the material it is possible that the propagation constant of light could also be influenced. To test the magnitude of this effect it was chosen to realize a set of couplers in which the two arms were written in two different directions. It is in fact expected that if a quill-induced detuning is visible it should be exacerbated by this fabrication process. The set of 11 couplers fabricated was characterized by an interaction distance fixed at 4.0 μm and an interaction length variable from 2.5 to 5.0 mm with step 0.250 mm.

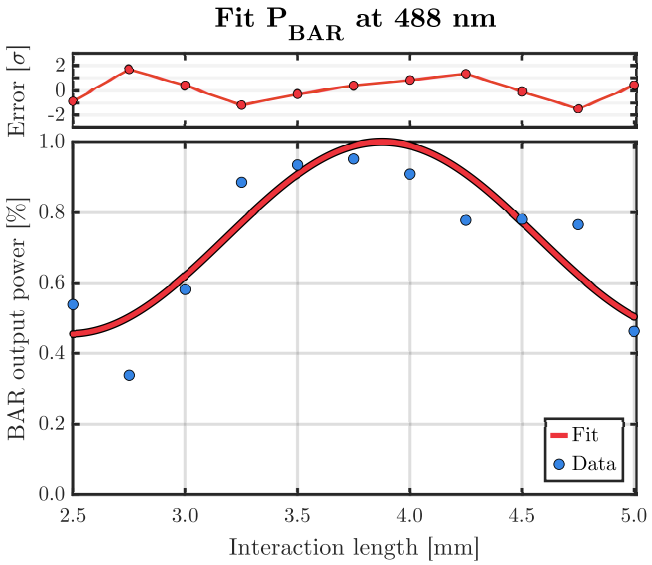

Figure 6.2: Bar output power measured at 488 nm of a set of couplers with $d = 4.0\mu m$ and L variable from 2.5 to 5.0 mm with step 0.250 mm realized to test the detuning of the quill effect.

Here in figure 6.2 is reported the result of the measurement and the fit realized at 488 nm. As it can be seen, the quill effect seems to be able to provide a considerable detuning which was estimated to be $\Delta\beta = 1.52$ mm^{-1} compared to a coupling coefficient $k = 0.83$ mm^{-1}. This value of detuning almost allows for realizing a coupler with a maximum power transfer of 50%. Unfortunately, at higher wavelengths, where the coupling is stronger, such detuning results to be insufficient. Nonetheless, it doesn't seem to be feasible to increase the magnitude of the detuning therefore the only possibility would be to increase the interaction distance to lower the value of k to enhance the detuning effect. Furthermore, controlling the writing direction doesn't seem to allow much room to tune the detuning to match the desired value accurately. In conclusion, detuning can be obtained by exploiting the quill effect but the results are not satisfactory.

Variable depth An alternative method that has been tested for the realization of detuning is to change the depth of the waveguide in the interaction region. In fact, previous works have evidenced that the writing depth can impact the characteristics of the waveguides, thus it is possible that writing the two arms of a coupler at different depths may determine the presence of a detuning. To test this hypothesis two sets of couplers have been realized in which one of the two arms has been written at distance Δh of 1.5 and 3.0 µm in the vertical direction — that is to say, the direction of propagation of the laser beam in the fabrication setup. The interaction distance was fixed to 4.0 µm

with an interaction length variable from 2.5 to 5.0 mm with step 0.250 mm. The arms were positioned in the plane such that their distance was equal to the one selected.

In figure 6.3 are visible the results of the measurement performed at 488 nm on the set written with $\Delta h = 3.0$ µm. This study evidenced that the vertical distance of the two waveguides is not sufficient to provide a significant detuning. In fact, the vertical offset of one of the arms of the coupler cannot be increased arbitrarily as it is capped by the chosen interaction distance. Furthermore, setting the vertical offset to the maximum value that is $\Delta h = d$ would mean fabricating one of the waveguides passing through the one above which is a practice that could probably lead to the waveguide performing less than ideally. For these reasons, this methodology is considered unsuitable to obtain asynchronous couplers.

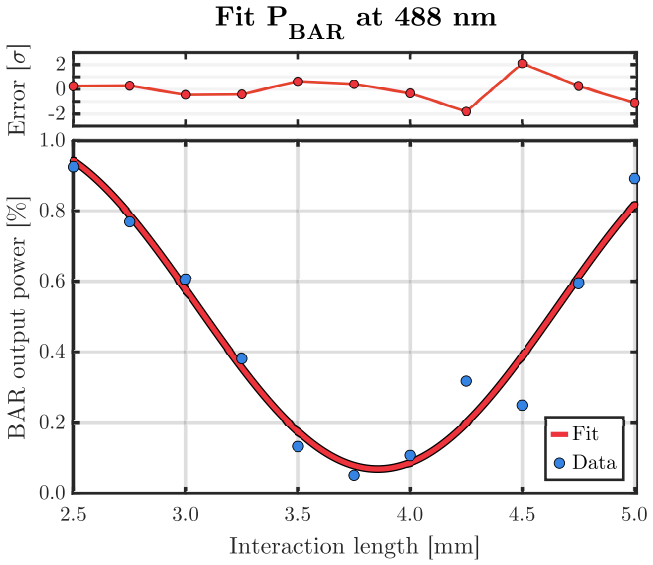

Figure 6.3: Bar output power measured at 488 nm of a set of couplers with $d = 4.0$ µm, L variable from 2.5 to 5.0 mm with step 0.250 mm and $\Delta h = 3.0$ µm realized to test the detuning effect of different writing depths.

Scan alternation It has been mentioned previously the waveguides utilized in this work are fabricated by repeated irradiation of the same line for 8 scans. The realization of the couplers has been realized by alternating the scans of the two arms as it is expected to alleviate the possible problems that could arise from the fabrication of two waveguides close to each other, as they are in the interaction region. Here is presented a test that has been carried out to gauge the possibility to obtain non-identical waveguides by changing the way the scanning procedure is carried out. In fact, it is possible that the fabrication of the first arm determines a modification of the material in the region corresponding to the adjacent arm thus the realization of the second arm occurs on a material that is

not pristine and may lead to a waveguide with slightly different guiding properties. Or it could be the case that the irradiation of the second arm may influence the already present modification corresponding to the first arm. Ultimately, it is safe to assume that both forms of "fabrication cross-talk" may concur with the formation of non-identical waveguides. Clearly, if such an effect is existing its impact should be maximum when the first arm is fabricated in its entirety before the second one.

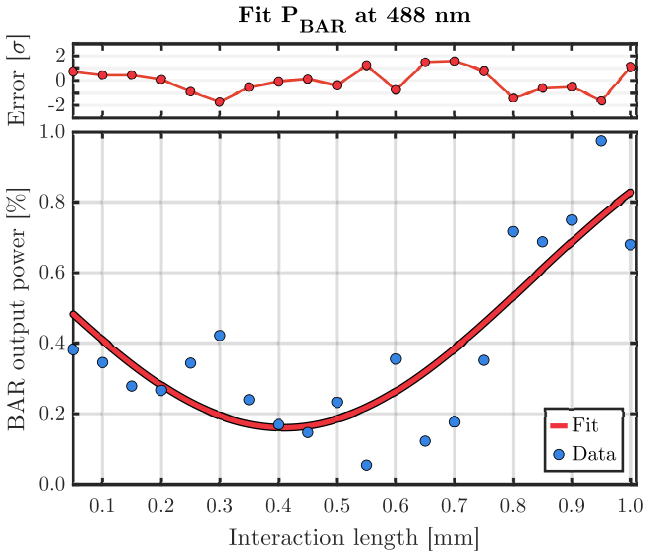

Figure 6.4: Bar output power measured at 488 nm of a set of couplers with $d = 4.0$ µm, L variable from 2.5 to 5.0 mm with step 0.250 mm and $\Delta h = 3.0$ µm realized to test the detuning effect of different writing depths.

Reported in figure 6.4 are the results measured at 488 nm of a set of couplers with $d = 4.0$ µm and L variable from 0 to 1 mm with step 0.05 mm realized without the scan alternation. It can be seen that a detuning effect is determined by this fabrication procedure but at the same time the behaviour of the coupler results to be rather noisy. Notwithstanding the noise, the entity of the detuning is still not high enough to be utilized in a meaningful way. Finally, the same reasoning detailed regarding the use of the quill effect apply in this case too: it is hard to imagine how the scan alternation can be tweaked to obtain the desired detuning value.

Variable writing velocity Here are presented the tests that have been carried out to experiment on the realization of detuning by changing the writing velocity of a coupler. In fact, it has been observed experimentally in this work that the writing velocity does have an impact on the waveguides realized, which is reflected in the difference in performance in terms of losses. Furthermore, in the literature, several studies are present regarding

the fabrication of asynchronous couplers with such a procedure. [57]

Multiple sets of couplers have been realized by keeping one arm fixed at the writing velocity of 40 mm/s, while the other arm was written with a wide range of velocities, ranging from 32 to 48 mm/s. In figure 6.5 are presented the results of one of such measurements realized at 488 nm. The set of couplers was realized with $d = 4.0$ µm, L variable from 2.5 to 5.0 mm with step 0.250 mm with one arm written at 40 mm/s and the other at mm/s. As can be seen in the figure this procedure resulted in considerable detuning, far greater than the ones obtained with the other methods. Furthermore, this approach has the advantage of being directly tunable, in fact, simply by selecting the appropriate velocity for the two arms the detuning can be tweaked to be equal to the desired value. This offers a finer control which the other methods analysed lack.

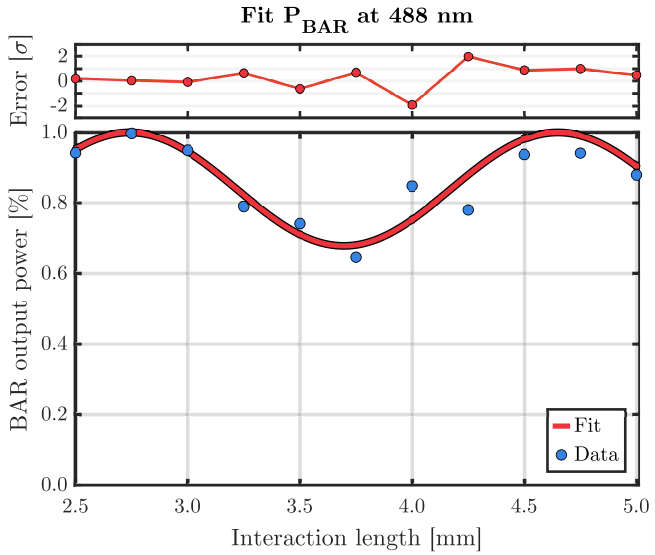

Figure 6.5: Bar output power measured at 488 nm of a set of couplers with $d = 4.0$ µm, L variable from 2.5 to 5.0 mm with step 0.250 mm and $\Delta h = 3.0$ µm realized to test the detuning effect of different writing depths.

Since the results showed were promising, a complete characterization of these sets of couplers has been carried out to analyse both the dependence of the detuning realized with a given velocity difference and the dependence of the detuning as a function of the wavelength. The wavelengths utilized for these measurements are 488, 561 and 635 nm.

Figure 6.6 shows the values of the detuning $\Delta\beta$ obtained by analysing and fitting each set of couplers like the one represented in figure 6.5, as a function of velocity difference Δv from 40 mm/s. Looking at the experimental value retrieved for $\Delta\beta$ it appears to exist a linear dependence with the velocity variation. Therefore, at each wavelength was

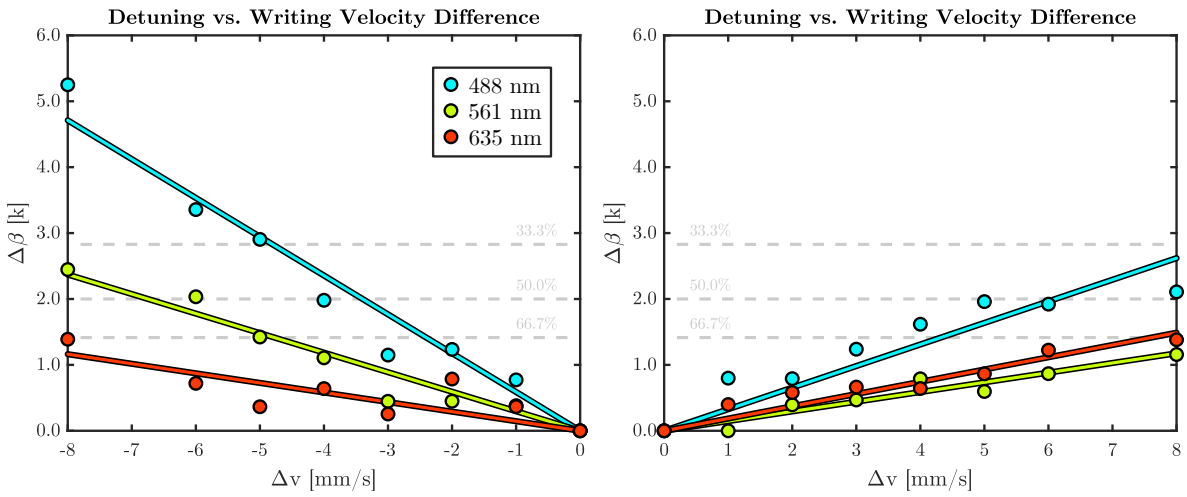

Figure 6.6: Results of the fit of the sets of asynchronous couplers at the wavelengths 488, 561 and 635 nm versus the writing velocity of one arm. The value of $\Delta\beta$ is expressed in units of k obtained in the same fit.

performed a linear fit, which yielded the result plotted on the graph.

The value of $\Delta\beta$ has been expressed in units of the coupling coefficient k obtained in the same fit. In fact, it has been seen that the trend of $\Delta\beta$ versus the writing velocity of the different arms of the coupler appears less noisy. It is possible that because of the noisiness of the experimental data both $\Delta\beta$ and k are estimated with a more significant error, yet expressing $\Delta\beta$ in units of k partially cancels out this variability yielding cleaner data. In this representation are also evidenced by grey lines the values of $\Delta\beta$ required to obtain a maximum power transfer of 33%, 50% and 66% which highlights the strength of the detuning that can be obtained at the various wavelengths with a given velocity change.

In table 6.5 are reported the values of the slope obtained by the linear fit of $\Delta\beta$ versus $|\Delta v|$. The velocity difference has been taken in absolute value so as to deal with positive quantities in the fit.

Wavelength	Slope
488 nm	0.664 mm^{-1}/mm/s
561 nm	0.557 mm^{-1}/mm/s
635 nm	0.361 mm^{-1}/mm/s

Table 6.5: Summary of the slopes of $\Delta\beta$ vs. Δv resulted from the fit at different λ.

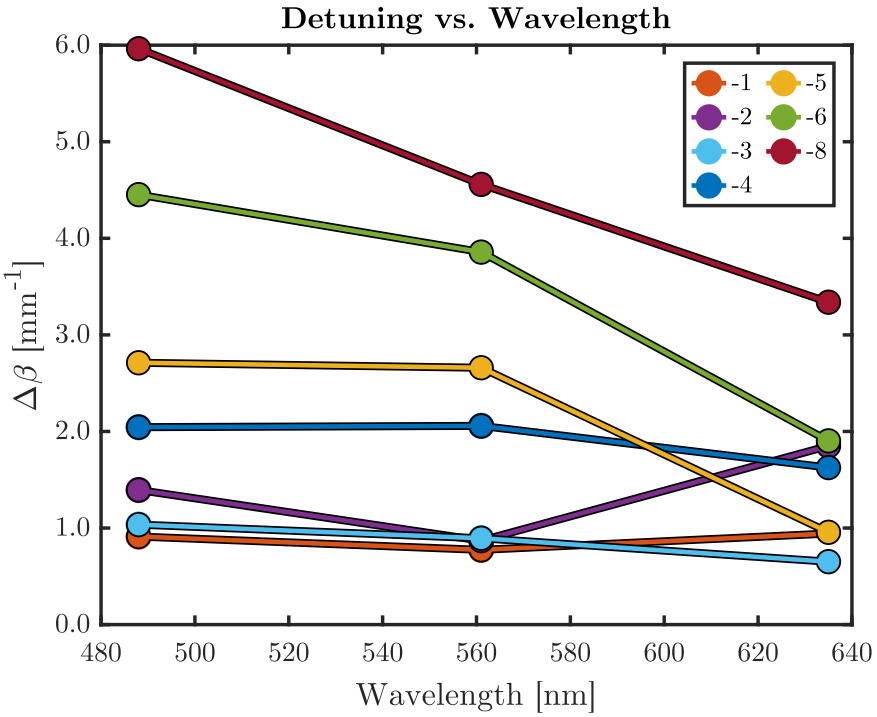

Figure 6.7: Detuning coefficients obtained at the wavelengths 488, 561, and 635 nm. Each line corresponds to a value of velocity difference Δv.

Detuning Wavelength dependence

Now that a method for the realization of detuned waveguides has been identified, we are interested in the wavelength dependence of the detuning coefficient. In fact from the theory of optical waveguides, we expect to see a wavelength dependence of $\Delta\beta$ of the type of $1/\lambda$. To evaluate this dependence the detuning obtained at each of the values of the velocity difference was plotted against the wavelength, as represented in figure 6.7. Unfortunately from the data retrieved no match could be identified with the wavelength dependence expected from the theory. In fact, data fitting with a dependence of the type $1/\lambda$ yielded unsatisfactory results. Admittedly, the theory of directional couplers describes the existence of an ulterior factor that may influence the wavelength dependence of the detuning coefficient. In fact, $\Delta\beta$ is also dependent on the effective refractive index of the guiding structure corresponding to both waveguides, which is a function of the wavelength too. It may thus be the case that this additional factor influences the observed dependence of $\Delta\beta$ on the wavelength.

Notwithstanding the origin of such dependence, it was chosen to proceed in the realization of broadband devices considering the dependence on λ observed experimentally. The fitting of the data points with a linear model yielded marginally better results and thus

was utilized for the subsequent works. To be precise, recalling the results of the previous section, $\Delta\beta$ appears to be a linear function of the velocity difference of the coupler's arms and the slope of this linear dependence is a function of the wavelength. Therefore, to simulate the response of an asynchronous coupler with respect to the wavelength, all the data points $\Delta\beta(\Delta v, \lambda)$ have been fitted with the following function:

$$\Delta\beta(\Delta v, \lambda) = m(\lambda)|\Delta v| = (m_1\lambda + m_2)\,|\Delta v|$$

6.2.2. Broadband coupler design

This section reports the method utilized to design broadband couplers at a specific target splitting ratio. As it has been presented previously to achieve this goal we will exploit asynchronous couplers, which allow for a flatter response with respect to the wavelength. Algorithm 6.2 reports the pseudocode describing the numerical procedure carried out to identify the fabrication parameters matching the desired characteristics. The structure of the algorithm is similar to the one presented in section 6.1.1 for the realization of dual-colour couplers, with a different metric for the identification of the best device. In fact, in this case, there are two requirements that the coupler has to meet: firstly, the splitting ratio must meet the target one and secondly, the bandwidth must be maximized. To combine these two requirements a composite cost function was created. The initial selection of two wavelengths is used to fix the position of the working bandwidth in the spectrum. The distance ε from the target splitting ratio is evaluated at these wavelengths. The bandwidth BW is calculated as the range of wavelengths at which the splitting ratio is within a specified tolerance from the target. The cost function to be minimized is defined as the ratio between the error ε and the BW elevated to a power $\alpha > 1$. Clearly, the cost function is minimized when the error from the target is minimized and the bandwidth is maximized. The elevation to the power α is utilized to amplify the effect of the larger bandwidth in spite of a smaller error from the target. The bigger the coefficient α the more solutions with a larger bandwidth will be ranked higher even if the error from the target is non-optimal. The algorithm then scans through all the possible combinations of d, L and Δv evaluating the error function in search of an adequate solution.

Algorithm 6.2 Broadband coupler finder

```
1: Define target splitting ratio T
2: Indicate target wavelengths λ_j
3: Define tolerance from the target, err
4: for d in range do
5:     Calculate coupling coefficient k and φ_0 at all wavelengths
6:     for Δv in range do
7:         Calculate detuning coefficient Δβ at all wavelengths
8:         for L in range do
9:             Compute BAR(k, L, φ_0, Δβ) power at all wavelengths
10:            Calculate distance from target ε = Σ_λj |BAR − T|
11:            for λ in range do
12:                if |BAR − T| < err then
13:                    Increment bandwidth BW
14:                end if
15:            end for
16:            if ε/BW^α is the smallest then
17:                Save current fabrication parameters [d, L, Δv]
18:            end if
19:        end for
20:    end for
21: end for
22: Return best fabrication parameters found
```

With this method, multiple fabrication parameters have been identified yielding broadband couplers. It was, in fact, possible to simulate possible devices at the splitting ratio of $33.\bar{3}\%$, 50% and $66.\bar{6}\%$ with bandwidths as large as 100 nm.

The simulations evidenced a connection between the controllable parameters and the maximum bandwidth attainable. The solutions characterised by the larger bandwidth are obtained for a short interaction length. The reason for this fact is that an important component of the wavelength dispersion is the frequency of the sinusoid and for a short interaction length the dispersion introduced is limited. Furthermore, it appears that a small interaction distance also reduces colour dispersion. At a short interaction distance, the frequency of power exchange becomes more efficient thus it is required a short interaction length to reach the desired splitting ratio, allowing for greater bandwidth for the reason just discussed. Finally, these solutions are characterised by a high value of velocity

difference. This becomes necessary since at a small interaction distance the coupling coefficient takes a high value, thus it is required to introduce a large value of $\Delta\beta$ to obtain the desired detuning.

6.2.3. Broadband results

To assess the possibility to realize broadband couplers, with the method described in the previous section, several couplers have been fabricated and measured. It was chosen to realize couplers centred around different wavelength ranges and different bandwidths, therefore with different sets of fabrication parameters. In the previous section, it has been explained how the simulations yield devices with particularly large bandwidths when the interaction distance is kept small and the detuning is high. As already discussed in this work, possible issues might occur in the fabrication of waveguides that are too close to one another, therefore it was chosen to also explore sub-optimal solutions with a greater interaction distance and a smaller bandwidth. Furthermore, increasing the interaction distance allows for smaller detuning and thus the realization of waveguides that are not too distant from the ones studied in this work.

To contrast the possible variability in the fabrication it has been decided to fabricate the couplers not only with the design parameters obtained by the simulation but also in their neighbourhood. The interaction length and the interaction distance were kept fixed at the design value while the velocity difference was varied around the target value. Varying the detuning introduced in the coupler has the effect of raising or lowering the expected response around the target splitting ratio without disrupting excessively the bandwidth.

Figure 6.8, on the left, reports the results of one such device. The coupler was realized with interaction distance $d = 5.955$ µm, interaction length $L = 3.023$ mm and a velocity difference $\Delta v = -1.6$ mm/s. The blue line reported in the figure represents the simulated output power at the BAR port with respect to the wavelength. The dashed black line indicates the target splitting ratio, equal to 66%. The red-shaded region highlights the predicted bandwidth, calculated with a tolerance of ±5%, which amounts to 49 nm. The region of working wavelengths was centred by design between 532 and 561 nm. The black markers indicate the measurement taken on this device at these two wavelengths.

A second result obtained is reported in figure 6.8 on the right. The coupler was realized with parameters $d = 4.25$ µm, $L = 1.006$ mm and $\Delta v = -3.8$ mm/s. This device is targeted at the same splitting ratio but centred around the wavelengths 488 and 532 nm with a simulated bandwidth amounting to 69 nm. The result of the measurement of the output power taken at these two wavelengths are represented by the black stars in the

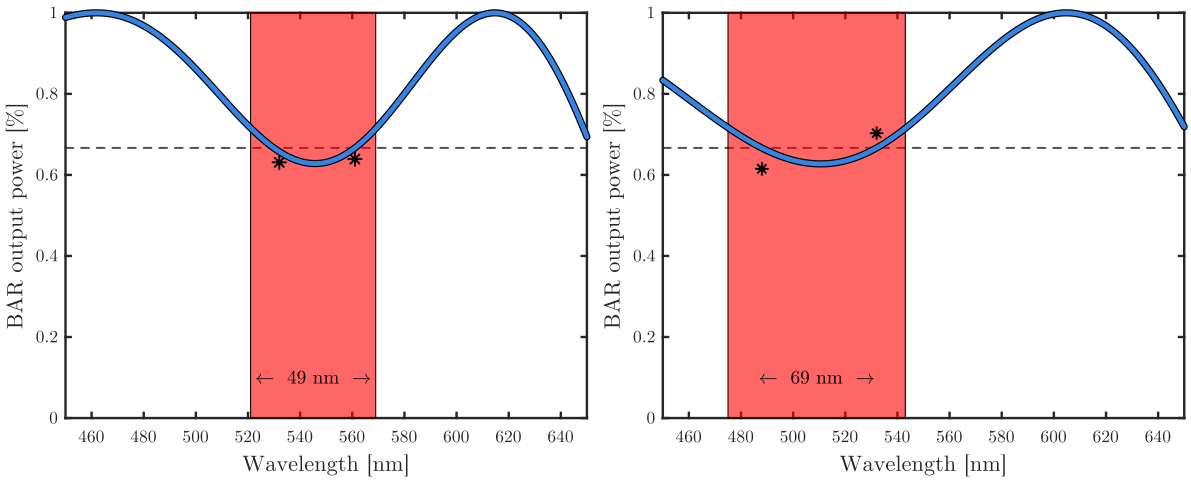

Figure 6.8: The panels represent two distinct broadband couplers realized. The blue lines describe the behaviour simulated at all the wavelengths. The regions shaded in red highlight the extension of the simulated bandwidths. The black markers report the measurements taken at wavelengths 532 and 561 nm (left), 488 and 532 nm (right).

figure.

These measurements constitute good evidence towards the possibility to realize broadband power splitters exploiting asynchronous couplers with the method described. Additional measurements, realized at multiple intermediate wavelengths are required to confirm the existence of a bandwidth around the desired splitting ratio and estimate its width.

Other geometries were tested to identify broadband couplers with splitting ratios equal to 33% and 50% but the results differed from the simulated ones. Figure 6.9 represents a coupler with a target splitting ratio equal to 33% centred between 488 and 561 nm. It can be seen that at 488 nm the device is working as expected, while at the two wavelengths 532 and 561 nm the experimental data points (black markers) deviate significantly from the expected behaviour (blue line). To identify the reason for this departure from the predicted response, it was chosen to simulate the response of the coupler subject to variability in its characteristics. The green line represents the response of the same coupler in the case of an increase in the values of the coupling coefficient of about +20% with respect to the predicted value. As one can see this simulation seems to describe the output measured at the three wavelengths. For this reason, it is hypothesised that a variation in the coupling coefficient interested the sample under investigation. This fluctuation in the value cannot be attributed to a stochastic variation in the fabrication since a secondary fabrication of the same device yielded comparable results. We can thus speculate the presence of the detuning to be the cause of this undesired variation from

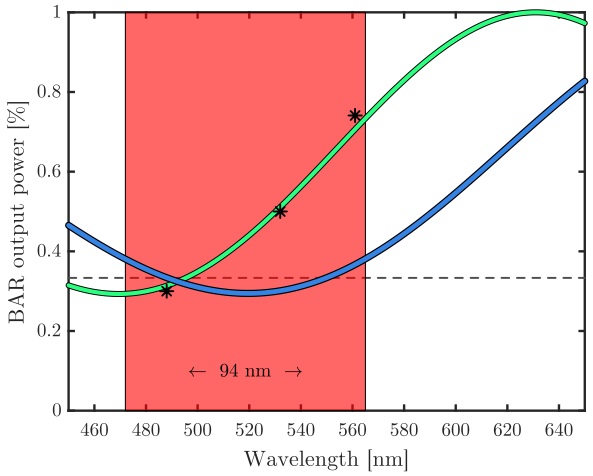

Figure 6.9: Simulation and experimental measurement of a broadband coupler. The blue line describes the behaviour simulated at all the wavelengths. The region shaded in red highlights the extension of the simulated bandwidth. The black markers report the measurements taken at wavelengths 488, 532 and 561 nm.

the expected outcome. In other words, the presence of the detuning could have impacted the coupling coefficient of the coupler causing a variation from what was estimated from the synchronous couplers studied in chapter 5.

Furthermore, the data gathered appear to highlight a possible pattern in the quality of the result and the dimension of the interaction distance. In fact, the devices whose behaviour was in line with the expected one were characterised by a higher value of the interaction distance (>4 μm). Conversely, the poorest results were found among the ones with a short interaction distance (3 μm $<$ d $<$ 4 μm). We hypothesize that interaction distances shorter than 4 μm may be too small to exclude that the waveguide traces come into contact, thus invalidating the assumption of weak coupling at the foundation of CMT. In fact, by lowering the inscription velocity of the waveguides the deposited energy increases, therefore it could be the case that the modification of the material may overlap significantly with the adjacent waveguide giving rise to a guiding structure not well described by CMT. Further investigation is necessary towards the understanding of the nature of this issue.

Therefore we argue that further analysis of the impact of the detuning on the response of directional couplers is required. In fact, at the current state it doesn't seem to be possible to identify the exact mechanism that produced this departure from the expect response. Nonetheless, the results obtained give us an insight on the possibility to realize the desired devices.

7 | Conclusions and future developments

In this thesis work, I have presented the work performed in the realization of the optical circuit required for the fluorescence excitation in an integrated structured illumination microscope. The goal of the project was to realize an integrated optical circuit capable of splitting the injected power of a laser beam equally in three waveguides. The device to be realized, referred to as *tritter*, was characterized by two power splitters cascaded one after the other so as to split the input power among two and then three waveguides. Precisely, it was chosen to realize the power splitters with integrated directional couplers. Furthermore, the splitters had to be designed so that their power-fractioning capabilities were independent of the injected wavelength thus allowing to perform illumination at distinct wavelengths with a single device.

The first experimental result concerned the identification of a good set of fabrication parameters for the realization of single-mode high-quality waveguides. Low-loss optical waveguides have been fabricated with FLM in alumino-borosilicate glass showing single-mode operation at several wavelengths (488, 532, 561 and 635 nm) in the visible range. After the identification of the set of parameters for the realization of the integrated optical circuit, I focused on the study of directional couplers fabricated with these parameters.

The agreement between the theory describing directional couplers and the experimentally fabricated ones was verified and a good working range of fabrication geometries was defined for the realization of these devices. The characteristic parameters controlling their behaviour, such as the coupling coefficient, were then extracted. The dependence of the coupling coefficient on the geometry of the coupler was investigated at several wavelengths. The complete characterization of the coupling coefficient allowed the simulation and fabrication of synchronous directional couplers with desired power splitting at its output.

The first approach investigated in the realization of multi-wavelength power splitters was to realize devices designed to meet the required splitting ratio at a selection of dis-

tinct wavelengths. A method was presented for the identification of coupler geometries yielding a target splitting ratio simultaneously at more than one wavelength, selected by design. In fact, exploiting information on the directional couplers measured at different wavelengths, an algorithm was developed with the purpose of autonomously identifying coupler geometries meeting the required characteristics with marginal error. This method was experimentally verified by the realization of two tritters. The first fabricated device was designed for the wavelengths 488 and 561 nm, while the second device was targeted at the three wavelengths 488, 561, and 635 nm. Both resulted in a satisfactory power splitting proving the correctness of this fabrication method. In fact, the resulting power splitting is expected to yield an optimal contrast (on average, 99.57% and 98.45 %) of the modulation pattern to be utilized for a structured illumination microscope. This method proved to be successful in the realization of splitters working at the same time at multiple wavelengths but also presents some issues as the limited number of operating wavelengths and their choice.

A second approach that was investigated dealt with the realization of couplers possessing a given splitting ratio in a bandwidth of wavelengths. To achieve this goal it was chosen to exploit asynchronous directional couplers. It was verified that asynchronous directional couplers can be realized in a controlled fashion by tuning one fabrication parameter. Furthermore, the wavelength dependence of the detuning was investigated. With the data available a numerical method was devised for the realization of broadband couplers with the desired splitting ratio in a designated bandwidth. Several devices have been fabricated exploiting this method to test its validity. The results obtained are not conclusive as it was not possible to realize all the desired splitting ratios, nonetheless, they provided good evidence towards the validation of the method presented. Further studies are necessary to verify the response of the realized devices over an extended range of wavelengths and to estimate its width. Moreover, the detuning realized requires additional investigation for the comprehension of its impact on the fabricated directional couplers.

In conclusion, the work presented reports on different solutions for the realization of multi-colour power splitters, each with its own merits and flaws. The first approach could be utilized when distinct wavelengths have to be selected, covering a particularly broad spectrum, conversely the second approach could be suitable for those applications in which tightly spaced wavelengths are selected in a narrower bandwidth. Future analysis foresees deepening the understanding of the behaviour of asynchronous couplers at the short visible wavelengths as required by fluorescence imaging.

Bibliography

[1] Robert G Hunsperger. *Integrated optics*, volume 4. Springer, 1995.

[2] Chin-Lin Chen. *Foundations for guided-wave optics*. John Wiley & Sons, 2006.

[3] Govind P Agrawal. *Fiber-optic communication systems*. John Wiley & Sons, 2012.

[4] Personal notes. Lecture notes from the course of micro-optics curated by prof. Marangoni Marco - Politecnico di Milano, 2021.

[5] Giancarlo C Righini and Andrea Chiappini. Glass optical waveguides: a review of fabrication techniques. *Optical Engineering*, 53(7):071819, 2014.

[6] Bahram Jalali and Sasan Fathpour. Silicon photonics. *Journal of lightwave technology*, 24(12):4600–4615, 2006.

[7] K. M. Davis, K. Miura, N. Sugimoto, and K. Hirao. Writing waveguides in glass with a femtosecond laser. *Opt. Lett.*, 21(21):1729–1731, Nov 1996.

[8] S Gross and MJ Withford. Ultrafast-laser-inscribed 3d integrated photonics: challenges and emerging applications. *Nanophotonics*, 4(3):332–352, 2015.

[9] Kwang-Sup Lee, Dong-Yol Yang, Sang Hu Park, and Ran Hee Kim. Recent developments in the use of two-photon polymerization in precise 2d and 3d microfabrications. *Polymers for advanced technologies*, 17(2):72–82, 2006.

[10] Roberto Osellame, Hugo Hoekstra, Giulio Cerullo, and Markus Pollnau. Femtosecond laser microstructuring: an enabling tool for optofluidic lab-on-chips. *Laser & photonics reviews*, 5(3):442–463, February 2011. 10.1002/lpor.201000031.

[11] Lawrence Shah, Alan Y Arai, Shane M Eaton, and Peter R Herman. Waveguide writing in fused silica with a femtosecond fiber laser at 522 nm and 1 mhz repetition rate. *Optics express*, 13(6):1999–2006, 2005.

[12] Roberto Osellame, Giulio Cerullo, and Roberta Ramponi. *Femtosecond laser micromachining: photonic and microfluidic devices in transparent materials*, volume 123. Springer, 2012.

[13] Thomas F. Johnston. Beam propagation (m2) measurement made as easy as it gets: the four-cuts method. *Appl. Opt.*, 37(21):4840–4850, Jul 1998.

[14] Alexander M Streltsov and Nicholas F Borrelli. Study of femtosecond-laser-written waveguides in glasses. *JOSA B*, 19(10):2496–2504, 2002.

[15] Shane M Eaton, Haibin Zhang, Mi Li Ng, Jianzhao Li, Wei-Jen Chen, Stephen Ho, and Peter R Herman. Transition from thermal diffusion to heat accumulation in high repetition rate femtosecond laser writing of buried optical waveguides. *Optics express*, 16(13):9443–9458, 2008.

[16] Linda Sansoni, Fabio Sciarrino, Giuseppe Vallone, Paolo Mataloni, Andrea Crespi, Roberta Ramponi, and Roberto Osellame. Polarization entangled state measurement on a chip. *Physical review letters*, 105(20):200503, 2010.

[17] Alexander Arriola, Simon Gross, Nemanja Jovanovic, Ned Charles, Peter G Tuthill, Santiago M Olaizola, Alexander Fuerbach, and Michael J Withford. Low bend loss waveguides enable compact, efficient 3d photonic chips. *Optics express*, 21(3):2978–2986, 2013.

[18] Yusuke Nasu, Masaki Kohtoku, and Yoshinori Hibino. Low-loss waveguides written with a femtosecond laser for flexible interconnection in a planar light-wave circuit. *Optics letters*, 30(7):723–725, 2005.

[19] Cyril Hnatovsky, RS Taylor, PP Rajeev, Eli Simova, VR Bhardwaj, DM Rayner, and PB Corkum. Pulse duration dependence of femtosecond-laser-fabricated nanogratings in fused silica. *Applied Physics Letters*, 87(1):014104, 2005.

[20] Audrey Champion and Yves Bellouard. Direct volume variation measurements in fused silica specimens exposed to femtosecond laser. *Opt. Mater. Express*, 2(6):789–798, Jun 2012.

[21] Calum A Ross, David G MacLachlan, Debaditya Choudhury, and Robert R Thomson. Optimisation of ultrafast laser assisted etching in fused silica. *Optics express*, 26(19):24343–24356, 2018.

[22] Roberto Memeo, Mattia Bertaso, Roberto Osellame, Francesca Bragheri, and Andrea Crespi. Laser-assisted etching of eaglexg glass by irradiation at low pulse-repetition rate. *Applied Sciences*, 12(3):948, 2022.

[23] Andrea Crespi, Roberto Osellame, and Francesca Bragheri. Femtosecond-laser-written optofluidics in alumino-borosilicate glass. *Optical Materials: X*, 4:100042, 2019.

[24] Krishna Chaitanya Vishnubhatla, Nicola Bellini, Roberta Ramponi, Giulio Cerullo, and Roberto Osellame. Shape control of microchannels fabricated in fused silica by femtosecond laser irradiation and chemical etching. *Optics express*, 17(10):8685–8695, 2009.

[25] Fulvio Flamini, Lorenzo Magrini, Adil S Rab, Nicolò Spagnolo, Vincenzo D'ambrosio, Paolo Mataloni, Fabio Sciarrino, Tommaso Zandrini, Andrea Crespi, Roberta Ramponi, et al. Thermally reconfigurable quantum photonic circuits at telecom wavelength by femtosecond laser micromachining. *Light: Science & Applications*, 4(11):e354–e354, 2015.

[26] Matteo Calvarese, Petra Paiè, Francesco Ceccarelli, Federico Sala, Andrea Bassi, Roberto Osellame, and Francesca Bragheri. Strategies for improved temporal response of glass-based optical switches. *Scientific Reports*, 12(1):1–9, 2022.

[27] Warren J Smith. *Modern optical engineering: the design of optical systems*. McGraw-Hill Education, 2008.

[28] Jerome Mertz. *Introduction to optical microscopy*. Cambridge University Press, 2019.

[29] Mats GL Gustafsson. Surpassing the lateral resolution limit by a factor of two using structured illumination microscopy. *Journal of microscopy*, 198(2):82–87, 2000.

[30] Mats GL Gustafsson. Nonlinear structured-illumination microscopy: wide-field fluorescence imaging with theoretically unlimited resolution. *Proceedings of the National Academy of Sciences*, 102(37):13081–13086, 2005.

[31] Hai Gong, Wenjun Guo, and Mark AA Neil. Gpu-accelerated real-time reconstruction in python of three-dimensional datasets from structured illumination microscopy with hexagonal patterns. *Philosophical Transactions of the Royal Society A*, 379(2199):20200162, 2021.

[32] Mark AA Neil, Rimas Juškaitis, and Tony Wilson. Method of obtaining optical sectioning by using structured light in a conventional microscope. *Optics letters*, 22(24):1905–1907, 1997.

[33] V Poher, HX Zhang, GT Kennedy, C Griffin, S Oddos, E Gu, DS Elson, JM Girkin, PMW French, MD Dawson, et al. Optical sectioning microscopes with no moving parts using a micro-stripe array light emitting diode. *Optics Express*, 15(18):11196–11206, 2007.

[34] Amit Lal, Chunyan Shan, and Peng Xi. Structured illumination microscopy image

reconstruction algorithm. *IEEE Journal of Selected Topics in Quantum Electronics*, 22(4):50–63, 2016.

[35] Matteo Calvarese. Thermal phase shifter design, optimisation and implementation for an on-chip structured illumination microscope. Master's thesis, Politecnico di Milano, 2020.

[36] Jan Huisken, Jim Swoger, Filippo Del Bene, Joachim Wittbrodt, and Ernst HK Stelzer. Optical sectioning deep inside live embryos by selective plane illumination microscopy. *Science*, 305(5686):1007–1009, 2004.

[37] Christoph J Engelbrecht and Ernst H Stelzer. Resolution enhancement in a light-sheet-based microscope (spim). *Optics letters*, 31(10):1477–1479, 2006.

[38] Bi-Chang Chen, Wesley R Legant, Kai Wang, Lin Shao, Daniel E Milkie, Michael W Davidson, Chris Janetopoulos, Xufeng S Wu, John A Hammer III, Zhe Liu, et al. Lattice light-sheet microscopy: imaging molecules to embryos at high spatiotemporal resolution. *Science*, 346(6208):1257998, 2014.

[39] Liang Gao, Wei-Chun Tang, Yun-Chi Tsai, and Bi-Chang Chen. Lattice light sheet microscopy using tiling lattice light sheets. *Optics Express*, 27(2):1497–1506, 2019.

[40] Yun-Chi Tsai, Wei-Chun Tang, Christine Siok Lan Low, Yen-Ting Liu, Jyun-Sian Wu, Po-Yi Lee, Lindsay Quinn Chen, Yi-Ling Lin, Pakorn Kanchanawong, Liang Gao, et al. Rapid high resolution 3d imaging of expanded biological specimens with lattice light sheet microscopy. *Methods*, 174:11–19, 2020.

[41] Bo-Jui Chang, Victor Didier Perez Meza, and Ernst HK Stelzer. csilsfm combines light-sheet fluorescence microscopy and coherent structured illumination for a lateral resolution below 100 nm. *Proceedings of the National Academy of Sciences*, 114(19):4869–4874, 2017.

[42] Petra Paiè, Rebeca Martínez Vázquez, Roberto Osellame, Francesca Bragheri, and Andrea Bassi. Microfluidic based optical microscopes on chip. *Cytometry Part A*, 93(10):987–996, 2018.

[43] Roberto Memeo, Petra Paiè, Federico Sala, Michele Castriotta, Chiara Guercio, Thomas Vaccari, Roberto Osellame, Andrea Bassi, and Francesca Bragheri. Automatic imaging of drosophila embryos with light sheet fluorescence microscopy on chip. *Journal of Biophotonics*, 14(3):e202000396, 2021.

[44] Petra Paiè, Francesca Bragheri, Andrea Bassi, and Roberto Osellame. Selective plane illumination microscopy on a chip. *Lab on a Chip*, 16(9):1556–1560, 2016.

[45] Federico Sala, Michele Castriotta, Petra Paiè, Andrea Farina, Sarah D'Annunzio, Alessio Zippo, Roberto Osellame, Francesca Bragheri, and Andrea Bassi. High-throughput 3d imaging of single cells with light-sheet fluorescence microscopy on chip. *Biomedical optics express*, 11(8):4397–4407, 2020.

[46] Matteo Calvarese, Petra Paiè, Alessia Candeo, Gianmaria Calisesi, Francesco Ceccarelli, Gianluca Valentini, Roberto Osellame, Hai Gong, Mark Neil, Francesca Bragheri, et al. Integrated optical device for structured illumination microscopy. *Optics Express*, 30(17):30246–30259, 2022.

[47] Prochip project. `https://pro-chip.eu/`.

[48] Alexander Killi, Andy Steinmann, Jochen Dörring, Uwe Morgner, Max J. Lederer, Daniel Kopf, and Carsten Fallnich. High-peak-power pulses from a cavity-dumped Yb:KY(WO4)2 oscillator. *Opt. Lett.*, 30(14):1891–1893, Jul 2005.

[49] Alexander Arriola, Simon Gross, Nemanja Jovanovic, Ned Charles, Peter G. Tuthill, Santiago M. Olaizola, Alexander Fuerbach, and Michael J. Withford. Low bend loss waveguides enable compact, efficient 3d photonic chips. *Opt. Express*, 21(3):2978–2986, Feb 2013.

[50] Corning Incorporated. EAGLE XG glass datasheet, 12.2021. `https://www.corning.com/media/worldwide/cdt/documents/EAGLE%20XG_PI%20Sheet_2021.pdf`.

[51] FP Kapron, Donald B Keck, and Robert D Maurer. Radiation losses in glass optical waveguides. *Applied Physics Letters*, 17(10):423–425, 1970.

[52] Matthias Will, Jonas Burghoff, Stefan Nolte, and Andreas Tuennermann. Femtosecond-laser-induced refractive index modifications for fabrication of three-dimensional integrated optical devices. In *Laser Micromachining for Optoelectronic Device Fabrication*, volume 4941, pages 58–64. SPIE, 2003.

[53] Giacomo Corrielli, Andrea Crespi, and Roberto Osellame. Femtosecond laser micromachining for integrated quantum photonics. *Nanophotonics*, 10(15):3789–3812, 2021.

[54] Alexander Szameit, Felix Dreisow, Thomas Pertsch, Stefan Nolte, and Andreas Tünnermann. Control of directional evanescent coupling in fs laser written waveguides. *Opt. Express*, 15(4):1579–1587, Feb 2007.

[55] Graeme Ball, Justin Demmerle, Rainer Kaufmann, Ilan Davis, Ian M Dobbie, and Lothar Schermelleh. Simcheck: a toolbox for successful super-resolution structured illumination microscopy. *Scientific reports*, 5(1):1–12, 2015.

[56] Peter G Kazansky and Martynas Beresna. Quill and nonreciprocal ultrafast laser writing. In *Femtosecond Laser Micromachining*, pages 127–151. Springer, 2012.

[57] Wei-Jen Chen, Shane M Eaton, Haibin Zhang, and Peter R Herman. Broadband directional couplers fabricated in bulk glass with high repetition rate femtosecond laser pulses. *Optics Express*, 16(15):11470–11480, 2008.

[58] David J Griffiths. *Introduction to Electrodynamics, Fourth Edition.* Pearson, 2021.

[59] Eric W Weisstein. Matrix exponential. *https://mathworld. wolfram. com/*, 2004.

A | Appendix: Three-beam interference pattern calculation

In this appendix is presented the calculation of the interference pattern resulting from the interference of three beams with different propagation directions. Furthermore, the maxima and minima points are localized and evaluated to estimate the visibility of the interference fringes. Starting from the definition of the energy density per unit volume for a monochromatic plane wave [58]:

$$\begin{aligned}
u &= \epsilon_0 \, |\vec{E}_{TOT}|^2 \\
&= \epsilon_0 \, \vec{E}_{TOT}\vec{E}^*_{TOT} \\
&= \epsilon_0 \, \left[\vec{E}_1 + \vec{E}_2 + \vec{E}_3\right] \cdot \left[\vec{E}^*_1 + \vec{E}^*_2 + \vec{E}^*_3\right] \\
&= \epsilon_0 \, \left[|\vec{E}_1|^2 + |\vec{E}_2|^2 + |\vec{E}_3|^2 + \vec{E}_1\vec{E}^*_2 + \vec{E}^*_1\vec{E}_2 + \vec{E}_1\vec{E}^*_3 + \vec{E}^*_1\vec{E}_3 + \vec{E}_2\vec{E}^*_3 + \vec{E}^*_2\vec{E}_3\right] \\
&= \epsilon_0 \, \left[|\vec{E}_1|^2 + |\vec{E}_2|^2 + |\vec{E}_3|^2 + 2\Re\left\{\vec{E}_1\vec{E}^*_2\right\} + 2\Re\left\{\vec{E}_1\vec{E}^*_3\right\} + 2\Re\left\{\vec{E}_2\vec{E}^*_3\right\}\right]
\end{aligned}$$

Now considering the expression for the electric field

$$\begin{aligned}
\vec{E}_j &= \frac{1}{2}\left[E_j e^{i\left(\omega t + \varphi_j - \vec{k}_j \cdot \vec{r}\right)} + c.c.\right]\hat{\varepsilon} \\
&= E_j \cos\left(\omega t + \varphi_j - \vec{k}_j \cdot \vec{r}\right)\hat{\varepsilon}
\end{aligned}$$

and substituting it in the previous equation we obtain:

$$
\begin{aligned}
u = \epsilon_0 \Bigg[& \sum_j E_j^2 \cos^2\left(\omega t + \varphi_j - \vec{k}_j \cdot \vec{r}\right) + \\
& + \sum_{j<k} 2\Re\left\{ \frac{1}{2}\left[E_j e^{i\left(\omega t + \varphi_j - \vec{k}_j \cdot \vec{r}\right)} + c.c.\right] \frac{1}{2}\left[E_k e^{i\left(\omega t + \varphi_k - \vec{k}_k \cdot \vec{r}\right)} + c.c.\right]^* \right\} \Bigg] \\
= \epsilon_0 \Bigg[& \sum_j E_j^2 \cos^2\left(\omega t + \varphi_j - \vec{k}_j \cdot \vec{r}\right) + \\
& + \frac{1}{2} \sum_{j<k} E_j E_k \Re\left\{ e^{i\left(\omega t + \varphi_j - \vec{k}_j \cdot \vec{r} + \omega t + \varphi_k - \vec{k}_k \cdot \vec{r}\right)} + e^{i\left(\cancel{\omega t} + \varphi_j - \vec{k}_j \cdot \vec{r} - \cancel{\omega t} - \varphi_k + \vec{k}_k \cdot \vec{r}\right)} + c.c. \right\} \Bigg] \\
= \epsilon_0 \Bigg[& \sum_j E_j^2 \cos^2\left(\omega t + \varphi_j - \vec{k}_j \cdot \vec{r}\right) + \\
& + \sum_{j<k} E_j E_k \left[\cos\left(2\omega t + \varphi_j + \varphi_k - \left(\vec{k}_k + \vec{k}_j\right) \cdot \vec{r}\right) + \cos\left(\varphi_j - \varphi_k + \left(\vec{k}_k - \vec{k}_j\right) \cdot \vec{r}\right) \right] \Bigg]
\end{aligned}
$$

Now to compute the intensity of the field we need to compute the temporal average over an optical cycle $T = \frac{2\pi}{\omega}$ of the energy density, in fact:

$$
I = \epsilon_0 c n \, \langle u \rangle = \epsilon_0 c n \, \frac{1}{T} \int_0^T u \, dt
$$

We notice that in the expression of u are present three terms:[1]

- The first term is proportional to $\cos^2(\omega t + \dots)$ and the temporal average of this factor is equal to $\frac{1}{2}$.
- The second term is proportional to $\cos(2\omega t + \dots)$ and its temporal average of this term is identically equal to zero.
- Finally, the last term is constant in time thus it is unaffected by the temporal averaging.

[1] Clearly the terms are actually 9 because of the presence of the sums over j and k.

Putting it all together we obtain the following expression for the intensity:

$$\begin{aligned} I(x,y) &= \epsilon_0 cn \left[\frac{1}{2}\sum_j E_j^2 + \sum_{j<k} E_j E_k \cos\left(\varphi_j - \varphi_k + \left(\vec{k}_k - \vec{k}_j\right)\cdot\vec{r}\right)\right] \\ &= \sum_j I_j + 2\sum_{j<k}\sqrt{I_j I_k}\cos\left(\Delta\varphi_{jk} + \left(\vec{k}_k - \vec{k}_j\right)\cdot\vec{r}\right) \end{aligned} \tag{A.1}$$

Where, in the last passage, we have defined the quantity $\Delta\varphi_{ij} \triangleq \varphi_i - \varphi_j$ describing the phase differences among the fields.

Now, expanding the sums and imposing the definition of the propagation vectors $\vec{k}_j = k\begin{bmatrix}\cos\theta_j \\ \sin\theta_j\end{bmatrix}$ in the xy plane we can identify the interference pattern as a function of space:

$$\begin{aligned} I(x,y) &= I_1 + I_2 + I_3 + \\ &\quad + 2\sqrt{I_1 I_2}\cos\left(\Delta\varphi_{12} + \left(\vec{k}_2 - \vec{k}_1\right)\cdot\vec{r}\right) + \\ &\quad + 2\sqrt{I_1 I_3}\cos\left(\Delta\varphi_{13} + \left(\vec{k}_3 - \vec{k}_1\right)\cdot\vec{r}\right) + \\ &\quad + 2\sqrt{I_2 I_3}\cos\left(\Delta\varphi_{23} + \left(\vec{k}_3 - \vec{k}_2\right)\cdot\vec{r}\right) \\ &= I_1 + I_2 + I_3 + \\ &\quad + 2\sqrt{I_1 I_2}\cos\left(\Delta\varphi_{12} + k\begin{bmatrix}\cos\theta_2 - \cos\theta_1 \\ \sin\theta_2 - \sin\theta_1\end{bmatrix}\begin{bmatrix}x & y\end{bmatrix}\right) + \\ &\quad + 2\sqrt{I_1 I_3}\cos\left(\Delta\varphi_{13} + k\begin{bmatrix}\cos\theta_3 - \cos\theta_1 \\ \sin\theta_3 - \sin\theta_1\end{bmatrix}\begin{bmatrix}x & y\end{bmatrix}\right) + \\ &\quad + 2\sqrt{I_2 I_3}\cos\left(\Delta\varphi_{23} + k\begin{bmatrix}\cos\theta_3 - \cos\theta_2 \\ \sin\theta_3 - \sin\theta_2\end{bmatrix}\begin{bmatrix}x & y\end{bmatrix}\right) \\ &= I_1 + I_2 + I_3 + \\ &\quad + 2\sqrt{I_1 I_2}\cos\left(\Delta\varphi_{12} + k\begin{bmatrix}-3/2 \\ -\sqrt{3}/2\end{bmatrix}\begin{bmatrix}x & y\end{bmatrix}\right) + \\ &\quad + 2\sqrt{I_1 I_3}\cos\left(\Delta\varphi_{13} + k\begin{bmatrix}0 \\ -\sqrt{3}\end{bmatrix}\begin{bmatrix}x & y\end{bmatrix}\right) + \\ &\quad + 2\sqrt{I_2 I_3}\cos\left(\Delta\varphi_{23} + k\begin{bmatrix}3/2 \\ -\sqrt{3}/2\end{bmatrix}\begin{bmatrix}x & y\end{bmatrix}\right) \end{aligned} \tag{A.2}$$

Where in the last passage we have imposed the condition that the three beams are propagating at the angles $\theta_1 = \frac{\pi}{3}$, $\theta_2 = \pi$ and $\theta_3 = \frac{5\pi}{3}$ in the xy plane as represented in figure A.1.

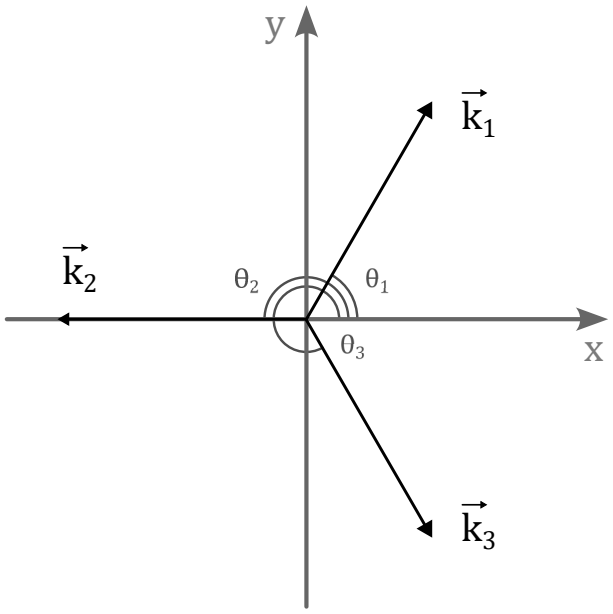

Figure A.1: Directions of propagation of the three beams.

The visibility of the interference fringes is defined as:

$$\mathcal{V} = \frac{I_{max} - I_{min}}{I_{max} + I_{min}}$$

Therefore to be able to calculate this value we need to know the intensity of the maxima and minima points of this interference pattern. Unfortunately, the calculation of these points cannot be performed analytically by imposing the gradient to be null hence it is here presented an alternative method.

Firstly we identify the locus of points where the three cosine function assume either maximum or minimum value by imposing their argument to be identical to $m_j\pi$ with $m_j \in \mathbb{Z}$. When m_j is an even number the respective cosine is at its maximum, while if it is odd, at its minimum.

$$\begin{cases} \Delta\varphi_{12} - \frac{3}{2}kx - \frac{\sqrt{3}}{2}ky = m_1\pi \\ \Delta\varphi_{13} - \sqrt{3}ky = m_2\pi \\ \Delta\varphi_{23} + \frac{3}{2}kx - \frac{\sqrt{3}}{2}ky = m_3\pi \end{cases}$$

Each of these equations identifies three different sets of parallel lines which describe the interference pattern resulting from the interference of two fields. For example, the second equation is a set of lines parallel to the x-axis resulting from the interference of the two plane waves propagating with directions $\vec{k}_1$ and $\vec{k}_3$.

By intersecting the set of lines corresponding to equations 1 and 2, and then 2 and 3, one identifies two sets of points which correspond to the points of space in which maxima and

minima of the respective cosine functions overlap. From equations 1 and 2 one obtains:

$$\begin{cases} \Delta\varphi_{12} - \frac{3}{2}kx - \frac{\sqrt{3}}{2}ky = m_1\pi \\ \Delta\varphi_{13} - \sqrt{3}ky = m_2\pi \end{cases} \Longrightarrow \begin{cases} x = \frac{1}{3k}\left(\Delta\varphi_{12} - \Delta\varphi_{23}\right) + \frac{1}{k}\left(m_2 - 2m_1\right)\frac{\pi}{3} \\ y = \frac{1}{\sqrt{3}k}\Delta\varphi_{13} - \frac{\sqrt{3}}{k}m_2\frac{\pi}{3} \end{cases} \tag{A.3}$$

Similarly from equations 2 and 3:

$$\begin{cases} \Delta\varphi_{13} - \sqrt{3}ky = m_2\pi \\ \Delta\varphi_{23} + \frac{3}{2}kx - \frac{\sqrt{3}}{2}ky = m_3\pi \end{cases} \Longrightarrow \begin{cases} x = \frac{1}{3k}\left(\Delta\varphi_{12} - \Delta\varphi_{23}\right) + \frac{1}{k}\left(2m_3 - m_2\right)\frac{\pi}{3} \\ y = \frac{1}{\sqrt{3}k}\Delta\varphi_{13} - \frac{\sqrt{3}}{k}m_2\frac{\pi}{3} \end{cases} \tag{A.4}$$

Now by imposing these two distinct sets of points to be identical we can identify the set of points where the maxima or minima of each of the three cosine functions overlap. As it is easy to see the y coordinate is identical in the sets while setting equal the x coordinate leads to the following expression linking the values m_1, m_2 and m_3.

$$m_3 = m_2 - m_1$$

This expression gives us some insight on the maxima and minima of the interference pattern, in fact:

- When m_2 and m_1 take both an even value, m_3 also takes an even value; this means that a set of points exists in which the maxima of the three cosine functions overlap. Thus we can state the maximum value assumed by the interference pattern is equal to $I_{max} = I_1 + I_2 + I_3 + 2\sqrt{I_1 I_2} + 2\sqrt{I_1 I_3} + 2\sqrt{I_2 I_3}$.
- Conversely when m_1 and m_2 are both odd m_3 is even, whereas when m_1 and m_2 are one odd and one even m_3 is odd; this means that a set of points exists where two of the cosine functions take minimum value and the other takes maximum value. Furthermore, it states that no point exists where all the minima of the three cosine functions overlap, as one might be tempted to assume.

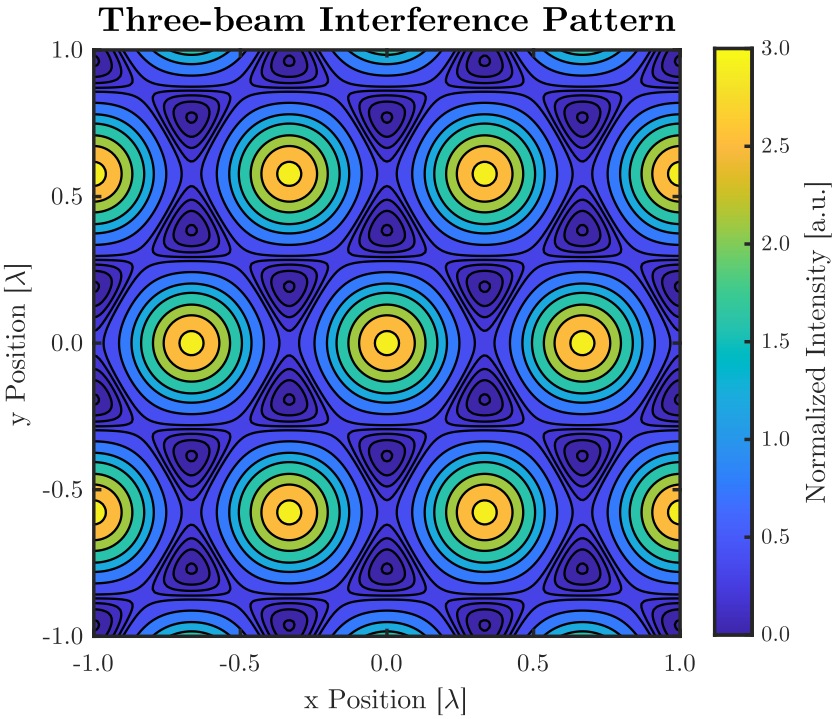

Figure A.2: Contour plot of the interference pattern of three beams.

As can be seen in figure A.2, adjacent maxima points are positioned at the vertexes of an equilateral triangle. Such points are found at the coordinates identified by either systems A.3 and A.4 reported above for values of m_1 and m_2 even, such that (m_1, m_2), $(m_1, m_2 + 2)$, $(m_1 - 2, m_2)$. In between two adjacent maxima are present saddle points, resulting from the overlap of two minima and a maximum of the three cosine functions. These points are found for values of m_j two odd and one even such that $(m_1, m_2 + 1))$, $(m_1 - 1, m_2 + 1)$, $(m_1 - 1, m_2)$. [2] These points take up a value of respectively:

$$
\begin{aligned}
I_{saddle} &= I_1 + I_2 + I_3 + 2\sqrt{I_1 I_2} - 2\sqrt{I_1 I_3} - 2\sqrt{I_2 I_3} \\
I_{saddle} &= I_1 + I_2 + I_3 - 2\sqrt{I_1 I_2} - 2\sqrt{I_1 I_3} + 2\sqrt{I_2 I_3} \\
I_{saddle} &= I_1 + I_2 + I_3 - 2\sqrt{I_1 I_2} + 2\sqrt{I_1 I_3} - 2\sqrt{I_2 I_3}
\end{aligned}
$$

The separation between adjacent maxima can be easily computed considering A.3:

$$
\begin{cases} \Delta x = \frac{1}{k}\left[m_2 - 2\left(m_1 - 2\right)\right]\frac{\pi}{3} - \frac{1}{k}\left[m_2 - 2m_1\right]\frac{\pi}{3} \\ \Delta y = 0 \end{cases} \Longrightarrow \begin{cases} \Delta x = \frac{2}{3}\lambda \\ \Delta y = 0 \end{cases}
$$

[2] Admittedly this set of points does not describe all the points on the plane. One also has to consider the set of points that form an equilateral triangle mirror image of the one described.

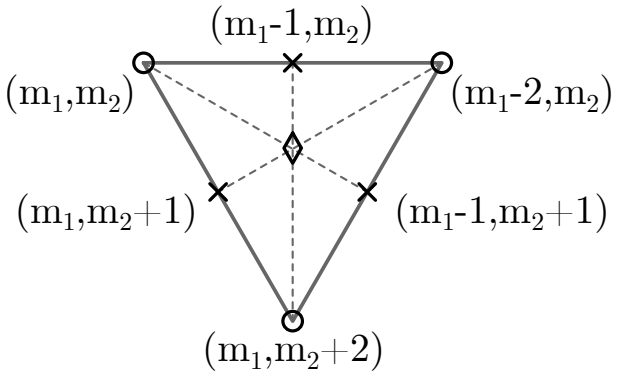

Figure A.3: Schematic representation of the notable points of the interference pattern. Highlighted with circles are the maxima, with crosses the saddle points and finally, with the diamond, the barycentre of the triangle, where the local minimum falls.

This means that this kind of interference pattern shows features that are smaller than the illumination wavelength in the medium λ, by a factor of $1/3$.

The local minima point falls in the barycentre of the equilateral triangle described by three adjacent maxima. Calling the vertexes A, B, C the coordinates of the barycentre are found at:

$$\begin{cases} x_G = \frac{1}{3}\left(x_A + x_B + x_C\right) \\ y_G = \frac{1}{3}\left(y_A + y_B + y_C\right) \end{cases}$$

$$\begin{cases} x_G = \frac{1}{3k}\left(\Delta\varphi_{12} - \Delta\varphi_{23}\right) + \frac{1}{3k}\left[m_2 - 2m_1 + m_2 - 2(m_1 - 2) + (m_2 + 2) - 2m_1\right]\frac{\pi}{3} \\ y_G = \frac{1}{\sqrt{3}k}\Delta\varphi_{13} - \frac{\sqrt{3}}{3k}\left(m_2 + m_2 + m_2 + 2\right)\frac{\pi}{3} \end{cases}$$

$$\begin{cases} x_G = \frac{1}{3k}\left(\Delta\varphi_{12} - \Delta\varphi_{23}\right) + \frac{1}{k}\left[m_2 - 2m_1 + 2\right]\frac{\pi}{3} \\ y_G = \frac{1}{\sqrt{3}k}\Delta\varphi_{13} - \frac{\sqrt{3}}{k}\left(m_2 + \frac{2}{3}\right)\frac{\pi}{3} \end{cases}$$

Finally, inserting these coordinates in equation A.2 we find the intensity in the minima points and obtain: [3]

$$I_{min} = I_1 + I_2 + I_3 - \sqrt{I_1 I_2} - \sqrt{I_1 I_3} - \sqrt{I_2 I_3}$$

In the ideal case where the three beams have equal intensity, $I_1 = I_2 = I_3 = \frac{1}{3}I_0$, the

[3] In these points the argument of the cosine functions takes on a value of either $\frac{2\pi}{3} + 2n\pi$ or $\frac{4\pi}{3} + 2n\pi$, therefore the cosine functions all take on a value of $-\frac{1}{2}$.

following is obtained:

$$I_{max} = 3I_0 \qquad I_{saddle} = \frac{1}{3}I_0 \qquad I_{min} = 0$$

Given the complexity of this particular interference pattern the computation of the visibility of the interference fringes is not straightforward, in fact, depending on the direction considered, different features are encountered, leading to a different value of the visibility $\mathcal{V}$. Moving in the directions $\frac{\pi}{6} + n\frac{\pi}{3}$ with $n = 0, 1, 2$ in between two maxima are found a minimum followed by a saddle point and yet another minimum. In these directions, the visibility takes a unitary value, considering maximum and minimum intensities I_{max} and I_{min}. Instead, going in the direction $n\frac{\pi}{3}$ with $n = 1, 2, 3$ — that is the direction that connects adjacent maxima points — a saddle point is located between two maxima. In this case, computing the value of the visibility yields $\mathcal{V} = 0.8$. The visibility is lower because the minima that are found in these directions are bigger than zero.

Considering instead the case in which the three beams have different intensities, the maxima and minima points will show an intensity that is respectively lower and higher than in the ideal case. For this reason, the visibility in the first direction mentioned will be lower the more unbalanced the intensity ratio is. Regarding the latter directions, the case is more complicated. In fact, the intensity of the saddle points encountered in the three different directions will be different according to the relative split of the intensities of the interfering beams. Specifically, I_{saddle} can be either higher or lower than the value in the ideal case, and consequently also the visibility will follow suit. It has been numerically tested that the average visibility for these three directions will take the maximum value of 0.8 — that is the ideal case value — only with perfectly balanced input beams, any deviation from these case will lead to an overall lower average visibility. To avoid the necessity to express the visibility in three directions on could think of calculating an average visibility considering the three directions, which coincidentally has the advantage of summarizing the information in a single figure of merit. Numerical simulations have shown that, because of the simultaneous increase of the visibility in one direction when the others decrease — due to an intensity unbalance — the average visibility hovers around near perfect values even at significant intensity unbalance, which could to a misleading interpretation of the pattern modulation.

Therefore, instead of the visibility, we employ the concept of modulation ratio or modulation depth, defined as the ratio of the oscillating component of the pattern over the

constant background.

$$M = \frac{AC}{DC}$$

Taking the Fourier transform of the intensity pattern, as expressed in equation A.1 for compactness we obtain what following:

$$\begin{aligned}\hat{I}(\vec{k}_\perp) &= \mathscr{F}\{I(x,y)\} \\ &= \sqrt{2\pi}\,\delta(\vec{k}_\perp)\sum_j I_j + \\ &\quad + \sqrt{2\pi}\sum_{j<k}\sqrt{I_j I_k}\Big[\delta\left(\vec{k}_\perp - \left(\vec{k}_k - \vec{k}_j\right)\right)e^{-i\Delta\varphi_{jk}} + \delta\left(\vec{k}_\perp + \left(\vec{k}_k - \vec{k}_j\right)\right)e^{+i\Delta\varphi_{jk}}\Big]\end{aligned}$$

In this expression we can identify the amplitudes of the DC component, thus the constant background, and the AC component, that is the modulation determined by the interference of the beams.

$$DC = \sqrt{2\pi}\,(I_1 + I_2 + I_3) \qquad AC = \sqrt{2\pi}\left(\sqrt{I_1 I_2} + \sqrt{I_1 I_3} + \sqrt{I_2 I_3}\right)$$

Plugging these values in the expression of the modulation ratio as defined above, we obtain a simple expression for the modulation ratio as a function of the intensities of the three beams. Therefore, we have a straightforward figure of merit to evaluate the goodness of the patterns that can be created with a non-equal intensity splitting among the beams.

$$M = \frac{\sqrt{I_1 I_2} + \sqrt{I_1 I_3} + \sqrt{I_2 I_3}}{I_1 + I_2 + I_3} \tag{A.5}$$

The modulation ratio takes unitary value in the case of equal intensity of the beams and decreases the more unbalanced they are.

B | Appendix: Code for the simulation of directional couplers

In this appendix it is presented the method that has been used to simulate the exchange of power of a directional coupler and to fit the experimental data in order to retrieve the characteristic parameters of the guiding structure. According to coupled mode theory, the power is exchanged between the two modes following the two coupled equations (1.12).

$$\begin{cases} \dot{A}_1(z) = -jk_{12}A_2(z)e^{j\Delta\beta z} \\ \dot{A}_2(z) = -jk_{21}A_1(z)e^{-j\Delta\beta z} \end{cases}$$

where $P_1(z) = |A_1(z)|^2$, $P_2(z) = |A_2(z)|^2$.

This system of equations can be rewritten in matrix notation as follows:

$$\begin{bmatrix} \dot{A}_1(z) \\ \dot{A}_2(z) \end{bmatrix} = \begin{bmatrix} 0 & -jk_{12}e^{+j\Delta\beta z} \\ -jk_{21}e^{-i\Delta\beta z} & 0 \end{bmatrix} \begin{bmatrix} A_1(z) \\ A_2(z) \end{bmatrix} = M \begin{bmatrix} A_1(z) \\ A_2(z) \end{bmatrix}$$

Going forward we will assume $k \triangleq k_{12} = k_{21}$.

To solve this system of coupled differential equations the following method can be exploited:

Given a linear system of the form $\dot{X}(z) = MX(z)$, its solution is determined by: $X(z_1) = e^{z_1 M}X(z_0)$ where $X(z_0)$ is the known initial value. [ref??]

In this specific case, the matrix M is not constant along z, since the two complex exponentials explicitly depend on z and k depends on z since the distance of the two waveguides is not constant along z. In particular, we will assume the coefficient k to have an exponential

dependence on the distance $d(z)$ like the following:

$$k(z) = a\, e^{-b \cdot d(z)}$$

Therefore, the system has to be solved with an iterative procedure, taking $z_1 = z_0 + dz$, where dz is small such that M can be considered constant.

In this case we can write:

$$\begin{bmatrix} A_1(z_n + dz) \\ A_2(z_n + dz) \end{bmatrix} = e^{dzM_n} \begin{bmatrix} A_1(z_n) \\ A_2(z_n) \end{bmatrix}$$

where $z_n = z_0 + n\, dz$

To compute the matrix e^{dzM} we exploit the method described in [59]:

Given a matrix B of the form:

$$B = \begin{bmatrix} a & b \\ c & d \end{bmatrix}$$

It can be shown that the matrix exponential of B is:

$$e^B = \frac{1}{\Delta} \begin{bmatrix} m_{11} & m_{12} \\ m_{21} & m_{22} \end{bmatrix}$$

where the matrix elements are:

$$\begin{aligned} m_{11} &= e^{(a+d)/2} \left[\Delta \cosh\left(\tfrac{1}{2}\Delta\right) + (a-d) \sinh\left(\tfrac{1}{2}\Delta\right)\right] \\ m_{12} &= 2be^{(a+d)/2} \sinh\left(\tfrac{1}{2}\Delta\right) \\ m_{21} &= 2ce^{(a+d)/2} \sinh\left(\tfrac{1}{2}\Delta\right) \\ m_{22} &= e^{(a+d)/2} \left[\Delta \cosh\left(\tfrac{1}{2}\Delta\right) + (d-a) \sinh\left(\tfrac{1}{2}\Delta\right)\right] \end{aligned}$$

and $\Delta \equiv \sqrt{(a-d)^2 + 4bc}$

In our specific case the elements $a, d = 0$ while $b = -jdzke^{+j\Delta\beta z}$ and $c = -jdzke^{-j\Delta\beta z}$ Thus:

$$\Delta \equiv \sqrt{4bc} = \sqrt{4\,(jdzk\,\cancel{e^{+j\Delta\beta z}})\,(jdzk\,\cancel{e^{-j\Delta\beta z}})} = 2jdzk$$

$$\begin{aligned} m_{11} &= m_{22} = \Delta \cosh\left(\tfrac{1}{2}\Delta\right) \\ m_{12} &= -2jdzk \sinh\left(\tfrac{1}{2}\Delta\right) e^{+j\Delta\beta z} \\ m_{21} &= -2jdzk \sinh\left(\tfrac{1}{2}\Delta\right) e^{-j\Delta\beta z} \end{aligned}$$

Therefore, in the end, we get:

$$e^{dzM} = \begin{bmatrix} \cosh(jdzk) & -\sinh(jdzk)\, e^{+j\Delta\beta z} \\ -\sinh(jdzk)\, e^{-j\Delta\beta z} & \cosh(jdzk) \end{bmatrix} = \begin{bmatrix} \cos(dzk) & -j\sin(dzk)\, e^{+j\Delta\beta z} \\ -j\sin(dzk)\, e^{-j\Delta\beta z} & \cos(dzk) \end{bmatrix}$$

Where in the last passage the following relations between hyperbolic and trigonometric functions have been exploited:

$$\cosh(jx) = \cos(x), \qquad \sinh(jx) = j\sin(x)$$

Finally, the solution of the system is determined by the sequence for z_n:

$$\begin{bmatrix} A_1(z_n + dz) \\ A_2(z_n + dz) \end{bmatrix} = \begin{bmatrix} \cos(dzk_n) & \sin(dzk_n)\, e^{-j\left(\frac{\pi}{2} - \Delta\beta z_n\right)} \\ \sin(dzk_n)\, e^{-j\left(\frac{\pi}{2} + \Delta\beta z_n\right)} & \cos(dzk_n) \end{bmatrix} \begin{bmatrix} A_1(z_n) \\ A_2(z_n) \end{bmatrix}$$

Here it is reported the MATLAB® code used to simulate a coupler following the methods just presented in this section.

```
function [BAR,phi0,phi,dd,z,k] = Coupler(d, D, R, L, a, b, db)

    D=D*1e-3;
    d=d*1e-3;

    dz = 0.010;

    % Defining the geometry of the coupler
    alpha = acos(1-(D-d)/(4*R));
    B = R*sin(alpha);

    N = round(L/dz);
    M = round(B/dz);

    T = N+M*4-3;

    theta = linspace(0,alpha,M);

    dd = [D-2*R*(1-cos(theta)), ...
          D-2*R*(1-cos(alpha))-2*R*(cos(fliplr(theta(1:end-1)))-cos(
   alpha)), ...
          d*ones(1,N), ...
```

```
22          D-2*R*(1-cos(alpha))-2*R*(cos(theta(2:end))-cos(alpha)), ...
23          D-2*R*(1-cos(fliplr(theta(1:end-1))))];
24
25      z = [linspace(0, 2*B, 2*M-1), ...
26      linspace(2*B, 2*B+L, N), ...
27      linspace(2*B+L, 4*B+L, 2*M-2)];
28
29      % Calculating coupling coefficient from the geometry
30      k = a.*exp(-b*dd);
31
32      phi = zeros(1,T);
33      A = zeros(2,T);
34
35      % Input power all in waveguide 1
36      A(:,1)=[1,0];
37
38      % Iterative procedure to integrate the system of differential eqs.
39      for i=2:T
40          t1 = k(i)*(z(i)-z(i-1));
41          t2 = cos(t1);
42          t3 = sin(t1);
43          t4 = exp(-1j*(pi/2-db*z(i)));
44          t5 = exp(-1j*(pi/2+db*z(i)));
45          C = [t2, t3*t4; t3*t5, t2];
46
47          A(:,i) = C*A(:,i-1);
48
49          phi(i)=phi(i-1)+t1;
50      end
51
52      phi0 = phi(2*M-1)+phi(end)-phi(T-2*M+2);
53      BAR = abs(A(1,:)).^2;
54  end
```

List of Figures

List of Tables

List of Symbols

Variable	Description	SI unit
k	Coupling coefficient	m^{-1}
L	Interaction length	m
d	Interaction distance	m
φ_0	Initial phase	rad
BAR	Output power at BAR waveguide	W
$\Delta\beta$	Detuning coefficient	m^{-1}
Δv	Writing velocity difference	m/s
M	Modulation ratio	-